

Utah State University

DigitalCommons@USU

All Graduate Theses and Dissertations

Graduate Studies

8-2021

Geologic Characterization of the Nonconformity Interface Using Outcrop and Drillcore Analogs: Implications for Injection-Induced Seismicity

Kayla Smith
Utah State University

Follow this and additional works at: <https://digitalcommons.usu.edu/etd>



Part of the [Geology Commons](#)

Recommended Citation

Smith, Kayla, "Geologic Characterization of the Nonconformity Interface Using Outcrop and Drillcore Analogs: Implications for Injection-Induced Seismicity" (2021). *All Graduate Theses and Dissertations*. 8186.

<https://digitalcommons.usu.edu/etd/8186>

This Thesis is brought to you for free and open access by the Graduate Studies at DigitalCommons@USU. It has been accepted for inclusion in All Graduate Theses and Dissertations by an authorized administrator of DigitalCommons@USU. For more information, please contact digitalcommons@usu.edu.



GEOLOGIC CHARACTERIZATION OF THE NONCONFORMITY INTERFACE
USING OUTCROP AND DRILLCORE ANALOGS: IMPLICATIONS FOR
INJECTION-INDUCED SEISMICITY

by

Kayla Smith

A thesis proposal submitted in partial fulfillment
of the requirements for the degree

of

MASTER OF SCIENCE

in

Geology

Approved:

Kelly K. Bradbury, Ph.D.
Major Professor

James P. Evans, Ph.D.
Committee Member

Dennis L. Newell, Ph.D.
Committee Member

D. Richard Cutler, Ph. D.
Interim Vice Provost
of Graduate Studies

UTAH STATE UNIVERSITY
Logan, Utah

2021

Copyright © Kayla Smith 2021
All Rights Reserved

ABSTRACT

Geologic Characterization of the Nonconformity Interface Using Outcrop and Drillcore
Analog: Implications for Injection-Induced Seismicity

by

Kayla Smith, Master of Science

Utah State University, 2021

Major Professor: Dr. Kelly K. Bradbury
Department: Geoscience

The pattern of recent increased seismicity in the midcontinent region of the United States is attributed to high volumes of injected wastewater reactivating subsurface faults at ~ 1 – 5 km depth near the Paleozoic sedimentary - Precambrian crystalline basement rock nonconformity contact. While much is known about the potential causes of induced seismicity, comparatively little is known about the geology and geochemistry of this interface region and how these factors may impact the permeability architecture and mechanical rock properties. In this study, we examine two drillcores intersecting the nonconformity and document the presence of a ~6-22 m altered/weathered horizon at the nonconformity between the Mount Simon Sandstone and Precambrian metagabbro. . This hydrogeologically distinct horizon is intensely faulted and fractured, semi-permeable (<1 - 443 mD). Petrographic and XRD analyses show the composition of this horizon is dominated by mechanically weak secondary mineralization, including carbonates and

phyllosilicates. This horizon also differs in its major oxide geochemistry and LOI compared to the relatively unaltered protolith. We provide a comparative set of detailed mineralogy, structures, geochemistry, porosity values, and lab permeability measurements that can be used to model impacts of fluid injection and migration proximal to the nonconformity interface.

We also examined the meso- to micro-scale spatial distribution of lithologic heterogeneities, structural features, mineralogy, and alteration (structural diagenesis) of the nonconformity interface in exhumed outcrops near Gunnison, Colorado. The drillcore and outcrop observations and analyses demonstrate the complex heterogenous rock properties and fluid migration pathways that may exist along and/or across nonconformity interface at depth, possibly contributing to fault reactivation and induced seismicity as a result of wastewater injection.

An additional aim of this work is to provide the constraints on the subsurface geologic setting for a proposed USU-USGS collaborative scientific drilling project. The proposed drilling project seeks to confirm the source of distinct, circular geophysical anomalies associated with the Northeast Iowa Intrusive Complex below the nonconformity interface contact as interpreted from aerial magnetic and gravitational surveys. We observed an intensely fractured and faulted metagabbro overlying a layered intrusive complex with a variable weathered and hydrothermally altered contact at the nonconformity.

PUBLIC ABSTRACT

Geologic Characterization of the Nonconformity Interface Using Outcrop and Drillcore
Analog: Implications for Injection-Induced Seismicity

Kayla Smith

Starting around 2009, a greater number of earthquakes than anticipated have occurred in the midcontinent region of the United States. These earthquakes have been linked to increased rates and volumes of wastewater injection at several km's depth into the Earth's crust near a contact between crystalline metamorphic or igneous rock and overlying sedimentary rock, known as a nonconformity. While much is known about why these new earthquakes occur, comparatively little is known about the physical and chemical rock properties because the nonconformity contact is primarily buried under km's of sedimentary rock in the midcontinent region. These rock properties are important because they influence rock strength and therefore the likelihood of earthquake activity. In this study, we examined two drillcores from southeastern Minnesota and document the presence of a ~6-22m horizon at the nonconformity which has been extensively altered due to low-temperature chemical weathering and high-temperature hydrothermal interaction. This distinct horizon is intensely damaged, semi-permeable, and is composed of mechanically weak minerals. We provide a comparative set of detailed mineralogy, structures, geochemistry, porosity values, and lab permeability measurements that can be used to model impacts of fluid injection and migration near the nonconformity interface.

We also examined rock properties of the nonconformity interface in surface exposures of the contact near Gunnison, Colorado. The drillcore and outcrop observations and analyses demonstrate complex variabilities in rock properties that may exist along and/or across nonconformity contacts at depth. These small- to large-scale rock variations can be used to understand how high-pressure injected fluids may move along or across the rock contact.

An additional goal of this work is to provide the background geologic information for a proposed USU-USGS collaborative scientific drilling project. This project targets previously identified magnetic and gravity anomalies associated with an underground igneous rock body called the Northeast Iowa Intrusive Complex. We observed an intensely fractured and faulted metagabbro overlying a layered intrusive complex with a weathered and hydrothermally altered contact at the nonconformity.

ACKNOWLEDGMENTS

I would like to thank my advisor, Kelly Bradbury, for her guidance, encouragement, and leadership. I would also like to thank my committee members Dennis Newell and Jim Evans for their insights and contributions.

I extend my gratitude to those who assisted with lab work and data collection/interpretation: Andrew Lonero, Will Kersey, Anna Paulding, Carli Studnicki, and the Washington State University Peter Hooper GeoAnalytical Lab. Additional thanks to Liz Petrie and Katie Potter for their field work contributions.

This research was primarily funded by the USGS-USU cooperative agreement #G17AC00345 awarded to Bradbury and Evans. Additional support came from the Geological Society of America student research grant, Stephen E. Laubach Structural Diagenesis Research Award, the Colorado Scientific Society Memorial Funds, and the Utah State University Department of Geoscience.

Kayla Smith

CONTENTS

	Page
Abstract.....	iii
Public Abstract.....	v
Acknowledgements.....	vii
List of Tables	xi
List of Figures	xii
Preface.....	xv
Chapter I	1
1. Project Objectives	1
2. Background	2
2.1 Problem: Induced Seismicity	2
2.2 Heterogeneities at the Injection Interface	7
2.3 Stress States and Fluid Migration	8
3. Geologic Setting	9
3.1 The Great Unconformity and Nonconformity Contacts.....	9
3.2 Oklahoma Geology	10
3.3 Minnesota Drillcores: A Structural Geochemical Analog	12
3.4 Gunnison, Colorado: A Structural Analog	15
4. Methodology and Workflow	18
4.1 Sample Acquisition and Core Logging.....	20
4.2 Field Work: Gunnison Analog Outcrops	20
4.3 Petrographic Analysis	21
4.4 Porosity and Permeability Measurements on BO-1 Drillcore	22
4.5 Whole Rock Mineralogy and Geochemistry	22
Chapter II: Manuscript: Geologic characterization across the sedimentary bedrock – crystalline basement nonconformity interface from two drillcores in SE Minnesota	24
Abstract	24
1. Introduction	25

2. Geologic Context	28
2.1 Induced Seismicity	28
2.2 Previous Work	29
2.3 B-1 and BO-1 Drillcore Analogs	30
3. Methods	34
3.1 Sample Acquisition and Detailed Core Characterization	34
3.2 Petrographic Analysis	36
3.3 Hydrogeologic Properties	36
3.4 Whole Rock Mineralogy and Geochemistry	38
4. Results	40
4.1 Above Nonconformity Interface	54
4.2 Nonconformity Interface: Upper Phyllosilicate Zone	58
4.3 Nonconformity Interface: Lower Phyllosilicate Zone	63
4.4 Nonconformity Interface: Transition Zone	69
4.5 Below the Nonconformity Interface: Amphibolite	74
4.6 Below the Nonconformity Interface: Layered Intrusions	78
4.7 B-1 Drillcore	83
5. Discussion	95
5.1 Geologic Features	95
5.2 Hydrogeologic Units	102
5.3 Injection Implications	107
6. Conclusion	111
Chapter III	113
1. Exhumed Outcrop Summary	113
1.1 Blue Mesa Dam	113
1.2 Hartman Rocks Recreation Area	116
Chapter IV	121
1. Conclusions	121
References	124

Appendices	134
Appendix A. Permeability values for select samples of the BO-1 drillcore	135
Appendix B. Porosity values for select samples of the BO-1 drillcore	136
Appendix C. XRF data for select samples of the BO-1 drillcore	141
Data Repository.....	https://usu.app.box.com/folder/64120489214

LIST OF TABLES

Chapter I.

	Page
Table 1. A summary of nonconformity characterizations	4

Chapter II.

Table 1. Qualitative XRD analysis for the BO-1 drillcore	51
Table 2. Qualitative XRD analysis for the B-1 drillcore	87
Table 3. Alteration intensity from meso- to micro-scale	101

LIST OF FIGURES

Chapter I.		Page
Figure 1. Initial lithology of the B-1 and BO-1 drillcores		14
Figure 2. Gunnison, CO field site geology		17
Figure 3. Visual methods summary		19
Chapter II.		
Figure 1. Location and geologic setting of B-1 and BO-1 drillcores in Fillmore County, MN		33
Figure 2. Geology of the BO-1 drillcore		41
Figure 3. Overview of meso-scale observations of the BO-1 Drillcore		42
Figure 4. Overview of micro-scale observations of the BO-1 Drillcore		43
Figure 5. Summary of hydrogeologic rock properties of BO-1 Drillcore		44
Figure 6. BO-1 drillcore major-element geochemistry from X-ray fluorescence		45
Figure 7. Relative major oxide concentrations of crystalline basement samples in the BO-1 drillcore		46
Figure 8. Bootstrapping statistical analysis of relative major oxide concentrations of crystalline basement samples in the BO-1 drillcore		47
Figure 9. Lithologic composition of Precambrian crystalline basement samples in the BO-1 Drillcore based on major-oxide geochemistry from X-ray fluorescence analysis ...		48
Figure 10. Summary of vein textures in the B-1 and BO-1 drillcores		49
Figure 11. Sedimentary samples from the BO-1 drillcore		55

Figure 12. Sedimentary photomicrographs from the BO-1 drillcore	57
Figure 13. Nonconformity upper phyllosilicate zone samples from the BO-1 drillcore	59
Figure 14. Nonconformity upper phyllosilicate zone photomicrographs from the BO-1 drillcore	61
Figure 15. Nonconformity lower phyllosilicate zone samples from the BO-1 drillcore	64
Figure 16. Nonconformity lower phyllosilicate zone photomicrographs from the BO-1 drillcore	66
Figure 17. Nonconformity transition zone samples from the BO-1 drillcore	70
Figure 18. Nonconformity transition zone photomicrographs from the BO-1 drillcore ..	72
Figure 19. Amphibolite samples from the BO-1 Drillcore	75
Figure 20. Amphibolite thin section scans from the BO-1 Drillcore	77
Figure 21. Layered intrusion samples from the BO-1 Drillcore	80
Figure 22. Layered intrusion thin section scans from the BO-1 Drillcore	82
Figure 23. Quartz arenite samples from the B-1 drillcore	85
Figure 24. Quartz arenite thin section scans from the B-1 drillcore	86
Figure 25. Clay-altered nonconformity boundary samples from the B-1 drillcore	89
Figure 26: Clay-altered nonconformity boundary thin section scans from the B-1 drillcore	90
Figure 27. Gabbro samples from the B-1 drillcore	93
Figure 28. Gabbro thin section scans from the B-1 drillcore	94
Figure 29. Visual categorization of alteration intensity at the meso to micro scale	100
Figure 30: Schematic of the midcontinent nonconformity interface based on observations from the B-1 and BO-1 drillcores	103

Chapter III.

Figure 1. Blue Mesa Dam outcrops 115

Figure 2. Hartman Rocks field site in Gunnison, CO 117

Figure 3. Hartman Rocks outcrop A 118

Figure 4. Hartman Rocks outcrop B 119

PREFACE

This thesis is divided into four chapters. The first chapter includes the background and literature review for the entirety of the project. The bulk of this work is centered around the geologic characterization of two drillcores from southern Minnesota. We also conducted fieldwork in Gunnison, Colorado in 2019. While this is not a focal topic of the thesis, the geologic background and sampling methods are also summarized in this chapter.

The second chapter is a stand-alone paper intended for submission to a scientific journal. This manuscript includes its own abstract separate from the broader thesis and focuses on the data pertaining to two drillcores collected from southeast Minnesota.

A summary of the field work data is discussed in Chapter III. The data collected during field work are not discussed in the manuscript, however it is relevant to the broader discussion of nonconformity characterization and development of subsurface models related to fluid migration along the nonconformity interface.

Chapter IV is a conclusion for the entire thesis. In this chapter, additional recommendations are made for future research relating to geologic characterization of regions vulnerable to induced seismicity or to inform subsurface models related to injection near the nonconformity contact. The raw data are electronically archived.

CHAPTER I

1. PROJECT OBJECTIVES

Induced seismicity is a current, societally relevant issue that this project seeks to address by understanding possible geologic contributors to subsurface permeability structure by characterizing the geology of analog injection sites. Induced seismicity is defined as *earthquakes where human activity, coupled with the state of stress within the crust, results in seismic slip on a pre-existing fault or fracture* (Foulger et al., 2018). The specific goals of this project are twofold: 1) to examine the spatial distribution of composition, structural features, and alteration along the sedimentary bedrock reservoir – crystalline basement rock nonconformity interface contact in select Minnesota drillcores and Gunnison, Colorado outcrop analog sites; and 2) to characterize subsurface rocks in southeast Minnesota that are suspected of producing large amplitude gravity and magnetic high anomalies within the Northeast Iowa Intrusive Complex (NEIIC) for a proposed USGS Scientific drilling project in northeastern Iowa (Drenth et al., 2015). This characterization helps constrain the bedrock geology of SE Minnesota, where rocks on the flank of the midcontinent rift are sampled.

We document the meso- to micro-scale variations in rock properties, structures, and permeability in two drillcores retrieved from exploration in southeastern Minnesota in 1962 and 1984 (MN Department of Natural Resources, 2020). At these scales, rock properties may directly impact hydromechanical properties, mineralogical reaction rates, and how injection fluids interact with the Precambrian basement, and thus influence the migration of fluids, fault reactivation, and the location of induced seismicity (Cuccio, 2017; Callahan

et al., 2019; Kolawole et al., 2019; Hesseltine, 2019; Petrie et al., 2020). This work focuses on compositional and textural variations at the targeted analog sites and continues to build on an extensive rock property database of the nonconformity interface contact region as summarized by Petrie *et al.* (2020) (Table 1). This work also provides permeability and porosity data which is key to understanding the hydromechanical rock properties of the nonconformity interface (Cuccio, 2017; Petrie et al., 2020). Results herein provide critical geologic constraints for determining rock properties of the nonconformity boundary and thus contribute to refined input parameters for hydromechanical and seismic risk models.

2. BACKGROUND

2.1 Problem: Induced Seismicity

Over the past decade, the midcontinent region of the United States has experienced a sharp increase in the frequency and magnitude of earthquakes with $M_w > 3.0$, particularly in Kansas, Texas, Colorado, and Oklahoma (Ellsworth, 2013; Rubinstein and Mahani, 2015; USGS, 2018). This seismicity has been attributed to the injection of wastewater fluids associated with production of oil and gas from midcontinent reserves (Keranen et al., 2014; Walsh and Zoback, 2015). Large volumes of fluids are injected at high rates with an estimated 2 billion gallons of wastewater injected daily into U.S. Class II wells which target porous sedimentary bedrock reservoir rocks that nonconformably overlie Precambrian crystalline basement rocks (Murray, 2015; EPA, 2017).

Earthquakes at the Rocky Mountain Arsenal (RMA) northeast of Denver, Colorado were among the first to be acknowledged as anthropogenic earthquakes. At this site, wastewater injection produced over 700 earthquakes including several $M_L > 5$ (Evans, 1966; Healy et

al., 1968; Foulger et al., 2018). In addition to fluid injection, earthquakes have been induced by other activities such as large-scale construction, mining activities, and geothermal operations (Foulger et al., 2018). Induced seismic events as large as M_w 5.8 have occurred (Pawnee, OK in 2016) and have caused millions of dollars in damage within the midcontinent region (Jones, 2016; USGS, 2019).

Table 1: A summary of nonconformity characterizations. Samples related to this project are shaded in yellow.

Study Site/Location	Core/ Outcrop	Formations	Lithologies of Interface	Structure	Researcher
Gallinas Canyon (New Mexico) 35° 39' 37.4" N, 105° 20' 13.6" W	Outcrop	Del Padre Member of the Espiritu Santo Fm. overlying Precambrian Gneiss and Schist	Silica and calcite cemented massive fine- to very coarse-grained sandstone overlying crystalline basement which varies from gneiss, granite, basalt, and green schist.	Faults were observed in the sedimentary units truncating against the contact and bisecting the contact. The outcrop was severely deformed. Mineralized and non-mineralized fractures were observed in the sedimentary units.	Kellie Kerner (M.S. Student), Garth Hesselstine (M.S. Student)
Phantom Canyon (Colorado) 38° 30' 43.3" N, 105° 06' 40.7" W	Outcrop	Pennsylvanian Fountain Fm overlying Precambrian Granite	Silica rich dolomitized marine carbonates with shallow karst erosion with intergranular microporosity and iron oxide minerals between dolomite grains overlying weathered granite with granitic dikes.	Two normal faults were observed bisecting the contact with associated damage zones surrounding them. In both cases, the basement fault core was wider than the sedimentary fault core.	Kellie Kerner (M.S. Student)
CPC BD-139 (Michigan) 359437 E, 4732092 N UTM Grid 17T	Core	Cambrian Mt Simon Sandstone overlying Precambrian Gneiss	Cemented fine-grained laminated quartz arenite overlying a finely foliated, weathered gneiss	Fragmented carbonate veins were observed in the weathered portion of the basement rock.	Laura Cuccio (M.S. Student)
CPC BD-151 (Michigan) 359024 E, 4738656 N UTM Grid 17T	Core	Cambrian Mt Simon Sandstone overlying Precambrian Gneiss	Carbonate cemented fine-grained sandstone with fine-scale laminae and evidence of bioturbation/soft sediment deformation overlying a weathered gneiss	No faults were observed in the sedimentary strata. A sub-vertical alteration zone was observed in the basement rock approximately 3m below the contact	Laura Cuccio (M.S. Student)
UPH-1 (Illinois) 264394 E, 4709549 N UTM Grid 16T	Core	Cambrian Mt Simon Sandstone overlying Precambrian Granite	Tan and purple cross bedded, medium- grained, well stored sandstone grading into interbedded red and green siltstone grading into interbedded grus and siltstone overlying pink, coarse-grained granite with few fractures and minor alteration	No faults were observed in either the sedimentary strata or the basement rock, however altered microfractures were observed in quartz and feldspar grains in the upper 5m of the granite.	Laura Cuccio (M.S. Student)
Merrimack, Wisconsin	Outcrop	Cambrian Parfrey's Glen Fm overlying Precambrian Baraboo Quartzite	Pebble- to boulder-sized quartzite clast conglomerate overlying quartzite	No faults were observed at this site.	Laura Cuccio (M.S. Student)
Presque Isle, Marquette, Michigan	Outcrop	Proterozoic Jacobsville Sandstone overlying Archean Serpentinized Peridotites	Fine-medium grained subarkosic sandstone with iron oxide and clay alteration interbedded with cohesive conglomerates and friable, incohesive basal conglomerates with clasts consisting of jasperoid, quartz, feldspar, and sandstone overlying serpentinized peridotite	Three of four observed faults truncate at the interface and are associated with iron oxide mineralization, while the fourth bisects the contact and appears as a silica rich vein in the basement rock	Laura Cuccio (M.S. Student)

Table 1: A summary of nonconformity characterizations (continued).

Hidden Beach/Little Presque Isle, Marquette, Michigan	Outcrop	Proterozoic Jacobsville Sandstone overlying Archean Compeau Creek Gneiss	Fine-medium grained subarkosic sandstone with a basal conglomerate of sub-angular to rounded jasperoid, gneiss, and greenstone clasts overlying gneiss with inclusions of schist and thin veins of quartz and epidote	Bleached fracture zones are present in the Jacobsville Sandstone. Small displacement faults only observed in basement rock with truncation at conglomerate layer	Laura Cuccio (M.S. Student)
Cody, Wyoming	Outcrop	Cambrian Flathead Sandstone overlying Precambrian Granite	Cambrian Flathead Sandstone overlying granite with a weathered horizon and presence of grus in some parts of the exposure	Faults were observed in both the sandstone and the granite as well as bisecting the contact between these two units. Both sandstone and basement hosted faults were observed truncating at the contact while vertical fractures were observed bisecting the contact.	Laura Cuccio (M.S. Student)
Gogebic Core (Michigan): D9-08-20, D9-08-22, D9-08-23, D9-08-24	Core	Jacobsville Sandstone and Bessemer Sandstone overlying Michigamme Slate	The Jacobsville and Bessemer sandstones are red, medium- to coarse-grained, and well sorted with interbeds of mudstone and shale. The sandstones are jointed, bleached, and silicified. The Michigamme slate is oxidized, non-graphitic slate, graphitic slate, and interbedded graywacke.	The graphitic slate has faults surfaces with purple smear. The slates are cut by intermittent faults, clay gouges, bleached zones, leached zones with abundant voids, pressure solution seams, folded and contorted layers, clay-rich shear zones, and broken core intervals.	Garth Hesselstine (M.S. Student)
Baker's Bridge, Colorado	Outcrop	Precambrian Conglomerates, Devonian Tamaron Member of the Ignacio Fm, and McCracken Member of the Elbert Fm overlying Precambrian Baker's Bridge Granite	Precambrian conglomerates, quartz cemented, variably colored, planar laminated, cross bedded sandstone interbedded with thin (<15 cm) shale beds (Tamaron Sandstone) and sandy dolomite (McCracken Dolomite) overlying a relatively homogenous granite composed of microcline, perthite, quartz, plagioclase, and hornblende with accessory zircon, apatite, magnetite, calcite, and epidote	Joints and fractures can be found cutting both the sedimentary strata and the basement rock with clay infilling. The basement rock is relatively fresh and unweathered.	Garth Hesselstine (M.S. Student)
RC Taylor Whole Rock Drill Core (Nebraska)	Core	Cambrian Lamotte Sandstone overlying sheared and weathered Proterozoic granitic basement	Arkosic, fine-grained, well sorted sandstone containing abundant glauconite and veinlets of quartz, calcite, and Fe-oxide overlying weathered and sheared granitic basement	Fractures and veins are observed in both the sedimentary strata and the basement rock	Liz Petrie, Tello (Undergraduate)

Table 1: A summary of nonconformity characterizations (continued).

Hartman Rocks Recreation Site, Gunnison CO	Outcrop	Brushy Basin member of the Morrison formation and amphibolite basement. Reverse fault contact (Gunnison fault)	Seds not present in outcrop due to extensive fault gouge and fracture zone. Amphibole host rock is medium grain with 30-40% plagioclase in some areas.	Extensively fractured fault zone with pods of cohesive quartz material in clay-rich fault gouge. Intense Fe-oxide alteration	Kayla Smith (M.S. Student)
Blue Mesa Dam, Gunnison CO	Outcrop	Depositional contact between Jurassic sandstone (Wanakah or Morrison Formation?) and Precambrian pegmatitic amphibolite gneiss	Carbonate cemented sandstone with granule clasts & muddy layers. Non-foliated amphibolite. No banding, but pegmatite veins 5-30cm thick.	Basement rock is jointed and relatively unweathered other than a discontinuous shear zone at the nonconformity contact. Iron oxide weathering along the joints and fractures	Kayla Smith (M.S. Student)
B-1 (Minnesota)	Core	Cambrian Mt. Simon Sandstone overlying Precambrian basement	Metagabbro with alteration of feldspars to clay. Grades to less alteration below contact. Some areas of serpentinization	Many veins and possible gouge zones in basement. Contact is very unconsolidated, clay rich, and propylitic.	Kayla Smith (M.S. Student)
BO-1 (Minnesota)	Core	Cambrian Mt. Simon Sandstone overlying Precambrian basement	Metagabbro with alteration of feldspars to clay. Grades to less alteration below contact. Core also intersects diabase and felsic pegmatites	Veined and faulted within the basement.	Kayla Smith (M.S. Student)

2.2 Heterogeneities at the Injection Interface

Buried lithologic and structural heterogeneities caused by composition and structural fabrics, fault and fracture system intensities and geometries, weathering, and fluid alteration can lead to unexpected fluid pressure migration patterns across the nonconformity and possibly reactivate basement and/or reservoir faults (Cuccio, 2017; Callahan et al., 2019; Kolawole et al., 2019). For example, phyllosilicate-rich alteration parallel to the sedimentary reservoir – crystalline basement interface may create a barrier to downward fluid flow and promote lateral migration to distal faults potentially intersecting the nonconformity (Zhang et al., 2013; Ortiz et al., 2018). Chemical interactions between *in-situ* fluids and minerals can lead to diagenetic alteration that impacts mechanical rock properties and failure criterion (Laubach et al., 2010).

The lateral discontinuity of the weathered and/or altered zone complicates the hydromechanical properties of the nonconformity interface contact (Cuccio, 2017; Ortiz et al., 2018; Petrie et al., 2020). The predicted contact geometries are also complicated due to faulting and past differential erosion of the Precambrian basement, which may exhibit significant paleo-topography along the nonconformity contact and localized permeability changes (Franseen et al., 2004; Petrie et al., 2020). Fluid migration within fault zones is highly variable and will depend on fault structure, composition, and mechanics (Caine et al., 1996; Faulkner et al., 2010). Highly altered and weathered areas are more likely to deform during faulting via granular flow rather than brittle fracturing and often result in a permeability reduction (Kerner, 2015).

2.3 Stress States and Fluid Migration

An earthquake is initiated by an increase in shear stress, or a decrease in frictional resistance, normal stress, or cohesion along a fault. Fault failure is mathematically expressed as:

$$\tau = \tau_0 + \mu(\sigma_n - p)$$

where τ is shear stress, τ_0 is cohesion, μ is the coefficient of friction, σ_n is the normal stress, and p is the pore pressure (Nicholson and Wesson, 1990; McGarr et al., 2002). Likelihood of failure depends on the existing states of stress in the crust and the orientation of the fault in relation to increases in pore pressure from fluid injection (Nicholson and Wesson, 1990). For example, hydraulically conductive fault systems near injection sites are more likely to transmit fluids and extend the possible failure region compared to injection sites with a basal seal between the injection site and faulted region (Zhang et al, 2013). Transmission of injection fluids and associated pressures increases the likelihood of encountering a critically stressed fault and creating a seismic event (Goebel and Brodsky, 2018). In the case of midcontinent seismicity at depths that occur near the buried nonconformity region, earthquakes can be induced by the increase pore fluid pressure from wastewater injection or a loss of frictional resistance when fluids reach hydraulically conductive fault zones (Doglioni, 2017). High rates of injection (>300,000 barrels of wastewater/month) are therefore more likely to produce seismicity because of the increased pore pressures (Weingarten et al., 2015) especially when injected proximal to the basement interface (Hinks et al., 2018).

The hydraulic behavior of faults and their damage zones facilitates the migration of fluids and pore pressures to greater depths and further distances depending on their

structure (Yehya et al., 2018). Critically stressed faults are those that are favorably oriented to fail, and are typically hydraulically conductive in order to maintain hydrostatic pressures (Townend and Zoback, 2000). Furthermore, studies have shown that altered basement rocks can create more pore space and increase permeability under high stress (Evans et al., 2005). Deeper injection provides direct access to hydraulic pathways that may be near or migrate to critically stressed faults (Zhang et al., 2013). However, there is disagreement on whether injection rates or proximity to basement faults have greater control over inducing a seismic event (Weingarten et al., 2015; Hinks et al., 2018).

High injection rates, coupled with the fact that pore fluid pressures do not exceed hydrostatic even at great depths (Townend and Zoback, 2000) imply that pressure builds where the speed and volume of injection exceeds the rate at which fluids can migrate through pore spaces and fractures. This buildup of pressure must be displaced to the surrounding rock, which can cause failure in areas without a localized increase in pore pressure, as seen by earthquakes which occur up to 90 kilometers away from injection sites (Peterie et al., 2018).

3. GEOLOGIC SETTING

3.1 The Great Unconformity and Nonconformity Contacts

The Great Unconformity, first identified by Powell *et al.* (1875) in the Grand Canyon, is defined as the nonconformity of Proterozoic metamorphic or igneous rock overlain by lower Paleozoic rock which extends across much of the United States. This rock sequence formed from Cambrian sea level rise that deposited sediment over the Laurentian continental craton (Haq and Schutter, 2008). It represents a gap in geologic time

spanning up to 1.2 Ga (Karlstrom and Timmons, 2012). What caused this erosional period and what happened during that missing time is debated; hypotheses include massive glacial erosion during Neoproterozoic periods of global glaciation and increased ocean alkalinity leading to more extensive weathering (Peters and Gaines, 2012; Keller et al., 2019). Other efforts to interpret the Great Unconformity reveal a minimum of 6 km of exhumation corresponding with the Rodinia and Pangea supercontinent breakups (DeLucia et al., 2017).

Interest in the Great Unconformity contact has recently increased because of: 1) its relation to midcontinent induced seismicity as it falls within close proximity to wastewater injection horizons; and 2) it represents a vast gap in geologic time and knowledge where new dating technologies are able to shed more light on its exhumation history (DeLucia et al., 2017; Keller et al., 2019). Characterizing the nonconformity contact in the midcontinent area is challenging because it is poorly exposed, and at depth relatively few drillcores penetrated the basement, thus relatively little is known about the structure, alteration, and permeability architecture. Exhumed outcrops of nonconformity contacts are plentiful in the southwestern U.S. and provide an opportunity to study analogs to the Great Unconformity/nonconformity interface contact within the midcontinent region. Surface exposures also allow for mapping the spatial relationships between topography, structure, and alteration across the nonconformity interface contact at broader scales.

3.2 Oklahoma Geology

Most seismic events in the midcontinent area with $M \geq 4.0$ occur in the north central region of Oklahoma (Rubinstein and Mahani, 2015; USGS, 2018). These earthquakes

nucleate at depths of 0.1-13 km (USGS, 2019). Multiple complex fault systems span across the state from the surface to the basement rocks (Marsh and Holland, 2016).

The Cambrian-Ordovician Arbuckle Group is the primary zone targeted for Class II wastewater injection wells in Oklahoma and Kansas (Murray, 2015). The Arbuckle Group is composed of carbonates with laterally continuous sandstone units. Reservoirs in the Arbuckle Group are complex and heterogenous owing to the presence of paleokarst, diagenesis of the rocks, stratigraphic variation, and presence of fractures from tectonic stresses over time (Fritz et al., 2012). This unit is also known for seismicity in association with CO₂ injection wells (Smith and Jaques, 2016). The lowest member of the Arbuckle Group is the Fort Sill Limestone overlain by Royer Dolomite. These units overlay the Great Unconformity and basement rock, which is composed of Cambrian Reagan Formation over Precambrian granites (Murray, 2015).

The nature of fluid migration at the nonconformity interface contact is complicated by which sedimentary unit borders the basement. Carbonate rocks have extremely complex hydrology because secondary dissolution and fractures introduce high permeability pathways in an otherwise low permeability material. Measurements of the Arbuckle Group show a range of 2-19.8% porosity (Manger, 1963). The more silicic units have 6% to 18% porosity with permeability ranging from 0.1 md to 50 md. (Franseen et al., 2004).

Between 2009-2014, an average of 645.2 million barrels of wastewater per year was disposed in the Arbuckle and Precambrian rocks (58.6% of total yearly disposal) with some individual wells supporting an excess of one million barrels of fluid per year (Murray, 2015). Many buried faults exist within the Precambrian rock of the midcontinent region, occasionally crossing into the younger strata as well (Murray, 2015 and references therein;

Petrie et al, 2020). Where the inter-plate stressed faults promote the creation of conductive faults and fractures (Townend and Zoback, 2000), these structures can be a path for fluid migration. The largest earthquake associated with these geologic units was a M_w 5.8 in Pawnee, OK, which has several disposal wells nearby which inject greater than one billion barrels of wastewater per year between 2009-2014 (Murray, 2015).

3.3 Minnesota Drillcores: A Structural and Geochemical Analog

Two borehole drillcores (B-1 and BO-1) were extracted in the southeast corner of Minnesota in Fillmore County as a part of an exploratory mining project in 1962 (Figure 1; Gilbert, 1962). This area was targeted because of geophysical anomalies which were initially detected by The New Jersey Zinc Company during airborne reconnaissance surveys. Gravity data indicated a body of dense rock which roughly corresponded with readings indicating the presence of magnetic rock materials. Their analysis of the core revealed that the source of the anomalies was a Precambrian metagabbro with intergrowths of iron and titanium (Gilbert, 1962).

The nature of the rocks revealed in drillcores are of broad scientific interest because they: 1) intersect strata analogous to injection horizons and subsurface strata where induced seismicity occurs; 2) they provide the opportunity to study fluid-rock interaction along a vertical cross section across the Precambrian nonconformity with no modern weathering as seen in uplifted outcrops, and 3) they are the closest boreholes to geophysical anomalies associated with the Northeast Iowa Intrusive Complex (NEIIC) which were detected during recent USGS mapping efforts (Anderson, 2012; Drenth et al., 2015). The NEIIC is hypothesized to be a part of the Midcontinent Rift System (MRS), which form the

Precambrian crystalline basement rocks and intrude into Yavapai rocks. This 1.1 Ga. failed rift system extends for ~1600 km and is difficult to characterize because it remains largely at depth, or is poorly exposed in parts of northern Wisconsin and eastern Minnesota. Previous studies have identified it as a fault bounded basin filled with volcanics and covered with ~ 2 km of sedimentary rock, which thins towards the north (Hinze et al., 1990).

Boreholes BO-1 and B-1 in southeastern Minnesota offer the closest available drillcores that intersect the crystalline basement rocks hypothesized to be the source of the mapped geophysical anomalies (Drenth et al., 2015). The boreholes also serve to constrain the bedrock geology proximal to the midcontinent rift, which is a region targeted for a proposed scientific drilling project in Northeast Iowa (Anderson, 2012; Drenth et al., 2015; Drenth et al., 2020). For additional information on the geologic setting of these drillcores, refer to Chapter 2 section 2.3.

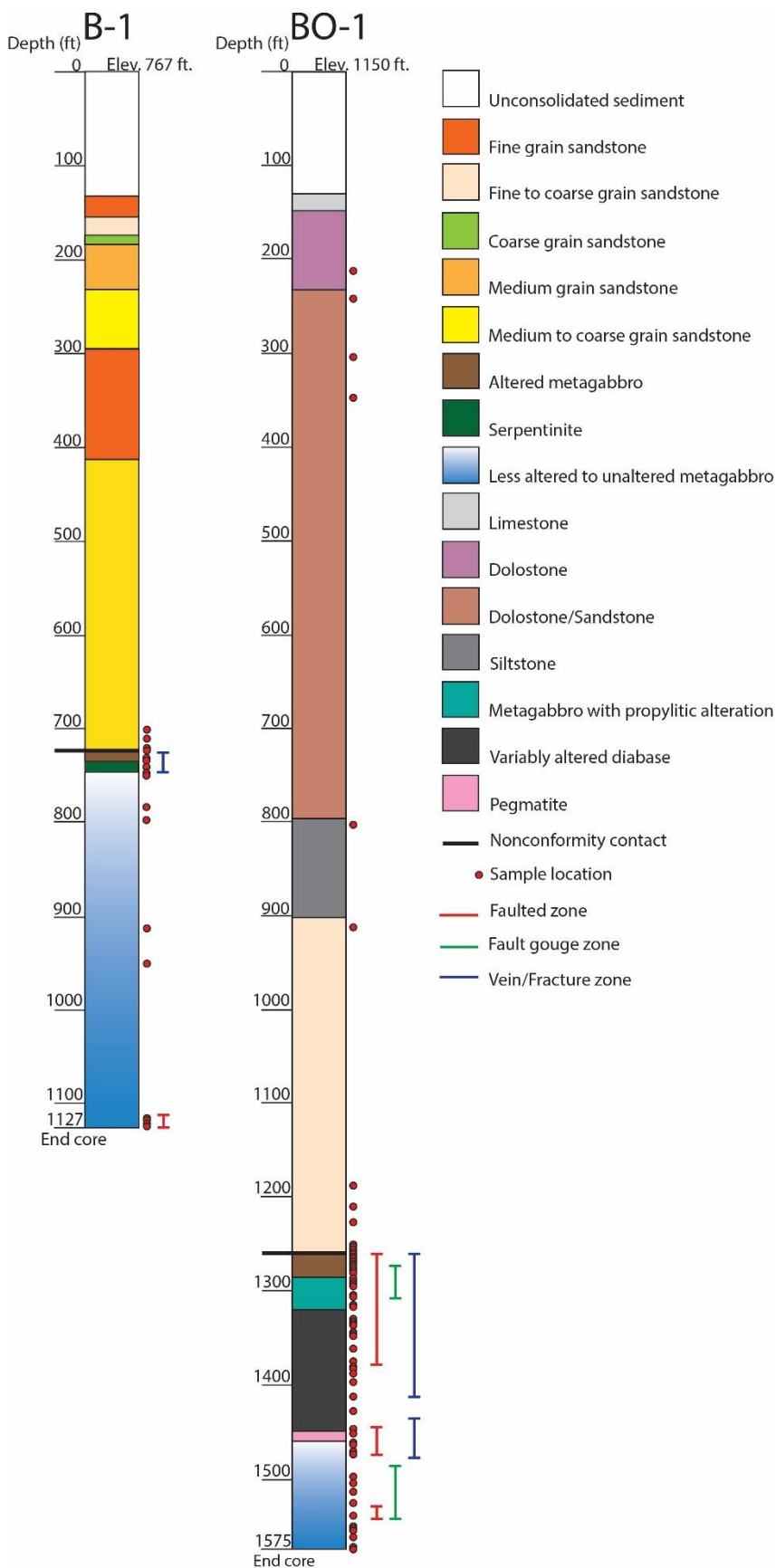


Figure 1: Initial lithology of the B-1 and BO-1 drillcores based on meso-scale core logging observations and historical drilling records. Red dots to the right of the columns indicate sample locations. Colored bars to the right of the columns indicate structural features.

3.4 Gunnison, Colorado: A Structural Analog

Many unconformities between Precambrian basement rock and younger sedimentary rock are exposed in the vicinity of Gunnison, Colorado and provide an opportunity to examine the 3-dimensional structural geometry and permeability architecture of a nonconformity contact. The Gunnison County region displays both faulted and depositional nonconformity contacts between Precambrian basement rocks and Jurassic to Cretaceous primarily siliciclastic units. The basement rocks are gneiss, amphibolite, quartzite, and schist metamorphosed at ~1.7 Ga with granite and diorite intrusions (Afifi, 1981; Steven and Hail, 1989; Kellogg, 2004; Stork et al., 2006).

The oldest basement rocks are the Proterozoic (~1.7 Ga) Dubois greenstone (Afifi, 1981). The basement rocks show evidence for two generations of folding associated with the Boulder Creek Orogeny, which corresponds with the metamorphism to amphibolite facies conditions. Layers of gabbros and diorites intruded in the area and were later metamorphosed to amphibolites. Porphyritic varieties of the lithologies crystallized at chilled margins or in dikes. Precambrian basement lithology is variable due to differentiation of magma and multiple phases of deformation (Afifi, 1981).

The region surrounding Gunnison is called the Gunnison Uplift, which was faulted during the Laramide orogeny, producing low angle (<45°) reverse faults creating basement cored uplifts (Kellogg, 2004 and references therein). This is a unique setting because previous records of nonconformity characterizations have not included reverse faulted contacts. Prominent faults near Gunnison include the Ute Indian Fault, Cimmaron Fault, and Red Rocks Fault (Kellogg, 2004). The Ute Indian Fault is a well exposed, west dipping reverse fault displaying up to 350 m of displacement. The Cimmaron and Red Rocks Fault

are steeply dipping reverse faults which border the southwestern side of the Gunnison Uplift.

The Gunnison fault is a southwest dipping reverse fault exposed at Hartman Rocks Recreation Area and parallels the Gunnison syncline (Figure 2). The fault separates the Brushy Basin Member of the Jurassic Morrison Formation and undifferentiated Paleoproterozoic amphibolite, biotite quartz schist, and South Beaver Creek tonalite (Figure 2; Stork et al., 2006). The fault borders the northeastern side of the Gunnison annular complex, which is an 8-km diameter intrusive body composed of Proterozoic sheet dikes surrounded by metamorphosed host rock (Lafrance and John, 2001). Other Jurassic/Proterozoic contacts in western Gunnison County region are depositional rather than faulted (Steven and Hail, 1989; Streufert et al., 1999).

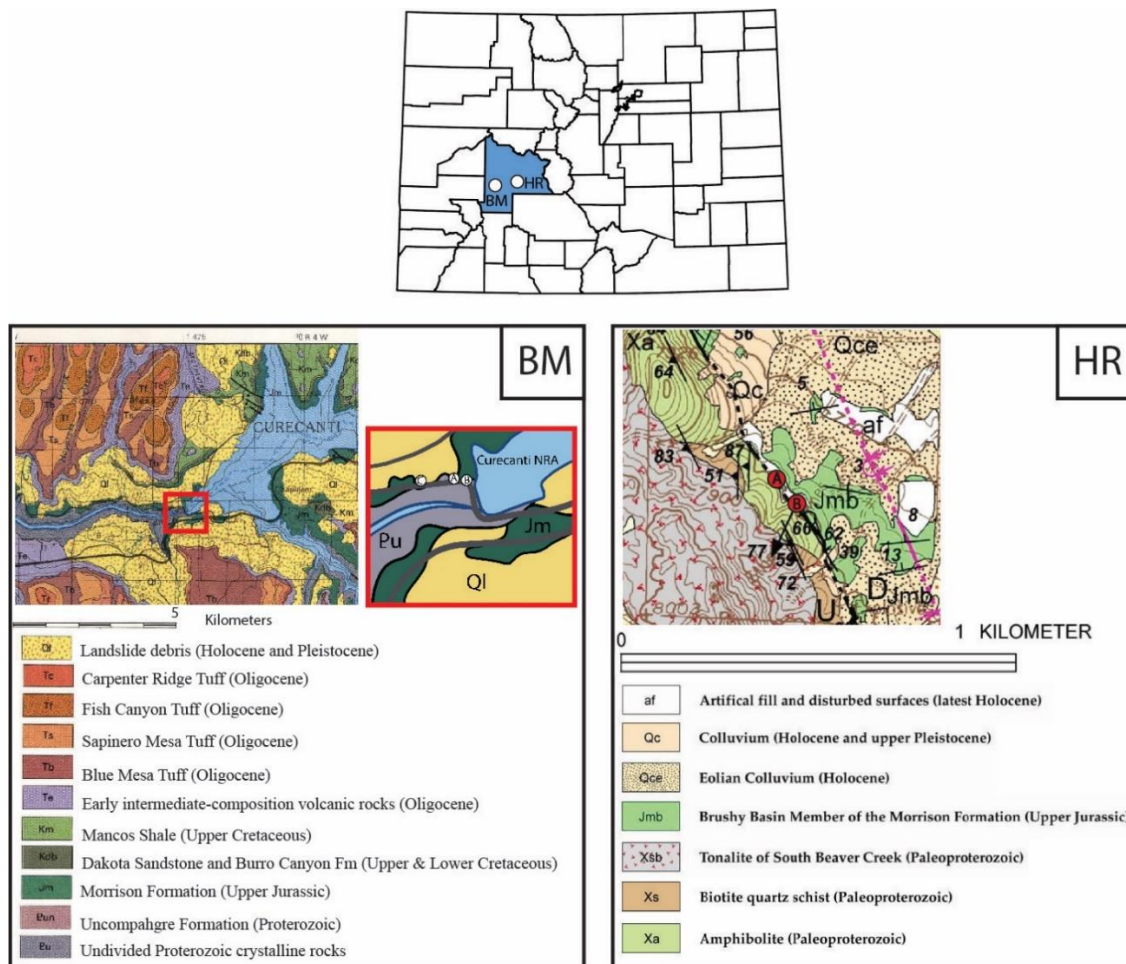


Figure 2: Gunnison, CO field site geology. Geologic map of the Gunnison County field area. Site locations are marked with white dots on the county map of Colorado. Lower Image Left: Geologic map of the Blue Mesa Dam (BM) region adapted from Steven and Hail (1989) with 50 m contour intervals. The field site is marked with a red box and specific sites labelled in the inset. Lower Image Right: Hartman Rocks (HR) field site adapted from Stork *et al.* (2006). The black NW-SE trending line is the Gunnison Fault, parallel to which is the Gunnison Syncline marked with a pink line. Contour interval is 20 ft.

4. METHODOLOGY AND WORKFLOW

To understand how rock structure controls fluid flow and thus alteration, we examined the relationships between composition, structure, and permeability/porosity of drillcore samples crossing the nonconformity. We use an integrative field and analytical approach focused on determining cm- to μm -scale variations to infer petrophysical rock properties, fluid-rock interactions, and how fluid migration potentially impacts the interface contact in this setting (Figure 3). The analyses in this thesis expand on prior work (Table 1; Cuccio, 2017; Hesseltine, 2019; Petrie et al., 2020) and will be used in on-going studies or future hydrologic modeling efforts.

Field and core samples examined here were selected based on documenting lithologic variations, the presence of structural features (faults, fractures, veins, fabric), and/or the nature of alteration. Samples from two drillcores and two field study sites were examined to address the broader goals of nonconformity characterization, however, only a subset of the samples from BO-1 drillcore are thoroughly examined for compositional and textural variations.

The primary focus is on 25 samples from the BO-1 drillcore that we extracted for permeability measurements and that span a nonconformity interface contact. We compare these results and correlate their relationship to observed structural features, alteration, and mineralogy. The Minnesota drillcores and the data produced from those samples are presented in Chapter 2 as a paper in preparation for submission to a scientific journal.



Figure 3: Visual methods summary: A) Individual samples are selected from the drillcore with a focus on changes in lithology, alteration zones, or structural features such as faults, veins, and fractures; B) Locations for thin sections (black rectangle) and relative porosity and permeability testing (red) are noted; C) In addition to petrographic analysis to determine mineralogy, alteration phases, and micro-structures, plane polarized thin sections impregnated with blue fluorescent dye are examined to document pore spaces and fractures.

4.1 Sample Acquisition and Core Logging

The initial core logging and sampling of drillcores BO-1 and B-1 took place in August 2017 by Drs. Kelly Bradbury and Katie Potter. Samples were acquired from the Minnesota Department of Natural Resources Drill Core Library (MN Department of Natural Resources, 2020) in Hibbing, MN with assistance from Nicholas Niemi and Barry Frey as part of a collaborative project between USU and USGS scientists. These cores were selected for analysis because they are the closest drillcores to the Northeast Iowa Intrusive Complex, which is targeted by the USGS for a future Scientific drilling project. Refer to Chapter 2 section 3.1 for additional details on the Minnesota core acquisition and characterization. When discussing depths, SI and imperial units are given because the original drillcore data is recorded in imperial units.

4.2 Field Work: Gunnison Analog Outcrops

We conducted fieldwork near Gunnison, Colorado in July 2019 to visualize and further document the range of rock property variations as a function of structural and permeability architectures that may exist across faulted nonconformity contacts. Numerous major faults are exposed in this region and dissect various portions of the unconformity, separating Jurassic sedimentary rocks from Precambrian igneous and metamorphic rocks (Manger, 1963). The range of lithologic compositions and structural complexity of the sites are ideal for examining the kilometer to sub-meter scale spatial variations that are analogous to the heterogeneous nonconformities occurring at injection depths in Oklahoma (Ham et al., 1964; Kolawole et al., 2019).

The goal for the field work was to map the spatial relationships between faults, the unconformity contact, and any associated alteration or weathering. The two primary locations for this field work were Hartman Rocks Recreation Area and Blue Mesa Dam (Figure 2). We conducted two horizontal transects across a fault at Hartman Rocks and we conducted two vertical transects across the nonconformity contact at Blue Mesa Dam. Samples were selected based on changes in alteration and lithology. We collected 29 samples from Hartman Rocks and 15 samples from Blue Mesa Dam. Due to the scope and direction of this thesis, the Gunnison samples became a part of Anna Paulding's senior URCO project and are not included in the primary data analysis in Chapter 2.

4.3 Petrographic Analysis

A total of 84 petrographic thin sections were selected from hand samples to identify mineralogy, deformation textures and fabrics, and the potential generations of cementation and vein infillings across the non-conformity interface. Of the thin sections, 12 are from Blue Mesa Dam, 19 are from Hartman Rocks, 14 are from B-1 drillcore, and 39 are from BO-1 drillcore. There are 26 thin sections in BO-1 drillcore which have corresponding permeability measurements. All thin sections were impregnated with a blue dye aid in quantifying porosity. The BO-1 drillcore thin sections were also impregnated with fluorescent dye to emphasize the presence of cements and fracture/vein infillings, which may be useful for understanding fluid history and the relative timing of structural diagenesis and porosity evolution in future studies (Yanguas and Dravis, 1985).

For petrographic analyses, I used the Leica Z16 APO and Leica DM 2700 P and petrographic microscope outfitted with a CoolLED *pE-300*^{white} light for fluorescence

microscopy at the USU Geoscience Petrography Lab. I also used a Leica Z16 APO microscope with the Leica Application Suite (LAS) software for photographing entire thin sections and a Leica DM 750 P for photomicrographs using a Nikon D750.

4.4 Porosity and Permeability Measurements

Porosity and permeability measurements were conducted on BO-1 drillcore only. The B-1 drillcore size was too small for conducting laboratory permeability testing. A complete detailed description of the methodology is presented in Chapter 2 section 3.3 (Appendices A & B).

4.5 Whole Rock Mineralogy and Geochemistry

Whole rock X-ray diffraction (XRD), X-ray fluorescence (XRF), and inductively coupled mass spectrometry (ICP-MS) methods were conducted to determine elemental and mineralogical variation across the drillcore and outcrop analog sites. Host rocks, lithologic contacts, fractures, slip surfaces, weathered horizons, and alteration zones were subsampled to document spatial variations and relative abundance in alteration products and assemblages such as clays, carbonates, sulfates, and oxides. We used the mineralogic and elemental composition results to understand alteration related to deformation and to infer fluid rock interaction and how these types of analog settings can impact future fluid migration. Twenty samples from B-1 drillcore, 79 samples from BO-1 drillcore, and 33 samples from the Gunnison outcrops were processed and analyzed using the PANalytical X'Pert PRO XRD machine at USU Geosciences X-ray Diffraction Lab. See Chapter II section 3.4 for additional information.

We selected 20 of the 25 samples with permeability measurements to analyze with XRF and ICP-MS methods as well as 11 additional samples from BO-1 drillcore and 18 samples from the Hartman Rocks site. These samples were analyzed to quantify variations in major, minor, and trace elements. These samples were processed at the Washington State University Peter Hooper GeoAnalytical Lab using their established methods (<https://environment.wsu.edu/facilities/geoanalytical-lab/>). Whole rock samples were chipped and crushed to a homogenous powder in a tungsten carbide bowl for two minutes in a ROCKLABS Standard Ring Mill. Powder samples (~4 g each) were mixed and fused with twice the amount of Merck Spectromelt (di-lithium tetraborate, ~8 g) into glass beads, re-crushed, and then re-fused for analysis.

The field samples were analyzed *in situ* and in the lab using a Bruker Tracer III-V portable XRF to measure variations in major and trace elements due to weathering and/or alteration. The field data was processed by Anna Paulding as part of her USU undergraduate thesis and provides additional geochemical data to support the interpretations of structurally-controlled alteration and permeability architecture at the field sites.

CHAPTER II

Manuscript: Geologic characterization across the sedimentary bedrock – crystalline basement nonconformity interface from two drillcores in SE Minnesota

Authors: Kayla Smith, Kelly Keighley Bradbury, and James Evans

Institutional Mailing Address: 4505 Old Main Hill, Department of Geosciences, Utah State University Logan, UT 84322-4505

Email addresses: Kelly.bradbury@usu.edu

ABSTRACT

The pattern of recent increased seismicity in the midcontinent region of the United States is attributed to high volumes of injected wastewater reactivating subsurface faults at ~ 1 – 5 km depth near the Paleozoic sedimentary - Precambrian crystalline basement rock nonconformity contact. While much is known about the potential causes of induced seismicity, comparatively little is known about the geology, geochemistry, and inferred hydrogeologic structure of this interface region and how these factors may impact the permeability architecture and mechanical rock properties. In this study, we examine rock properties of two drillcores that intersect the nonconformity and document the presence of a ~6-22 m thick altered/weathered horizon below the nonconformity between the Mount Simon Sandstone and Precambrian amphibolite. This hydrogeologically distinct horizon is intensely faulted and fractured, semi-permeable (<1 - 443 mD). Petrographic and XRD analyses show the composition of this horizon is dominated by mechanically weak secondary mineralization, including carbonates and phyllosilicates. This horizon also

differs in its major oxide geochemistry and LOI compared to the relatively unaltered protolith. We provide a comparative set of detailed mineralogy, structures, geochemistry, porosity values, and lab permeability measurements that can be used to provide constraints and inform hydrologic models for fluid injection and migration proximal to the nonconformity interface.

1. INTRODUCTION

Induced earthquakes are triggered when anthropogenic activity, coupled with stress state variations within the crust, result in seismic slip on a pre-existing fault or fracture (Ellsworth, 2013; Foulger et al., 2018). Induced seismicity is attributed to a variety of industrial practices such as wastewater injection, pressure loading from construction activities or reservoir filling, or material removal from mining (Van Poolen and Hoover, 1970; Zoback and Harjes, 1997; Deichman and Giardini, 2009; Doglioni 2017; Foulger 2018; Hincks et al., 2018). Over the past decade, the midcontinent region of the United States has experienced a sharp increase in the frequency and magnitude of earthquakes with $M_w > 3.0$, particularly in Colorado, Kansas, Oklahoma, and Texas (Frolich, 2012; Ellsworth, 2013; Zhang et al 2013; Rubinstein and Mahani, 2015; Foulger et al., 2018; USGS, 2018). This uptick in seismic activity has been attributed to increased rates and volumes of wastewater fluids injected into wells targeting porous sedimentary bedrock that directly overlie Precambrian crystalline basement rocks (Keranen et al., 2013; Walsh and Zoback, 2015; Scales et al., 2017). This wastewater is a byproduct of hydraulic fracturing and other oil and gas production processes and is injected into Class II wells as a method of disposal (EPA, 2017).

High-pressure fluid injection may cause ancient, previously inactive faults to rupture due to: 1) fluids reducing frictional resistance on the fault surface, or 2) pore fluid pressures decreasing the shear strength on a fault (Doglioni, 2017; Foulger et al., 2018). Associated pore pressure changes during migration of injected fluids and rock property changes due to fluid-rock interactions may result in dynamic weakening of faults (Lachenbruch, 1980; Maurer et al., 2020) and cause earthquakes many km's from injection sites (Keranan et al., 2014; Zhang et al., 2016; Peterie et al., 2018). Moreover, induced earthquakes can occur months after injection depending on how much pressure loading on a fault is required for rupture (Deichman and Giardini, 2009; Zhang et al., 2016). The largest recorded induced earthquake in the midcontinent region is a M_w 5.8 in Pawnee, OK which occurred in 2016 and caused millions of dollars in damage (Jones, 2016; USGS, 2019). Fault geometry complexities and interconnected structures may also exert a greater control on rupture size than the volume of injected fluid (Maurer et al., 2020). The relationship between structures and alteration is known as "structural diagenesis", however studies on structural diagenesis typically relate to sedimentary rocks and not the crystalline basement rocks where the induced seismicity is concentrated (Laubach, 2010).

Hydrologic modelling of injected fluids at depth in the midcontinent region indicates fluid pressure migration is controlled by the permeability architecture of the basement rock (Stober and Bucher, 2007; Zhang et al., 2016; Goebel and Brodsky, 2018; Ortiz et al., 2018; Yeyha et al., 2018; Kolawole et al., 2019). However, knowledge of the geologic conditions of the basement rocks within the midcontinent region is limited, particularly as it relates to alteration composition, geometry of fault and fracture systems, and their spatial distributions. Pre-existing fluid-rock interactions can lead to diagenetic

alteration, pore pressure communications, and pore fluid volume changes that affect rock mechanical properties (Laubach et al., 2010). Failing to incorporate diagenetic features into geophysical or hydrologic modeling will over-estimate fault stability and not properly quantify the potential for fault reactivation (Kibikas et al., 2019). As such, the in-situ subsurface geologic conditions are critical for understanding chemical and physical interactions between rocks and injection fluids, and thus influence the location of induced seismicity (Cuccio, 2017; Callahan et al., 2019; Hesseltine, 2019; Kolawole et al., 2019; Petrie et al., 2020).

Here, we examine micro- to meso-scale compositional and textural variations in whole rock samples from two SE Minnesota drillcores as a representative injection analog site for the midcontinent region. We assess rock property heterogeneities and the spatial distribution of structural features in a vertical transect across nonconformity interfaces at ~ 0.5 – 1.5 km depth. We use detailed drillcore characterization, petrography, whole-rock mineralogy and geochemical analyses, and permeability measurements to document changes in lithologic composition, weathering, alteration, structural features, fabrics, and textures from the meso- to micro-scale. Our results provide critical geologic constraints for determining permeability and rheologic properties of the nonconformity boundary and thus contribute to refined inputs for hydrologic, hydromechanical, and/or seismic risk models for similar subsurface geologic settings.

2. GEOLOGIC CONTEXT

2.1 Induced Seismicity

The Great Unconformity, first identified by Powell *et al.* (1875) in the Grand Canyon, is defined as the nonconformity of Proterozoic metamorphic or igneous rock overlain by lower Paleozoic rock which extends across much of the United States (Sloss, 1963; Peters, 2006; Peters and Gaines, 2012). This contact is frequently exposed in the western US with limited exposures across the midcontinent (e.g., DeLucia *et al.*, 2017; Kolawole *et al.*, 2019), where the contact primarily lies at depth (Sims, 1990; Karlstrom and Timmons 2012). Multiple complex metamorphic and igneous terrains and fault systems underly the midcontinent from the surface to the basement rocks (Sims 1990; Whitmeyer and Karlstrom, 2007; Murray, 2015; Marsh and Holland, 2016) and much of the seismicity in the midcontinent area occurs around ancient faults proximal to this sedimentary bedrock - crystalline basement nonconformity interface contact (Zhang *et al.*, 2013; Walsh and Zoback, 2015; Hinks *et al.*, 2018; Kolawole *et al.*, 2019). For example, the M_w 5.8 earthquake in Pawnee, OK ruptured along a previously unmapped basement fault in response to fluid injection and increased pore pressures or stress perturbations (Chen *et al.*, 2017).

The nonconformity may exhibit a dominant hydrological control on wastewater fluid flow pathways because it can enhance or impede lateral migration of pore fluid pressures to faults in the Precambrian basement (Zhang *et al.*, 2013; Ortiz *et al.*, 2018; Petrie *et al.*, 2020). This lateral migration can lead to seismic events from m's to 10 km's away from an injection site (Ortiz *et al.*, 2018; Chen *et al.*, 2017), with some earthquakes

associated with injection sites reported up to 90 km's away (Peterie et al., 2018). Characterizing the nonconformity geology is challenging because the contact is typically buried in the midcontinent area, and therefore knowledge is limited about its structure and alteration at depth. Drillcores that intersect this contact are also sparse, few have been studied in detail, and are distributed among a range of libraries with variable quality in documentation. Where available and well-documented, they provide an excellent opportunity to study and sample the *in-situ* rock properties and structure adjacent to the nonconformity interface contact.

2.2 Previous Work

Surveys of multiple drillcores and outcrops that sample or provide access to the nonconformity yield a variety of lithology combinations, degrees of alteration, and variable fault and fracture intensities in the nonconformity zone (Cuccio, 2017; Hesseltine, 2019; Petrie et al., 2020). The Great Unconformity contact geometries may be complicated due to faulting, hydrothermal alteration, and past differential erosion of the Precambrian basement which creates significant topography along the nonconformity contact (Sims, 1990) or localized permeability changes due to laterally discontinuous zones of alteration (Petrie et al., 2020). Permeability can also vary over time due to the chemical interaction between fluids, including injection brines, and the bedrock (Cuccio, 2017). Furthermore, laterally discontinuous and/or localized low permeability zones may funnel pore pressures to greater depths within the crystalline basement (Petrie et al., 2020). Fluid flow in the crystalline basement is typically facilitated by faults and fractures (Hickman et al., 1995;

Caine et al., 1996; Boullier et al., 2004), however deep fluid circulation can occur without fracture permeability (Cuccio, 2017).

Petrie *et al.* (2020) identified 3 generalized end-member nonconformity types and described potential modifications of poroelastic behavior and the transmission of pore fluids for each. The first end member (Type 0) is a sharp depositional contact with little to no alteration. The Type I contact is dominated by phyllosilicate alteration and Type II is dominated by secondary non-phyllosilicate mineralization. All end member contact types may also contain faults that either terminate at the boundary or extend into the sedimentary cover. Complex fault geometries may enhance or inhibit the downward migration of injection fluids (Bense et al., 2013; Petrie et al., 2020). Altered and weathered nonconformities may inhibit seismicity because they deform by granular flow rather than brittle deformation (Kerner, 2015)

2.3 B-1 and BO-1 Drillcore Analogs

Our focus is on a nonconformity contact where porous sandstone overlies mafic crystalline basement associated with the Midcontinent Rift (MCR) in southeastern Minnesota (Drenth et al., 2020). We describe the rocks in the boreholes and provide detailed permeability and mechanical rock property measurements at the sub-meter scale, which are needed to quantify how heterogeneous lithologies, structure, and alteration may affect fluid migration (Hesseltine, 2019; Kolawole et al., 2019). Two boreholes (B-1 and BO-1) were drilled in the southeast corner of Minnesota in Fillmore County as a part of exploratory mining projects in 1962 and 1984. This project targeted geophysical anomalies interpreted to indicate the presence of iron and titanium mineral deposits in the crystalline

basement rock (Figure 1; Gilbert, 1962; Drenth et al., 2015; Drenth et al., 2020; MN Department of Natural Resources, 2020). Both drillcores sampled the lower Cambrian Mount Simon Sandstone which overlays Precambrian mafic rocks and layered diabase and granitic dikes of the NE Iowa Intrusive Complex (NEIIC) which is associated with the Midcontinent Rift System (MRS; Anderson, 2012; Drenth et al., 2015; Drenth et al., 2020). The drillcores are ~ 28 km apart at the surface and have a ~ 47 m difference in depth between where they intersect the Precambrian nonconformity.

Suspected basement faults near the boreholes were identified by magnetic lineaments and align with the NW-SE trending Belle Plaine Fault Zone (BPFZ) (Drenth et al., 2015; Drenth et al., 2020). The BPFZ are pre-MRS faults which generally display strike-slip movement and controlled the location of the NEIIC (Drenth et al., 2015). Possible extent of structures into Paleozoic sedimentary rocks is uncertain because the sedimentary cover is not expected to produce geophysical anomalies as is seen in the basement rocks (Drenth et al., 2020). Some areas of these fault systems were active post-Ordovician, as identified in structures through Cambrian and Ordovician sedimentary units which align with the basement structures identified in the geophysical data (Sloan and Danes 1962; Bloomgren, 1993; Allen, 1994). Basement faults which intersect, and/or trend perpendicular to the BPFZ display a vertical offset of up to ~60 m and can extend into the sedimentary cover (Morey, 1977).

The B-1 and BO-1 drillcores are analogous to several other midcontinent injection sites such as the subsurface in Oklahoma, because the Precambrian crystalline basement in Fillmore County is separated from lower Cambrian to upper Ordovician sedimentary strata by the Great Unconformity (Gilbert, 1962; Mossler, 1995). Additionally, the Mount Simon

Sandstone featured in this study is targeted for CO₂ storage, compressed air storage, and wastewater injection (Dewers et al., 2013; Wang and Bauer, 2017), and is at risk of producing an induced seismic event with enough pressure loading (Zhang et al., 2013). This is not a unique situation as several other units targeted for waste injection in the midcontinent region have also experienced injection-induced earthquakes (Wickstrom et al., 2010; Kaven et al., 2014; Abousif, 2015).

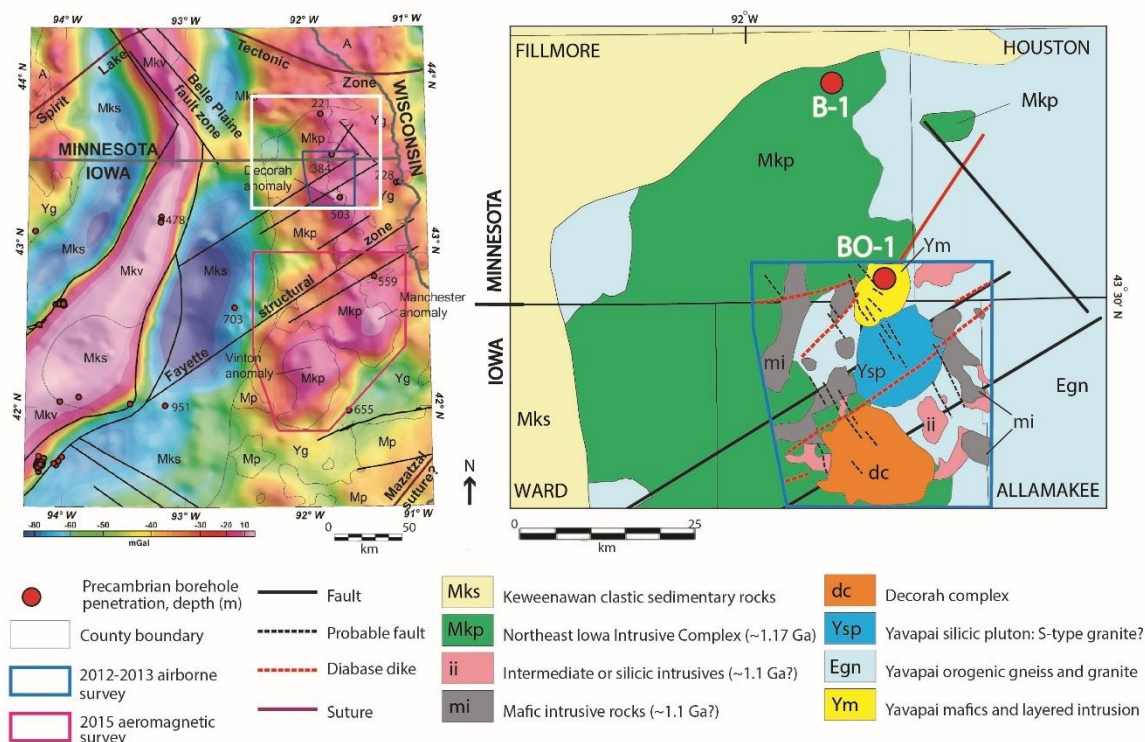


Figure 1: Location and geologic setting of B-1 and BO-1 drillcores in Fillmore County, MN. Figure modified from Drenth et al. (2015, 2020) and Anderson (2005). Left map: complete Bouguer Ground gravity data with background hillshade of reduced-to-pole aeromagnetic data. The Decorah Complex is a part of the Northeast Iowa Intrusive Complex where the Belle Plaine Fault Zone facilitated its emplacement. White box marks the inset of the right map. Right map: inset showing the basement Precambrian geology. Faults (black solid and dashed lines) may be associated with the SW-NE-trending Fayette Structural Zone or the NW-SE-trending Belle Plain Fault Zone to the southwest or northwest of BO-1 respectively (Drenth et al., 2020; Drenth et al., 2015; Anderson 2005). The BO-1 and B-1 boreholes are ~28.5 km apart.

3. METHODS

To document μm - to m-scale variations in physical and chemical properties relating to fluid flow, we use an interdisciplinary analytical approach including detailed core logging, petrography, whole-rock mineralogy and geochemistry, and mini-permeameter permeability measurements. The analyses presented in this paper expand on previous work (Cuccio, 2017; Hesseltine, 2019; Petrie et al., 2020) and offer a new suite of data for comparison to other nonconformity observations. We compare results between methods to identify patterns between lithology, structural deformation, alteration, and fluid-rock interactions along the nonconformity contact at depth. The analyses conducted in this study focus on around 59 rock core and chip samples. In total, the dataset for the BO-1 drillcore includes 39 petrographic thin sections, 25 permeability and porosity values (Appendix A & B), 73 X-ray diffraction (XRD) measurements (Table 1), and 31 X-ray fluorescence (XRF) measurements (Appendix C). The B-1 drillcore has 16 rock core and chip samples, 14 petrographic thin sections, and 20 XRD measurements (Table 2).

3.1 Sample Acquisition and Detailed Drillcore Characterization

The B-1 drillcore (elevation: 767 ft / 234 m; UTM: 15N 591298 4848017; MN Unique Well #219446) was extracted in 1962 and the BO-1 drillcore (elevation: 1150 ft / 351 m; UTM: 15N 598575 4820583; MN Unique Well #20102) was extracted in 1984 for mineral exploration. The B-1 drillcore is 3.64 cm in diameter (BQ) and the BO-1 drillcore is 4.76 cm in diameter (NQ). Boreholes are azimuth-unoriented and assumed vertical when reporting depths below ground surface. Drillcore depths were originally reported in feet

and converted to meters for the purpose of this study. Samples for this study were acquired in August 2017 from the Minnesota Department of Natural Resources Drill Core Library (MN Department of Natural Resources, 2020) in Hibbing, MN. The B-1 and BO-1 drillcores were selected as nonconformity interface analogs because: 1) the nonconformity is comparable to depths that are common injection intervals within midcontinent region; and 2) they provide a continuous vertical transect across the nonconformity which excludes the interference of modern surface weathering and alteration. A total of 17 samples were collected over ~127 m from the B-1 drillcore with 59 total samples from ~120 m of the BO-1 drillcore. Samples were collected to capture variations in lithology, weathering, alteration, and structural features. Whole-rock and rock chip samples were further subdivided for a range of physical and chemical laboratory analyses.

Detailed core logging and characterization included recording lithologic composition, weathering, alteration zones, and documentation of textures (foliation and fabric) and structural features (faults, fractures, veins) with dip angles measured assuming a vertical core axis (see Data Repository). Locations of structural features in areas of the drillcore not sampled were estimated using photographs of the drillcore in original storage boxes. We used the mineralogic and elemental composition results to understand alteration related to deformation, infer fluid rock interactions, and understand how these types of analog settings may impact future fluid migration related to wastewater injection practices.

3.2 Petrographic Analysis

A total of 53 petrographic thin sections were prepared from hand samples to identify mineralogy, alteration, vein infillings, deformation textures and fabrics and across the non-conformity interfaces intersected by B-1 (14 samples) and BO-1 (39 samples) drillcore. All thin sections were impregnated with a blue dye to highlight pore spaces. For petrographic analyses, we used the Leica Z16 APO and Leica DM 2700 P and petrographic microscope outfitted with a CoolLED *pE-300^{white}* light for fluorescence microscopy at the USU Geoscience Petrography Lab. We also used a Leica Z16 APO macroscope with the Leica Application Suite (LAS) software for photographing entire thin sections and a Leica DM 750 P for photomicrographs using a Nikon D750 camera.

3.3 Hydrogeologic Properties

3.3.1 Permeability

Twenty-five samples from BO-1 drillcore were selected for gas permeability testing through Schlumberger Rock Mechanics and Core Analysis Services (Appendix A). Drillcores were split vertically using a saw and permeability measurements were made in steady state conditions with a mini permeameter where N₂ gas is injected directly onto the core slab surface. Each sample had 5 permeability sub-sample sites and each measurement was made twice. Sampling sites were chosen based on changes in lithology, structure, or texture. The measurable permeability range for the profile permeametry system is between 0.01 mD – 3000 mD. Results in the text are described on a scale relevant for hydrologic model inputs and rounded to the nearest whole number. Values are reported as the mean of

each permeability sub-sample site ($N = 2$) averaged across each sample ($N = 5$) \pm the standard deviation. Refer to Appendix A for raw data. We compare permeability values to the composition and structural deformation features we observed at both the meso- to micro-scale.

3.3.2 Porosity

The 25 samples selected for permeability testing have 26 corresponding thin sections which were analyzed with ImageJ software to estimate porosity using the jPOR macro addition, following the methods reported in Grove and Jerram (2011). The thin sections were scanned at 4800 DPI using an Epson Perfection v850 Pro film scanner. Images were processed in Adobe Photoshop by converting the image to an 8-bit color palette designed for jPOR and cropped to leave display only inter-sample pore spaces. This yields a 2σ counting error which is negligible ($\pm 0.039\%$) compared to He injection porosimetry as opposed to up to $\pm 3.8\%$ associated with point counting. When using this method, reported values varied by an average of 1.2% of the jPOR result. Values of the dataset here are reported with $\pm 1.2\%$ of the jPOR assigned value to account for account for possible sources of variability (Grove and Jerram, 2011).

In addition to jPOR counting error and inter-operator variability, an additional potential source of error includes the imaging systems used. Issues such as exposure, color balance, and chromatic aberration are present in any image capturing system to varying degrees, which can exaggerate or diminish the blue pixels selected in this program. In our thin section slides, we noticed the imageJ program would falsely identify pore spaces in the grain boundaries between high contrast dark minerals and light matrix, likely due to chromatic aberration caused by the scanner. We currently do not have a way to quantify

this error and we did not perform a point counting test of our thin sections for comparison, so we rely on the 1.2% error reported by Grove and Jerram (2011) and acknowledge that the precision and porosity may be overestimated. Refer to Appendix B for raw data.

3.4 Whole Rock Mineralogy and Geochemistry

Whole rock X-ray diffraction (XRD), X-ray fluorescence (XRF), and inductively coupled mass spectrometry (ICP-MS) methods were conducted to determine mineralogical and elemental compositions across the drillcore analog sites. Host rocks lithology, contacts, fractures, slip surfaces, weathered horizons, and alteration zones were sub-sampled to document spatial variations and relative abundance in alteration intensity and assemblages such as clays, carbonates, sulfates, sulfides, and oxides and hydroxides.

3.4.1 X-ray Diffraction

Twenty samples from the B-1 drillcore and 73 total samples and sub-samples from the BO-1 drillcore were processed and analyzed using the PANalytical X'Pert PRO XRD machine at USU Geosciences X-ray Diffraction Lab (Tables 1 & 2). 10-20 g of rock material per sample were crushed to a homogenous powder in a tungsten carbide bowl using a ROCKLABS Ring Mill Pulverizer in USU's Rockprep Lab. 1 g of whole-rock powder sample material was analyzed in an aluminum sample plate from 2-75° at 45 kV and 40 mA at one second per 0.02° step increments. Mineral phase identification was interpreted using the PANalytic X'Pert HighScore program version 4.5 and the ICDD PDF-4+ Inorganic database of reference patterns. The range of potential mineral phases were further refined based on the XRF data results and petrographic analysis. Mineral candidates

with high scale and score factors were prioritized, then phases were user-matched to the position and intensity of the reference patterns match to sample peaks. We did not perform a clay-specific XRD analysis, however, some samples where clay is abundant, the clay mineral phases were identified based on a match to reference patterns.

3.4.2 X-ray Fluorescence

We selected 20 of the 25 samples with permeability measurements to conduct XRF and ICP-MS analysis as well as 11 additional samples from BO-1 drillcore. Samples were processed at the Washington State University Peter Hooper GeoAnalytical Lab using their laboratory facilities and following their sample processing and analysis protocols (Johnson et al., 1999) (Appendix C). Around 10 g of rock chip material per sample was powdered and homogenized in a tungsten carbide Rocklabs Standard Ring Mill. 4.0000-4.0050 g of powder sample is combined with twice the sample weight of Merck Spectromelt (dilithium tetraborate) \pm 0.0020 g. Samples are fused for 10 minutes at 1000 °C, then crushed again and re-fused after 0.05-1.00 g of powder have been removed from the re-ground sample for loss on ignition (LOI) analysis. Samples were analyzed using a ThermoARL Advant'XP+ XRF spectrometer. XRF data is reported as unnormalized with no decimal places in the text, refer to Appendix C for raw data. Depending on the element, the uncertainty in the data ranges from 0.00-0.31% based on a repeat of sample BO-1_1263.65. Comparison of elemental variation patterns within the samples was conducted using a Bootstrapping statistical analyses of the XRF data was conducted and calculated at the 90% confidence level in MATLAB using an open access code provided by Randolph Williams (University of Wisconsin, pers. comm., 2021). This method randomly re-samples from the

dataset with 1500 iterations to better estimate the distribution within a particular sample population (Sohn and Menke, 2002).

4. RESULTS

The BO-1 drillcore has the most complete suite of analyses, so we focus our results on these samples with a brief overview of the B-1 drillcore towards the end of this section. We define three distinct geologic or hydrogeologic units within the drillcore based on detailed compositional and structural characterization of the ~120 m of BO-1 drillcore. These are: 1) sedimentary bedrock units composed of medium – to fine-grained sandstones and siltstones above the nonconformity interface; 2) the altered interface region which consists of a Precambrian amphibolite with three separate zones of alteration: upper phyllosilicate zone, lower phyllosilicate zone, and a transition zone from the altered region; and 3) amphibolite and a layered intrusive complex below the nonconformity interface (Figures 2 - 4). A minimum of ~ 22 m of altered mafic protolith occurs below the nonconformity boundary in the BO-1 drillcore. Permeability and porosity vary from the meso- to micro-scale, however, permeability is highest immediately proximal to the nonconformity contact (Figure 5). Below the nonconformity, permeability is extremely low, with the exception of localized and structurally-controlled, high permeability values. The areas of intense alteration at, or adjacent to, the nonconformity boundary also corresponds with higher levels of loss on ignition in XRF and high elemental variability (Figures 6-8). For each of these zones, we describe the mesoscopic composition and structure (Figure 2 & 3), the petrography (Figure 4), porosity and permeability (Figure 5), and the lithologic, elemental, and mineralogical compositions (Figures 6-10; Table 1).

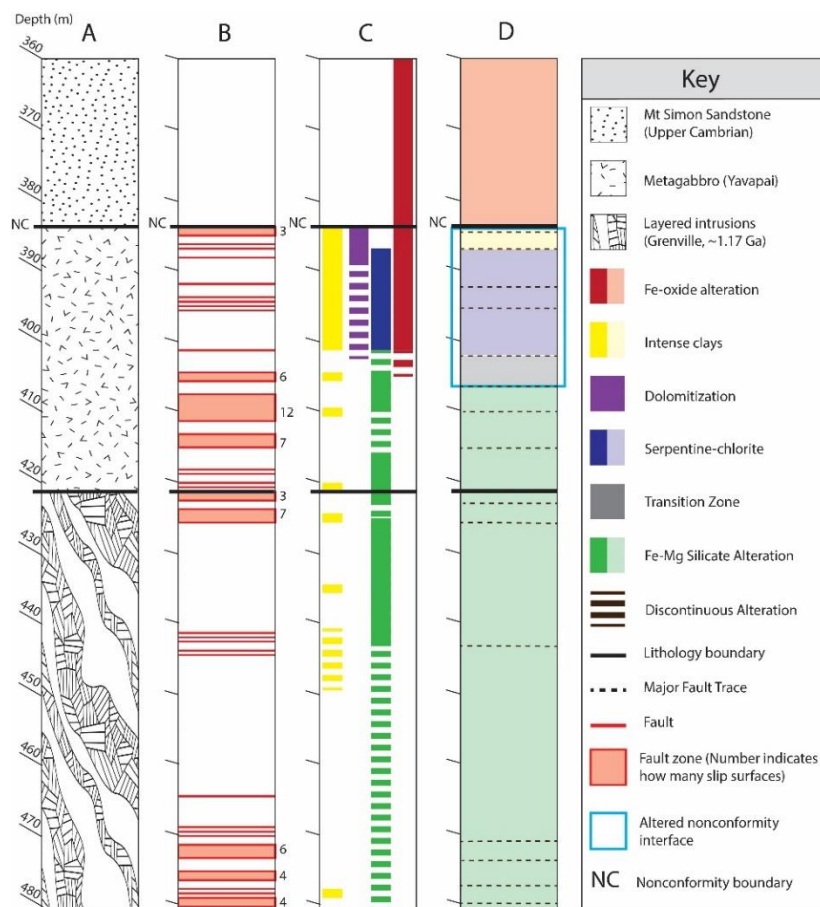


Figure 2: Geology of the BO-1 Drillcore: **A)** Simplified lithologic column with 3 major units as determined from detailed core logging; **B)** Observed fault and slip surfaces with intersection angles relative to core axis (assume vertical core) noted in Appendix B; quantity noted on right side of graphic **C)** Alteration zones delineated through meso- to micro-scale observations and whole-rock X-ray diffraction (XRD) mineralogical analyses; **D)** Simplified alteration assemblages as shown in later figures. *Red/Fe-oxide alteration:* Fe-oxide/hydroxide minerals are the dominant alteration minerals in this zone. *Yellow/Intense clays:* Iron oxide alteration continues through this zone; however, the dominant alteration minerals are clays like nacrite and kaolinite plus dolomite. Almost all samples in this interval also show presence of dolomite in thin section and/or XRD. *Blue/Serpentine-chlorite alteration:* The samples in this interval have intense clays, Fe-oxide/hydroxide, dolomite, chlorite and/or serpentine \pm pyrite (identified in hand sample, thin section, or XRD) and exhibit distinct green staining in hand sample. *Grey/Transition Zone:* this interval is marked by a sharp decrease in the concentration of clays, no propylitic alteration, and overlapping intermittent presence of Fe-oxide, dolomite, and Fe-Mg silicate alteration minerals. *Green/Fe-Mg Silicate alteration:* alteration in this interval is generally less intense than near the nonconformity. In this interval, mafic primary minerals are altered to biotite, chlorite, serpentine, or tremolite. Sericitized feldspar often co-occurs or is more dominant in felsic regions.

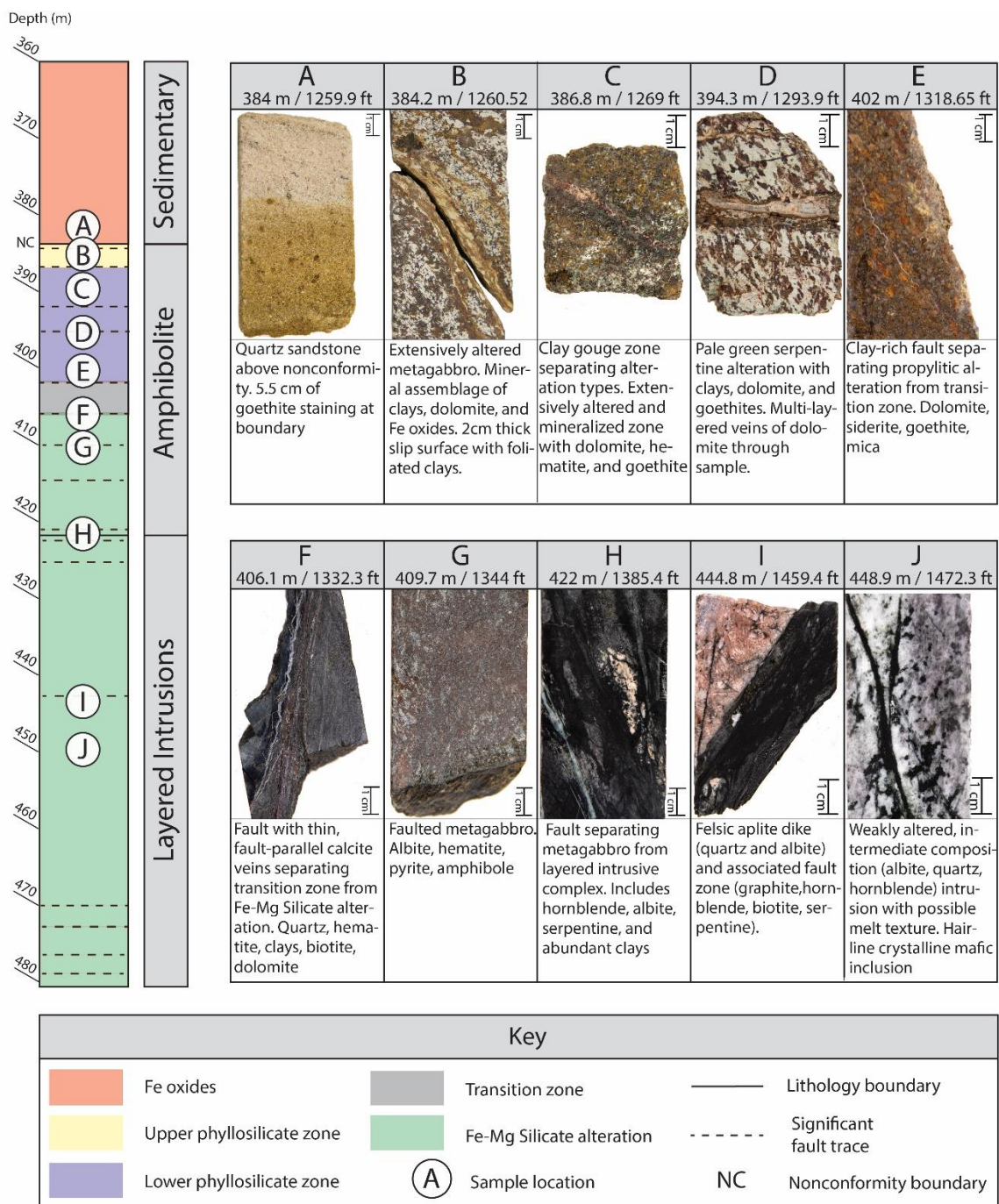


Figure 3: Overview of meso-scale observations of the BO-1 Drillcore. Representative hand sample photos and descriptions of texture and composition of the samples. The lithologic column (left side of figure) shows the simplified alteration assemblages shaded in the background. See Figure 2 for more detailed information on the alteration assemblages.

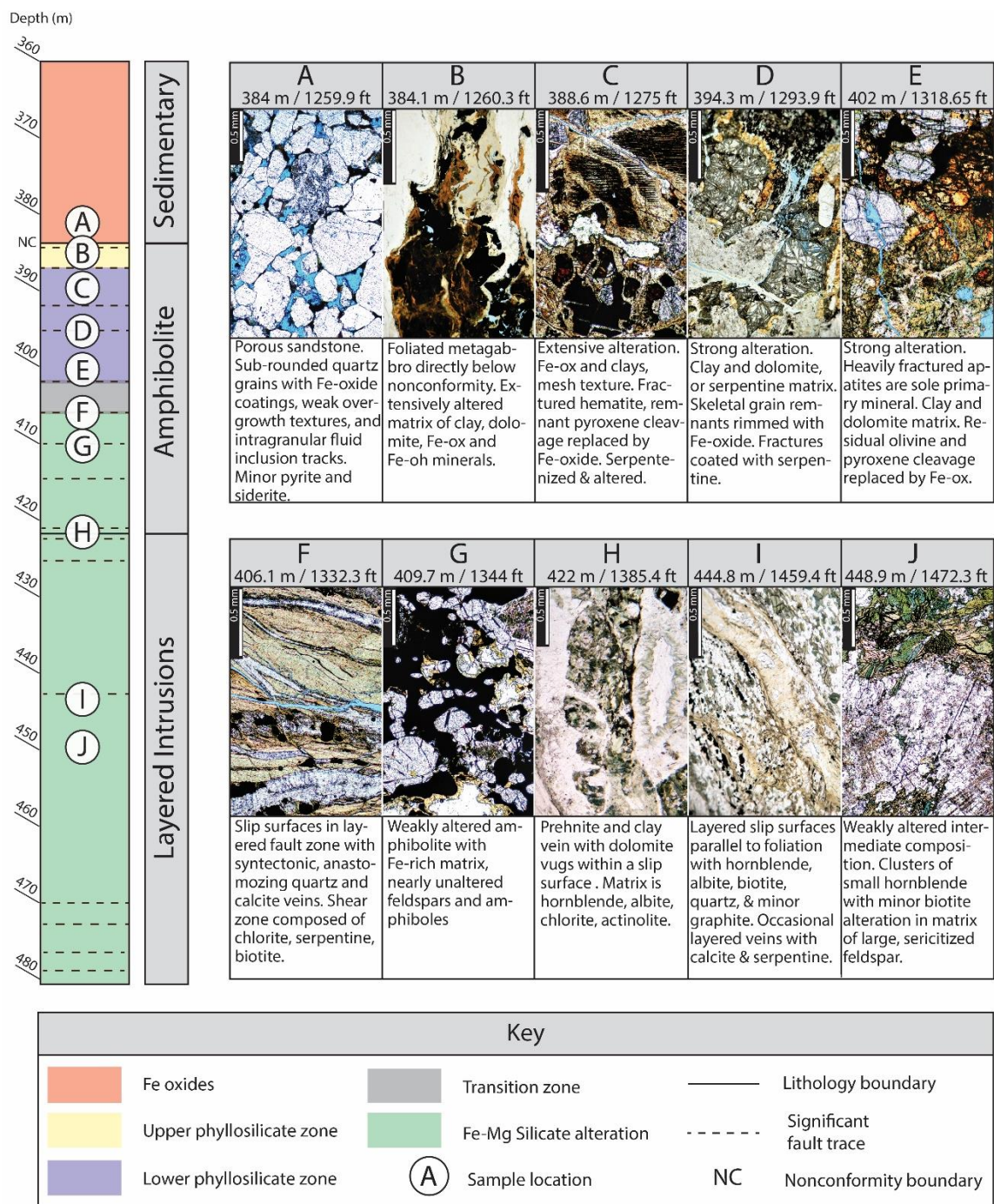


Figure 4: Overview of micro-scale observations of the BO-1 Drillcore. Representative plane-polarized thin section photomicrographs highlighting mineralogical composition, micro-structures, textures and/or fabric of the samples. For a more thorough description of alteration intensity at this scale, refer to Figure 5. Lithologic column (left side) shows sample locations relative to alteration assemblages. See Figure 2 for more detailed information on the alteration assemblages.

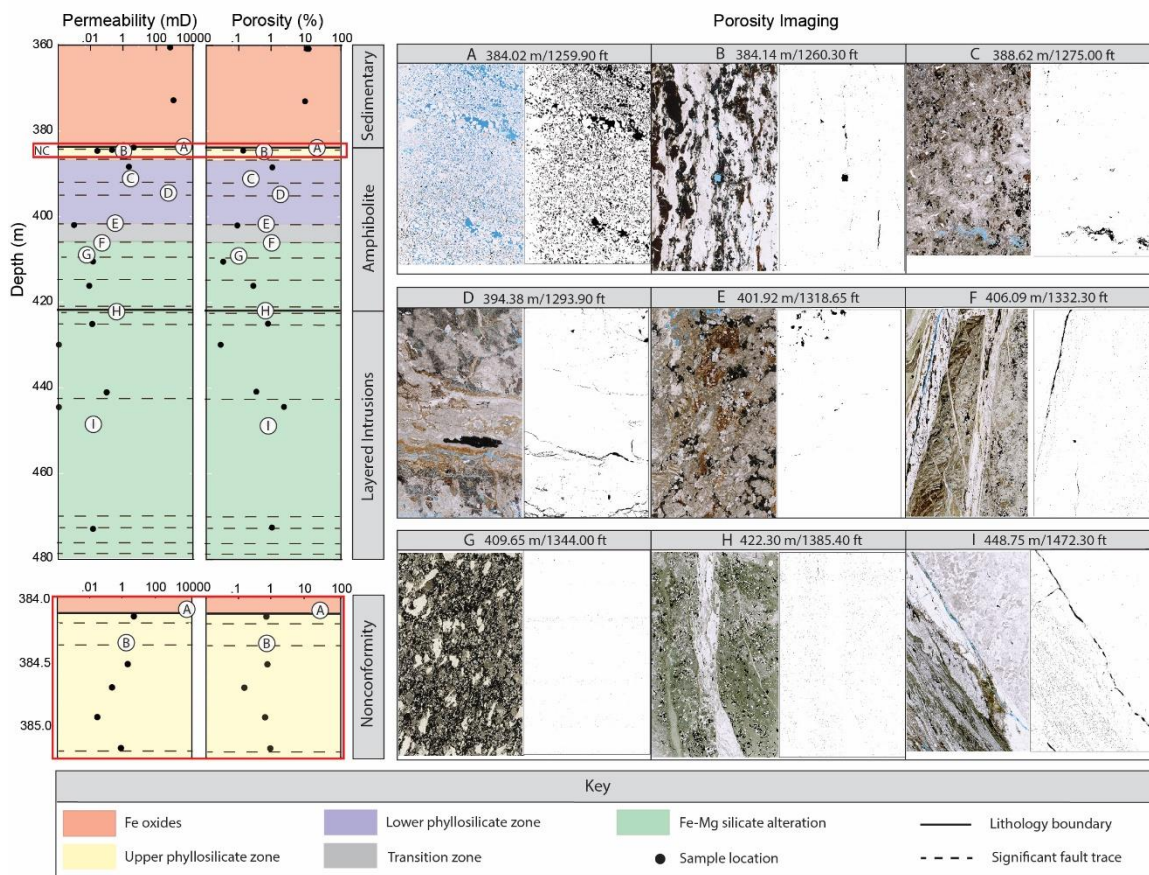


Figure 5: Summary of hydrogeologic rock properties of BO-1 Drillcore. Porosity and permeability of select samples in drillcore BO-1. Lithologic columns (left side) show alteration zones shaded in the background. See Figure 2 for more detailed information on the alteration assemblages and where they overlap. Inset outlined in red shows variation around the nonconformity boundary. Example imagery (Porosity Imaging) shows the full scan of a standard 27 x 46mm thin section (left) and pore spaces isolated by imageJ (right). Samples are injected with blue epoxy to highlight pore spaces.

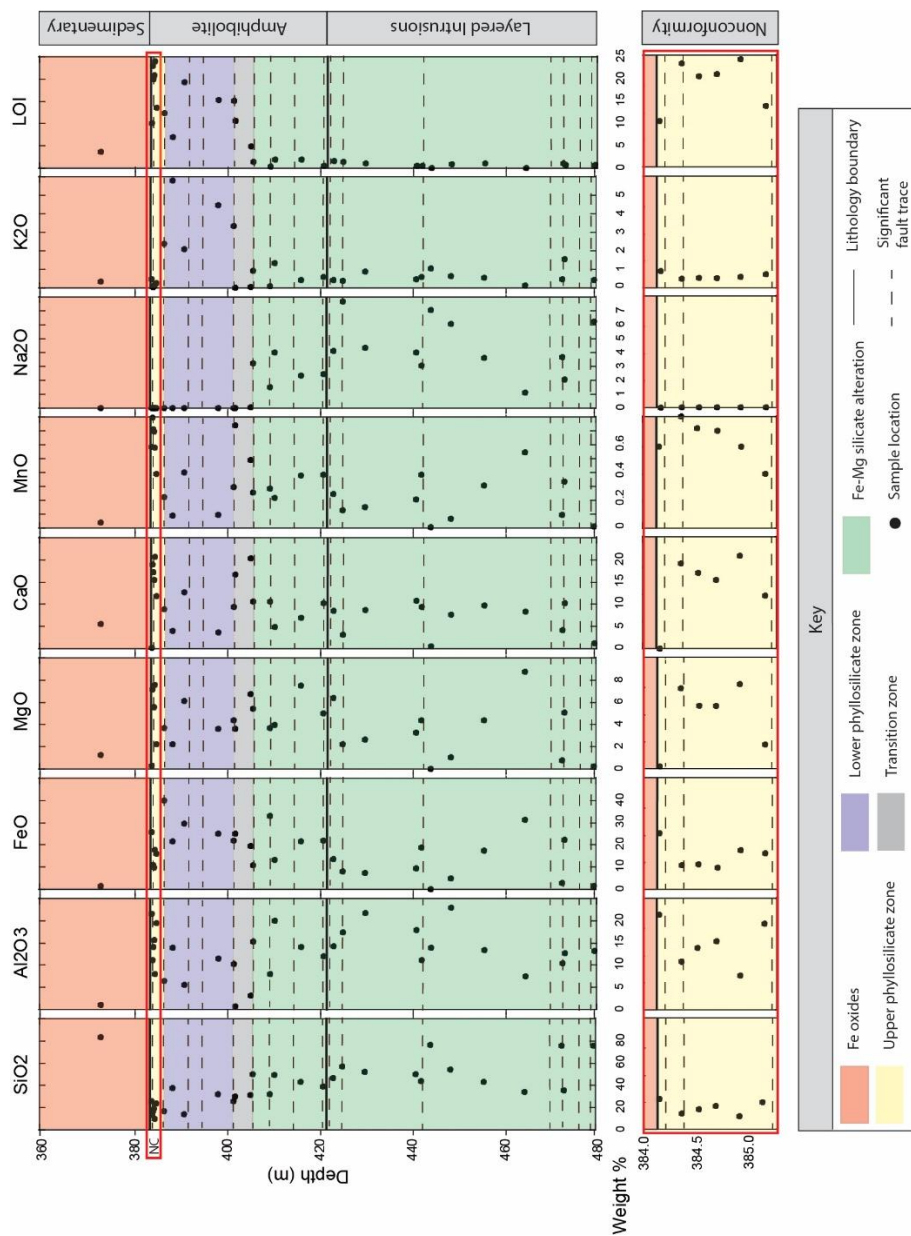


Figure 6: BO-1 Drillcore major-element geochemistry from X-ray Fluorescence analysis. Major oxides and Loss on Ignition (LOI) for 31 whole-rock powder drillcore samples. Percentages are based on unnormalized data. Total Fe content is reported as FeO. Associated alteration assemblages are shown as shaded in the background for comparison Figure 2 for more detailed information. Inset outlined in red shows the high degree of elemental variation within and adjacent to the nonconformity boundary. Note changes in X-axis scale to highlight variation.

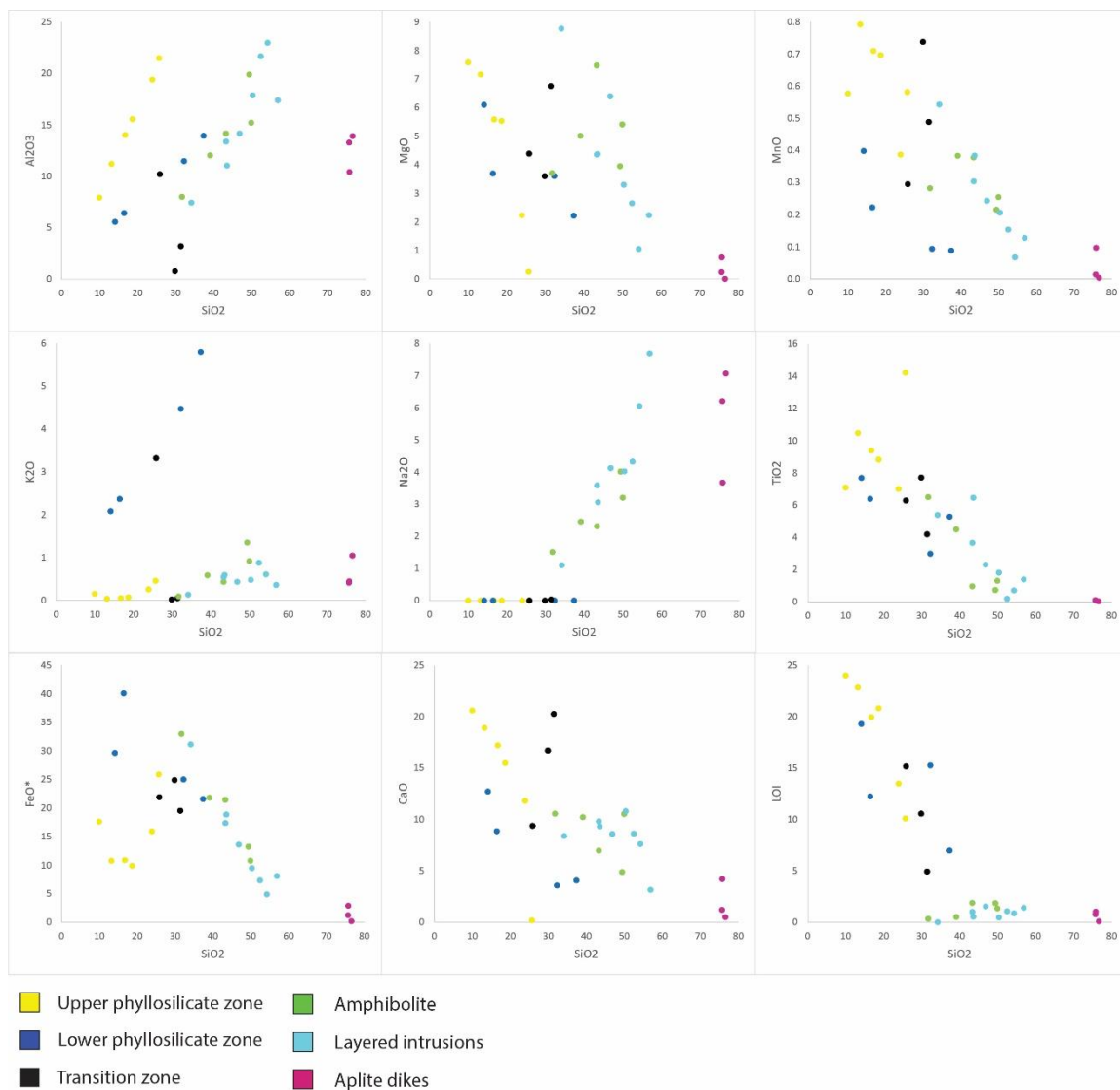


Figure 7: Relative major oxide concentrations of crystalline basement samples in the BO-1 drillcore. Weight percentages are based on unnormalized data. Total Fe content is reported as FeO. Data points are color coded by alteration and/or dominant mineralogy as determined by meso-scale observations, XRD, and petrography.

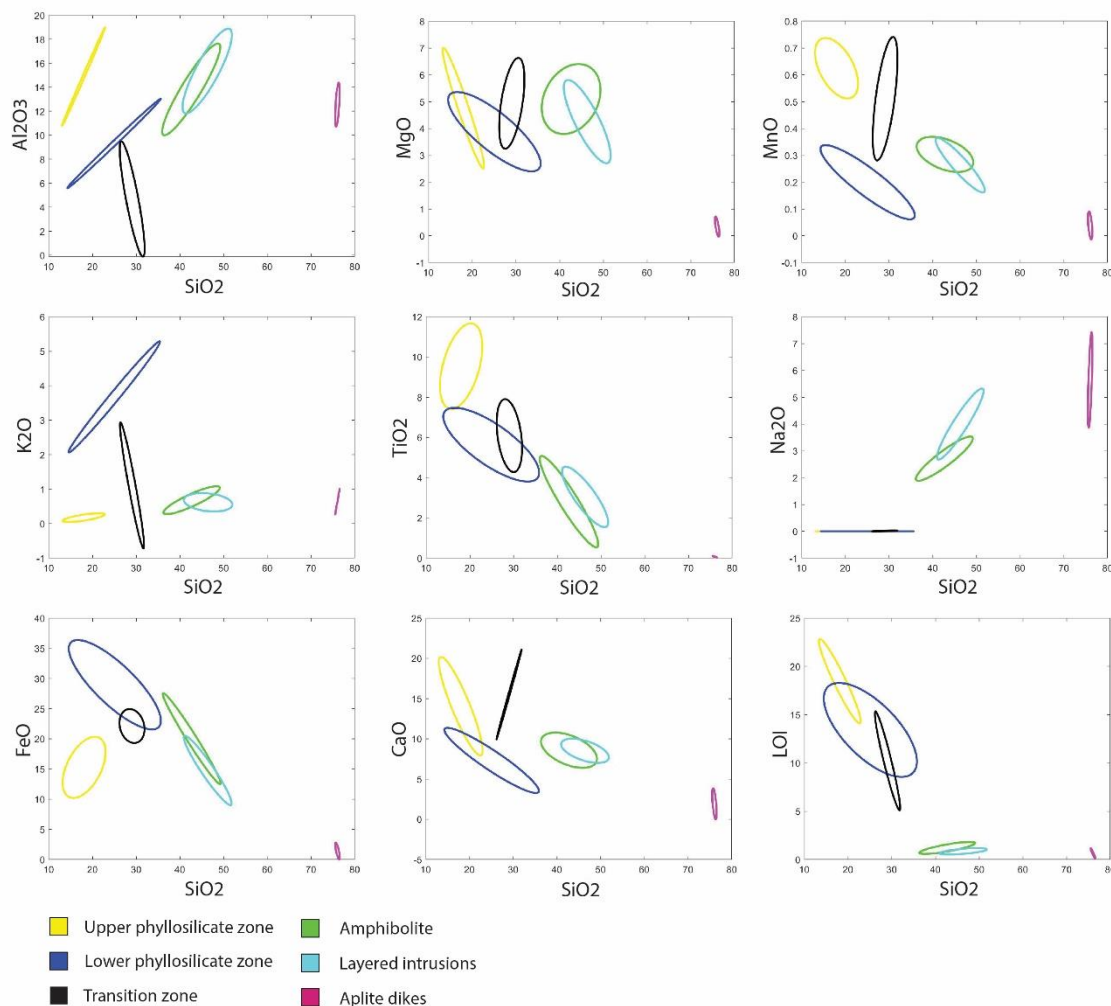


Figure 8: Bootstrapping statistical analysis of relative major oxide concentrations of crystalline basement samples in the BO-1 drillcore. Ellipses represent interval of 90% confidence for where the samples plot. Weight percentages are based on unnormalized data. Total Fe content is reported as FeO. Due to software plotting requirements, note that Na₂O values were assigned a value close to zero (0.001) if no weight percentage was initially detected in XRF. Data points are grouped color coded by alteration and/or dominant mineralogy as determined by meso-scale observations, XRD, and petrography.

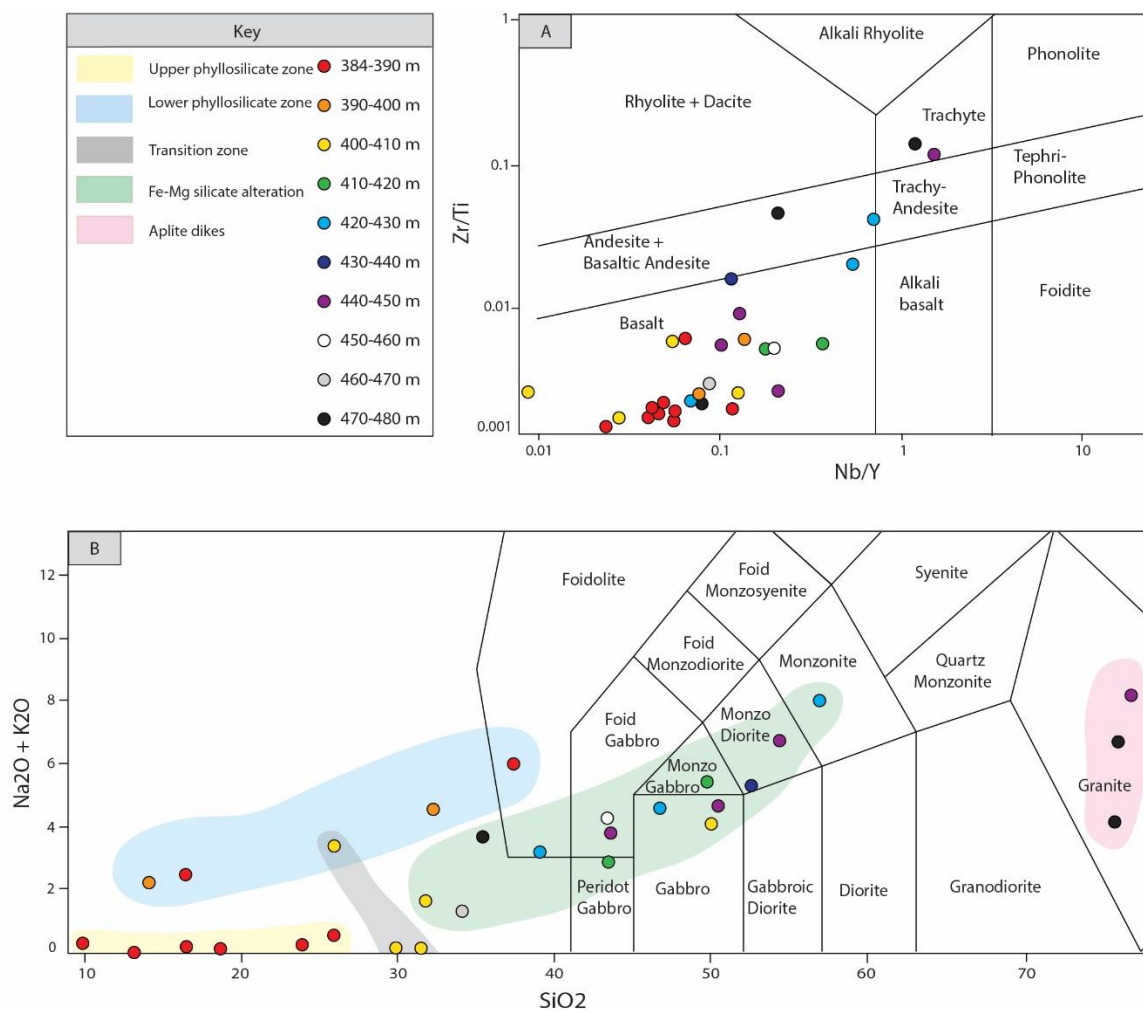
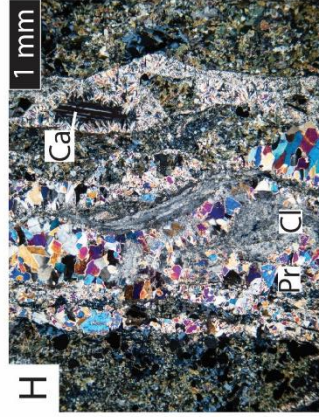
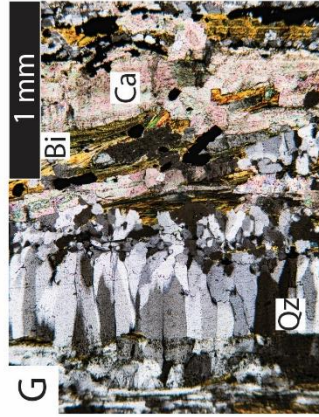
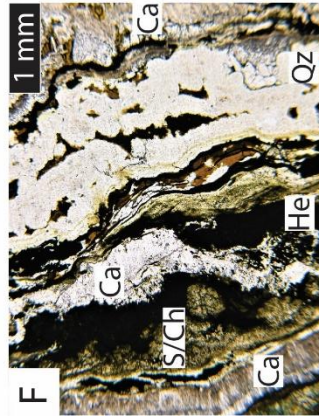
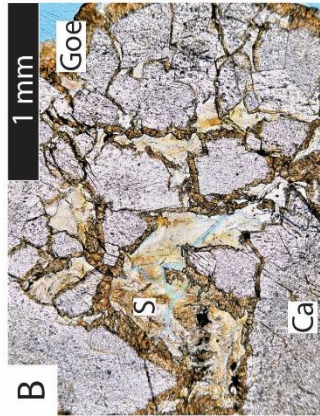
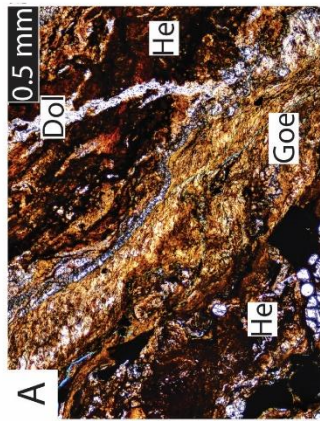


Figure 9: Lithologic composition of Precambrian crystalline basement samples in the BO-1 Drillcore based on major-oxide geochemistry from X-ray fluorescence analysis. A) Basalt discrimination Zr/Ti – Nb/Y plot (Floyd and Winchester, 1978; modified by Pearce, 1996) on a log scale B) Total Alkali Silica (TAS) plot (Middlemost 1994). Shaded clusters indicate dominant mineral assemblage. The Zr/Ti plot uses fluid immobile trace elements to determine igneous protolith even if the sample has been subjected to alteration.

BO-1



B-1

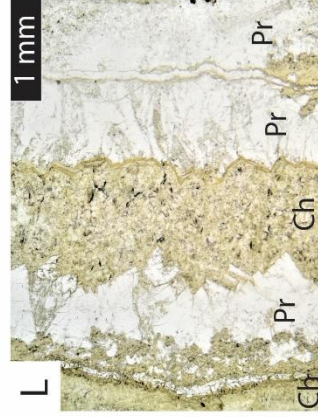
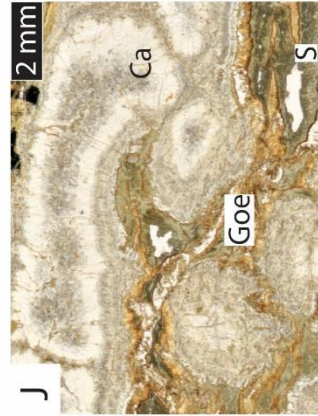
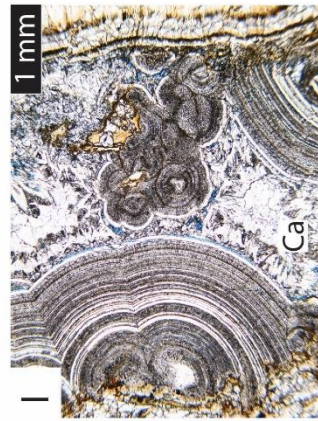


Figure 10: Summary of vein textures in BO-1 and B-1 Drillcores. Caption on next page.

Figure 10: Summary of vein textures in BO-1 and B-1 Drillcores. (following terminology and textural indicators of boiling conditions, established by Dong et al., 1995; Moncada et al., 2012). Blue epoxy is visible within pore spaces. **A)** Sample BO-1_1261.52 in plane-polarized light (PPL). Layered hematite (He-brown/red) and goethite (Goe-orange/yellow) vein cross-cut by dolomite (Dol) in host rock of altered gabbro (not pictured): clay, Fe-oxide/hydroxides, dolomite, Cr-spinel; **B)** Sample BO-1_1283.3 in PPL. Brecciated, rhombic carbonate vein (white) with fibrous siderite surrounding brecciated grains (dark yellow) and infilled with serpentine (light yellow). All non-boiling textures; **C)** Sample BO-1_1293.9 in cross-polarized light (XPL). Layered vein with rhombic carbonate in the center (non-boiling), bordered by goethite stain (Goe-orange) with fibrous silica (Si-grey) on the outermost edge. The outer layers of the vein display crustiform mineralization texture (boiling). Host rock is altered gabbro: dolomitized clay, iron oxide/hydroxides, chlorite, and serpentine; **D)** Sample BO-1_1305.85 in PPL. Fibrous calcite “beef” vein cross-cut by green crustiform-texture green phyllosilicate vein. Green vein is bordered by pale yellow biotite (Bi) altering to serpentine (not pictured). Green vein has been brecciated, offset, and infilled with another generation of fibrous calcite. Host rock is altered gabbro (not pictured): clay, serpentine, Fe-oxide/hydroxides; **E)** sample BO-1_1319.9 in XPL. Quartz vein displaying mosaic or jigsaw textured crystals with interpenetrating grain boundaries (boiling). Stylolites run parallel to the vein wall. Host rock is altered gabbro: clay, hematite, dolomite. Quartz vein is cross-cut by a massive-texture dolomite vein (non-boiling); **F)** sample BO-1_1327.7 in PPL. Crustiform texture quartz and calcite vein (boiling). Inner quartz band displays cockade and massive (microcrystalline) textures (non-boiling); **G)** sample BO-1_1332.3 in XPL. Syntaxial, layered quartz and calcite veins. Calcite is fibrous perpendicular to vein walls **H)** sample BO-1_1385.4 in XPL. Anastomosing prehnite vein in fault zone with fine grain clay. Host rock (green) is hornblende, biotite, chlorite, and apatite. Crystalline vug (upper right corner) is filled with rhombic carbonate (Ca, non-boiling); **I)** Sample B-1_732.6 in PPL) Spherical colloform (boiling) textures in complex, layered calcite vein separating upper sericite-rich altered gabbro from lower serpentine-rich, altered gabbro host rock. Inner vugs are filled with micro-crystalline calcite (Ca, non-boiling). Vein outer walls are crustiform texture (boiling) with fibrous calcite and opaque minerals (not pictured). Locally, outer veins are offset by micro-faults; **J)** Sample B-1_738.0 in PPL. Cockade (non-boiling) texture carbonate (Ca) vein outlined in fibrous orange goethite-stained carbonate (Goe) with green serpentine (S) infilling; **K)** Sample B-1_744.0 in PPL. Layered colloform-crustiform (boiling) calcite vein with filled inner vug. Fibrous calcite vein on the outer vein edge separating serpentine-rich host rock (S); **L)** Sample B-1_1121.4 in PPL. Layered fault cement of rhombic, crystalline prehnite (Pr-white) and fine grained, chlorite core (Ch-green).

Mineral abbreviations: Bi-biotite, Ca-calcite, Cl-clay, Ch-chlorite, Dol-dolomite, Goe-goethite, He-hematite, Pr-prehnite, Qz-quartz, Si-silica, S-serpentine

Table 1: Qualitative XRD analysis for the BO-1 drillcore. Highlighted sample depth boxes indicate a sample with an associated permeability test. Not all samples collected for analysis are reported here. Mineral concentration marked with shaded boxes. Dark blue: major, medium blue: minor, light blue: detected.

Depth (ft)	Quartz	Feldspar	Inosilicates	Phyllosilicates	Other Silicates	Carbonates	Sulfate/Sulfide	Oxide/Hydroxide	Halides / Phosphates	Native Elements
BO-1-1183.67-1184 A (granule layer)	Quartz					Dolomite		Goethite		
BO-1-1183.67-1184 B (coarse to fine)	Quartz	Microcline								
BO-1-1210-1210.1		Microcline, Orthoclase		Kaolin-Serpentine (Dickite)	Zeolite*			Goethite		
BO-1-1224.15-1224.42	Quartz									
BO-1-1258.6-1258.63	Quartz			Kaolin-Serpentine (Nacrite)				Goethite		
BO-1-1259.9-1260.18 A (no stain)	Quartz									
BO-1-1259.9-1260.18 B (stain)	Quartz							Goethite		
BO-1-1260.3-1260.52				Kaolin-serpentine; Chlorite*				Co-Goethite		
BO-1-1260.52-1261.25 A (host rock)			Epidote	Kaolin-serpentine		Dolomite	Anhydrite			
BO-1-1260.52-1261.25 B (slip surface)				Kaolinite, Dickite, Chlorite-vermiculite		Dolomite				
BO-1-1261.52-1261.83				Kaolin-serpentine (Nacrite, Kaolinite)		Dolomite				
BO-1-1262.11-1262.47 A (Host/veins)				Kaolin-serpentine (Nacrite, Kaolinite)		Dolomite				
BO-1-1262.11-1262.47 B (clay center)				Kaolin-serpentine (Nacrite, Kaolinite)		Dolomite				
BO-1-1262.87-1263.13						Dolomite		Hematite, Rutile	Apatite	
BO-1-1263.65-1263.95				Kaolin-serpentine (Dickite)		Dolomite		Hematite	Apatite	
BO-1-1263.95-1264 (rubble)				Aluminosilicate		Dolomite		Hematite, Anatase	Apatite	
BO-1-1268.15-1268.25 (rubble)				Kaolin-serpentine (Nacrite)		Dolomite		Hematite		
BO-1-1269-1269.17						Dolomite		Goethite		
BO-1-1274.2-1274.4				Sepiolite (Palygorskite?)		Dolomite		Hematite, Goethite, Rutile		
BO-1-1275-1275.35 host & slip				Mica				Magnetite, Hematite, Goethite, Anatase		Graphite
BO-1-1277.9-1278	silica			Chlorite/Montmorillonite?				Hematite, Goethite, Anatase	Apatite	
BO-1-1283.3-1283.7 A (slip/shear)						Dolomite, Siderite		Goethite	Apatite	
BO-1-1283.3-1283.7 B (host)						Dolomite		Anatase, Goethite	Apatite	
BO-1-1286.8-1287.12 A slip surface						Dolomite, Siderite				
BO-1-1286.8-1287.12 B host				Chlorite-Vermiculite		Dolomite		Hematite		

BO-1-1286.8-1287.12 C fracture				Mica*		Siderite		Hematite, Chromite		
BO-1-1287.8-1287.85			Amphibole (tremolite)*	Mica				Ni-Hematite; Cu,Cr Spinel		
BO-1-1293.9-1294.3_A host				Mica		Fe-Mg Carbonates (Dolomite,				
BO-1-1305.85-1305.92_B				Mica*		Siderite, Dolomite				
BO-1-1307.25-1307.5 A host				Mica (Illite)						
BO-1-1307.25-1307.5 B fracture/slip surface	silica			Mica		Siderite, Dolomite				
BO-1-1318.65-1319.35_A (host)						Zeolite*	Dolomite, Siderite		Apatite, Fluorite*	
BO-1-1318.65-1319.35_B (fracture)	Quartz	Orthoclase		Mica (Paragonite?)	Zeolite (Phillipsite?)	Fe-Mg Carbonate (Siderite)				
BO-1-1319.35-1319.45				Chlorite (Clinocllore)		Siderite				
BO-1-1319.9-1320.25 A host	Quartz			Mica (Phlogopite?)		Dolomite			Apatite	Graphite
BO-1-1319.9-1320.25 B vein	Quartz									Graphite
BO-1-1327.7-1327.9	Quartz		Hornblende					Hematite	Apatite	
BO-1-1330.4-1330.6_A (host)	Quartz							Magnetite		
BO-1-1332-1332.3 A host		Albite	Diopside, Glaucophane	Chlorite (Clinocllore)				Ni-Magnetite		
BO-1-1332-1332.3 B black slip surface	Quartz	Albite	Tremolite, Diopside	Chlorite (Clinocllore)						
BO-1-1332.3-1332.5	Quartz			Chlorite		Dolomite		Spinel (Bixbyite)		Graphite
BO-1-1344-1344.4	Quartz	Albite*	Amphibole (Arfvedsonite ?)			Cordierite		Hematite, Ilmenite	Apatite	Graphite
BO-1-1347.6-1348 A host & slip		Albite	Riebeckite, Fe Glaucophane *	Chlorite- Serpentine						
BO-1-1347.6-1348 B pink alteration		Albite		Muscovite	Zeolite			Fe-oxide		
BO-1-1348.6-1348.8		Anorthite, Andesine	Amphibole (Tremolite)		Zeolite (Phillipsite?)			Ti-Hematite		
BO-1-1366.2-1366.6		Albite, Anorthite	Mg- Hornblende		Zeolite					
BO-1-1372.9-1373.2		Albite	Hornblende	Serpentine (Greenalite?)						
BO-1-1381.7-1382		Albite	Hornblende							
BO-1-1385.4-1386 A Host		Albite	Mg-Fe Hornblende	Chlorite- Serpentine						
BO-1-1385.4-1386 B Slip			Amphibole (Fe- Glaucophane)	Chlorite- Serpentine, K-Al silicate (clay)	Zeolite			Chromite		
BO-1-1389.1-1389.6		Albite	Tremolite					Spinel		
BO-1-1395.4-1396 A host		Albite								
BO-1-1395.4-1396 B slip		Albite	Fe-Tremolite	Chlorite- Serpentine						
BO-1-1411.6-1412		Albite, Anorthite	Fe-Tremolite							
BO-1-1430.2-1430.7		Albite	Hornblende						Apatite	
BO-1-1447.7-1448.25		Albite, Anorthite			Cordierite			Ilmenite		

BO-1-1451.5-1451.9_A host	Quartz	Albite	Hornblende	Sepiolite	Aluminosilicate					
BO-1-1458-1458.8	Quartz	Albite	Amphibole (Grunerite?)							
BO-1-1459.4-1459.6 (slip)		Albite	Amphibole (Riebeckite?)							Graphite
BO-1-1467-1467.5		Albite	Hornblende, Glaucophane		Zeolite (Phillipsite?)					
BO-1-1472.3-1473		Albite								
BO-1-1495.6-1496.4		Albite	Hornblende		Sodalite	Dolomite				
BO-1-1505.7-1506.1			Hornblende		Zeolite (Phillipsite?)		Covellite	Hematite, Ilmenite	Nitratine	
BO-1-1514.3-1515		Albite	Mg-Hornblende							
BO-1-1524.6-1524.9		Microcline	Anthophyllite, Hornblende, Diopside							
BO-1-1550.72-1551.15 A host	Quartz	Albite	Hornblende			Magnesite		Hematite		
BO-1-1550.72-1551.15 B slip surface?		Albite	Hornblende	Phlogopite				Perovskite	Fluorapatite	
BO-1-1552.3-1552.65		Albite	Hornblende	Biotite			Bornite			Graphite
BO-1-1552.65-1553A host	Quartz	Albite	Mg-Fe Hornblende							
BO-1-1552.65-1553B slip		Albite	Mg-Fe Hornblende							
BO-1-1566.2-1566.6		Albite	Hornblende				Hauerite, Picromerite			Graphite
BO-1-1573-1573.5	Quartz	Albite			Willemite					
BO-1-1575 (rubble)			Hornblende, Rhodonite							

4.1 Above Nonconformity Interface

4.1.1 Mesoscopic Observations

The sedimentary interval in BO-1 drillcore (212.33-1260.18 ft / 64.72-384.10 m depth) consists of Ordovician dolostones above Upper Cambrian sandstones at the lowest part of this interval (Mossler, 1995; MNDNR, 2021). Only sedimentary units proximal to the nonconformity interface (1183.67 ft / 360.78 m and below) were analyzed. The upper Cambrian rocks discussed here are the basal Mount Simon Sandstone (Figure 2) which is capped by the shales and siltstones of the Cambrian Eau Claire Formation (Mossler, 1995; MNDNR 2021).

The Mount Simon Sandstone sampled in this drillcore is a quartz arenite sandstone with minor feldspar and lithic fragments (Figure 11). There are occasional clay, silt, or gravel layers in the sandstone. Structures in this section are typically open mode fractures parallel to bedding (approximately perpendicular to core axis), though it is ambiguous if these fractures were a result of the drilling process. No faults were observed in the sampled sedimentary bedrock interval. Many samples in this interval display Fe-oxide minerals, determined by red staining, or Fe-hydroxide mineralization, determined by yellow stains in hand sample (Figure 3A, Figure 11). Directly above the Precambrian interface, there is a ~5 cm zone of yellow goethite staining (Figure 3A, Figure 11). In heavily stained regions, some grains display a darker, pitted texture.

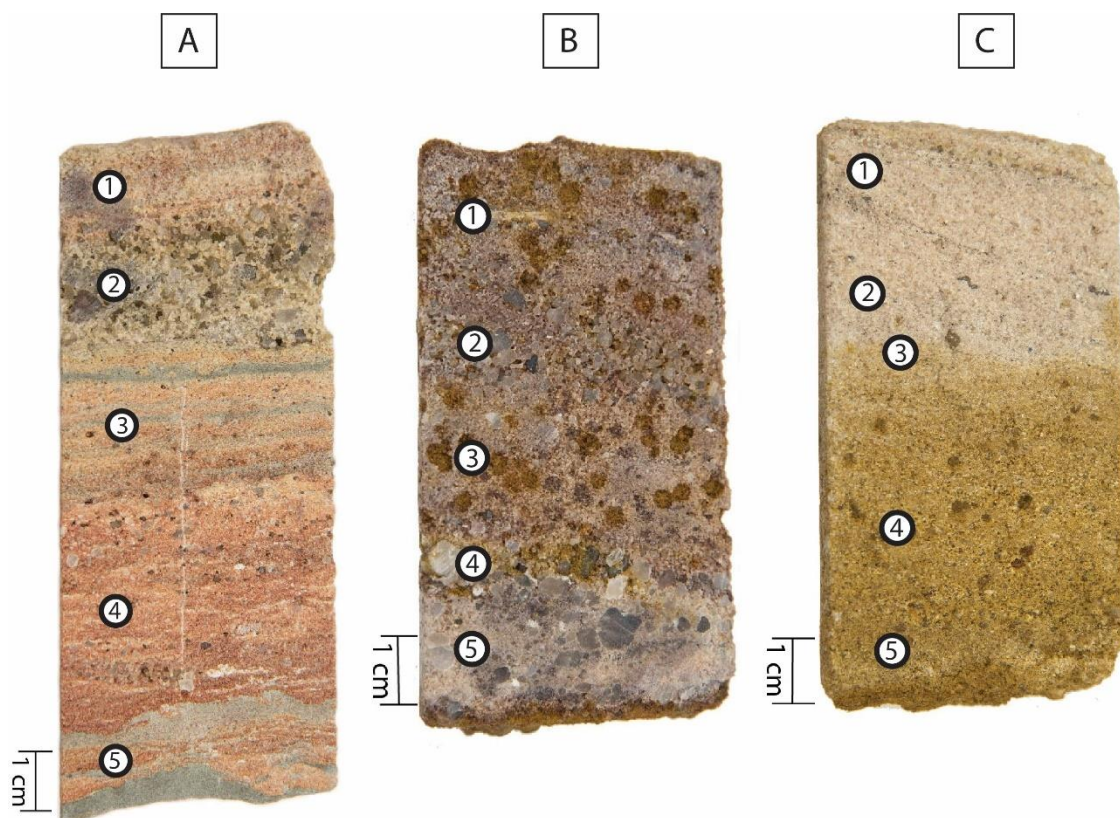


Figure 11: Sedimentary samples from the BO-1 drillcore. Only samples selected for permeability testing are shown; numbers indicate permeability test site locations. **A)** Sample 1183.67-1184.00. Poorly sorted quartz arenite with granule to clay grains, featuring red hematite staining. Granule layer (upper part of sample) fizzes slightly in HCl and is poorly cemented. Clay layers (grey) to medium grains are better cemented with no reaction to HCl. **B)** Sample 1224.15-1224.42: Poorly sorted coarse grain sandstone with red hematite staining and rust-colored goethite staining. Goethite stains are localized to leached pits. Sample reacts with HCl, particularly in fine grained areas, with the exception of the well-cemented lower 1.7cm of the sample. **C)** 1259.90-1260.18. Pink quartz sandstone, medium sorting, with fining upward sequences. Occasional fine, pyrite grains in the upper half of the sample. Heavily stained with goethite at the lower 5.5cm of the sample, which is in direct contact with the nonconformity. Leached pits observed within the stained section and just above, which appear as darker brown circles in the image.

4.1.2 Petrographic Analysis

In the 4 thin sections of the quartz arenite, samples are dominantly poorly sorted, subrounded to angular quartz grains with clay minerals, and minor micas and sulfates (Figure 4a & 12). Grains are cemented with quartz, Fe-oxide/hydroxide minerals, and carbonate (Figure 12). Bedding is defined by grain size and/or mica horizons (Figure 12A). Small, brown siderite crystals line pore space perimeters in some samples in an irregular and discontinuous manner (Figure 12B). Other samples have opaque coatings around grains, either composed of hematite and/or goethite (Figure 4A, Figure 12). Areas with visible staining in hand sample contain a greater concentration of opaque minerals between grain boundaries (Figure 12).

4.1.3 Hydrogeologic Properties

Porosity and permeability measurements made in the drillcore are highest in the sedimentary section, ranging from 9.1 ± 1.1 to 11.7 ± 1.4 % and 635 ± 623 to >3000 mD, respectively, across the 3 targeted samples (Figure 5, Appendices A & B). In general, the pore channels are between grains and pore shape and volume vary within samples. Regions with leached/pitted minerals have larger pore spaces and yield high permeability, with less porosity between sediment laminations or variations in grain size. Areas of oxide and/or hydroxide staining yield reduced porosity values as seen in Figure 6A, which has slightly fewer, smaller, and less 2-dimensional connected pore spaces in the lower half of the sample stained with goethite.

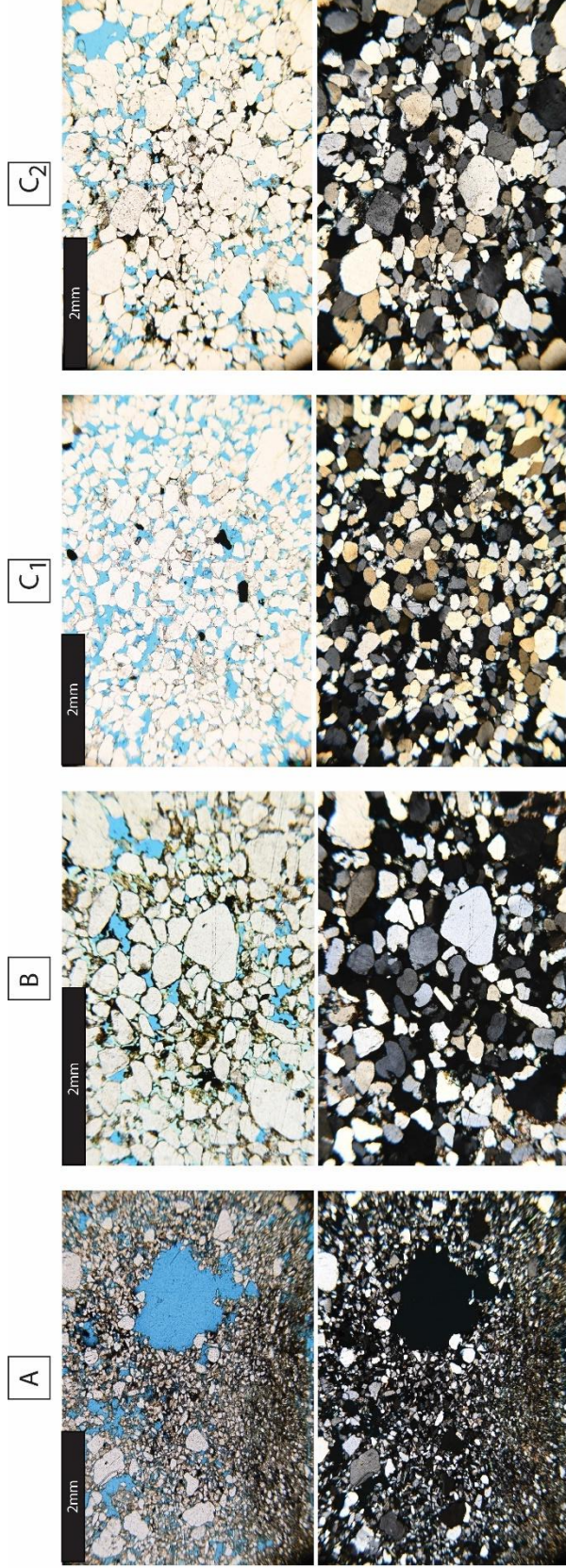


Figure 12: Sedimentary Photomicrographs from the BO-1 drillcore. Plane polarized light (PPL) images on the top row, cross polarized light (XPL) images on the bottom. **A)** Sample 1183.67-1184.00. Poorly sorted quartz arenite with granule to clay grains. Sample shows Fe-oxide cements (black in PPL), clay cement (grey in PPL), and carbonate cement (high order colors in XPL, lower part of the sample). Large pore spaces are leached grains. **B)** Sample 1224.15-1224.42: Hematite and goethite cement (black and yellow in PPL) with siderite in pore spaces (small, brown, high relief in PPL). Carbonate cement in the area surrounding the goethite cement in the corners of the image (high interference colors in XPL). **C1)** Sample 1259.90-1260.18. Upper, non-stained part of the sample showing subangular to rounded grains. Opaque grains in PPL are pyrite. Clay (grey-brown) and quartz cement. **C2)** Sample 1259.90-1260.18. Lower part of the sample, which has hematite (black) and goethite (yellow) cement. Many fractured grains, grain boundaries are compacted.

4.1.4 Whole-rock Mineralogy and Geochemical Composition

Seven XRD samples were analyzed across this lithologic unit (Table 1). All samples have a major presence of quartz. The minor amounts of pyrite, oxides, clays, and carbonates observed in thin section were not detected by XRD, except for minor microcline in one sample and minor goethite in the sample directly above the nonconformity. Based on XRF analysis, this unit contains high amounts of SiO₂ (83%) and minor amounts of all other major oxides (0 - 6%), the highest of which is CaO and likely corresponds to carbonate cements observed (Figure 6). Measured FeO concentrations are low, however, the particular sample selected for analysis (1224.15 ft / 373.12 m) was well-cemented with lesser staining near the base and also did not yield an iron-oxide or hydroxide minerals in XRD analysis.

4.2 Nonconformity Interface: Upper Phyllosilicate Zone

4.2.1 Mesoscopic Observations

The samples directly below the nonconformity have a high presence of clays, oxides, and dolomite which extends from 384.14 - 386.79 m (1260.30 – 1269.00 ft; Figures 2, 3, & 12). Mineral textures are difficult to recognize at the meso-scale (Figure 13). Rock foliation is inconsistent and defined by uneven layers of light-grey clay alternating with darker yellow-brown (Fe-hydroxide). The darker layers slightly effervesce when exposed to HCl, except for the sample closest to the nonconformity. There are also small, subhedral dark metallic flecks visible at the meso scale.

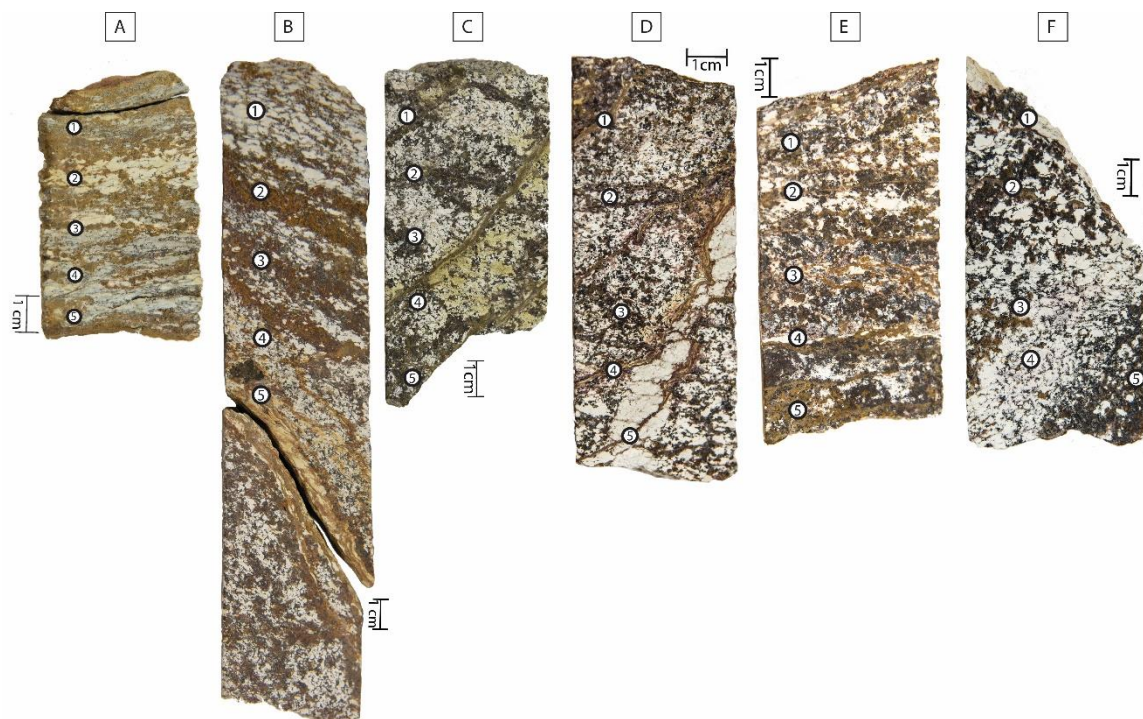


Figure 13: Nonconformity upper phyllosilicate zone samples from the BO-1 drillcore. Only samples selected for permeability testing are shown; numbers indicate permeability test site locations. **A)** Sample 1260.30-1260.52 ft. This sample is directly in contact with the nonconformity boundary. Visible fracture is a faulted surface with slickenlines dipping $\sim 8^\circ$. Rust layers are goethite, white layers are clay. Small, metallic grey flecks are visible throughout the sample. Does not react with HCl. **B)** Sample 1260.52-1261.25 ft. Similar mineralogy to previous sample. Brown Fe-oxide areas react with HCl (dolomite present in XRD). Fractured portion of the sample is a fault that dips $\sim 55^\circ$. The slip surface is 4-6mm thick with slickenlines. **C)** Sample 1261.52-1261.83 ft. Stockwork texture hematite-goethite veins and slip surfaces (some veins are offset by others). **D)** Sample 1262.11-1262.47 ft. Similar host rock composition to previous samples. Additional hematite-goethite veins, plus 4-16mm kaolinite vein dipping $\sim 60^\circ$. **E)** Sample 1262.87-1263.13 ft. Similar composition to previous samples with higher concentration of oxides. Many parallel, approximately horizontal sub-mm goethite-hematite veins. **F)** Sample 1263.65-1263.95. Slip surface dipping at $\sim 45^\circ$ with slickenlines on the surface. Host rock appears darker with less goethite.

The first fault trace intersecting the Precambrian section of the drillcore is within 1 cm of the nonconformity. The fault is sub-mm thick and trends nearly parallel to the fabric of the host rock, dipping $\sim 8^\circ$ (Figure 13A). There are a total of 5 slip surfaces within a 2 m interval below the nonconformity, which appear as single plane, open mode, clay-rich slip surfaces with slickenlines (Figures 3B & 13). Many samples in this phyllosilicate zone are intensely fractured and display stockwork texture (Figures 13C & D). Fractures are lined with multiple generations of goethite (yellow) and hematite (red) (Figures 10A, 13 C & D). The fractures and faults occur at varying dip angles and can have clay infilling up to 1.5 cm thick (Figure 13D). Given the spatial limitation of the drillcore, we do not have confirmation if these faults continue into the sedimentary cover or terminate at the nonconformity. The contact itself appears depositional.

4.2.2 *Petrographic Analysis*

The 6 thin sections in this upper phyllosilicate zone are primarily composed of dolomite, clays, Fe-bearing minerals, and apatite (Figures 4B & 14). The matrix is fine-grained white clay (Kaolin-group in XRD; Table 1). The brown layers are composed of fine-crystalline iron-oxide minerals, which are anhedral with diffuse grain boundaries and display multiple stages of oxidation as irregular laminations of varying browns/oranges within grains (combinations of hematite and goethite, Figure 14). Euhedral, opaque grains are magnetite or uncommonly pyrite, which often appear euhedral and brecciated.

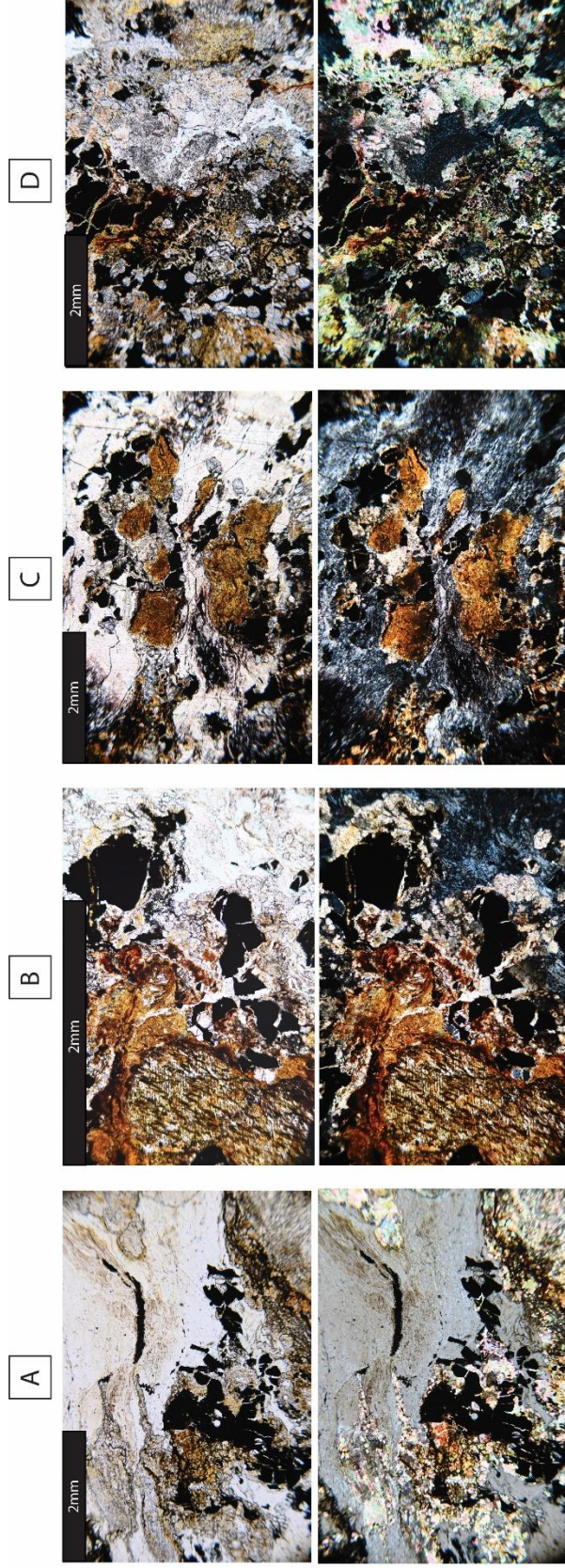


Figure 14: Nonconformity upper phyllosilicate zone photomicrographs from the BO-1 drillcore. Plane polarized light (PPL) images on the top row, cross polarized light (XPL) images on the bottom. **A)** Sample 1260.52-1261.25 ft. Offset in clay gouge zone parallel to slip surface. Opaque, brecciated magnetite & pyrite, goethite, and crystalline dolomite. **B)** Sample 1261.52-1261.83 ft. Fe-oxide minerals are preserving amphibole cleavage in the crystal on the left of the image. **C)** Sample 1262.11-1262.47 ft. Clay, magnetite, hematite, goethite-stained dolomite. **D)** Sample 1263.65-1263.95 ft. Clay, dolomite, magnetite, hematite, goethite, and apatite.

Clay (white in PPL, dark grey in XPL), magnetite (opaque), hematite (red), goethite (orange), dolomite (pastel high order colors in XPL), apatite (colorless, round, gritty, high relief in PPL)

After ~1m beyond the nonconformity, the Fe oxide-/hydroxide grains are darker/more concentrated and align with the cleavage of pyroxenes or amphiboles which are no longer present (Figure 14B). In cross-polarized light, the samples show dolomite in association with Fe-oxide minerals, and dolomite grains appear larger and more euhedral towards local fault slip surfaces (Figure 14A). Most samples, except that nearest the nonconformity, have rounded and fractured apatite.

4.2.3 Hydrogeologic Properties

Permeability and porosity are variable at the meso- to micro-scale across the nonconformity contact ($<1 - 4 \pm 1$ mD; $0.1 \pm 0.0 - 0.7 \pm 0.1\%$) and are greatest in samples that include discrete structures such as faults, fractures, veins, or the nonconformity contact (Figure 5). Pore spaces are observed in brecciated minerals, leached grains, or fine hairline fractures parallel to foliation (Figure 5B).

4.2.4 Whole-rock Mineralogy and Geochemical Composition

Ten samples were analyzed for XRD, which showed the samples are composed of clays (predominantly Kaolin-group kaolinite and/or nacrite) and dolomite with minor apatite (Table 1). All measured samples contain dolomite except for the sample directly at the nonconformity contact. Opaque minerals and Fe-oxides observed in thin section were not always detected by XRD analysis. The lower part of this section (384.92 m / 1262.87 ft onward) demonstrated significant quantities of hematite, which likely corresponds to the diminishing clays seen in thin section.

The 6 XRF samples in the upper phyllosilicate zone showed the lowest concentration of SiO_2 (10 – 26%), Na_2O (0%), K_2O (<1%) in the drillcore (Figures 6-8;

Appendix C). The other major oxides and the LOI are highly variable within this interval. The greatest percent values of LOI (10 - 24%), CaO (<1 - 21%), and MgO (<1 - 8%) are found in this zone. The high LOI likely corresponds to the volume of clays observed in hand sample and thin section. All sampled MnO concentrations are below 1% throughout the core. Using fluid-immobile trace element ratios Zr/Ti and Nb/Y, this interval classifies as a basalt, suggesting a mafic protolith (Figure 9A). Since these samples have extensive secondary mineralization and low concentrations of SiO₂, Na₂O, and K₂O, they do not plot within the standard total alkali silica (TAS) diagram litho-types (Figure 9B).

4.3 Nonconformity Interface: Lower Phyllosilicate Zone

4.3.1 Mesoscopic Observations

This zone extends from 386.79 - 401.92 m (1269.00 - 1318.65 ft) and is separated from the upper phyllosilicate zone by a ~1 m layered clay gouge fault (Figure 3C). Meso-scale textures are similar to the overlying phyllosilicate zone, with alternating dark brown layers and clays (Figure 3D; Figure 15). The clays are stained green with varying intensity, likely from chlorite and serpentine minerals (see 4.3.2) and the brown layers do not appear as sheared or mechanically deformed (Figure 15). The green staining is restricted along a web of fine fractures (Figure 15B) or pervades entire sample (Figure 15D). The yellow-orange goethite/limonite staining of the host rock as seen in the above phyllosilicate zone decreases in favor of intensified red-brown hematite in this zone. Fractures and veins display an outer layer of goethite-stained dolomite (Figure 10B & 10C). Most samples effervesce when exposed to HCl, especially around veins.

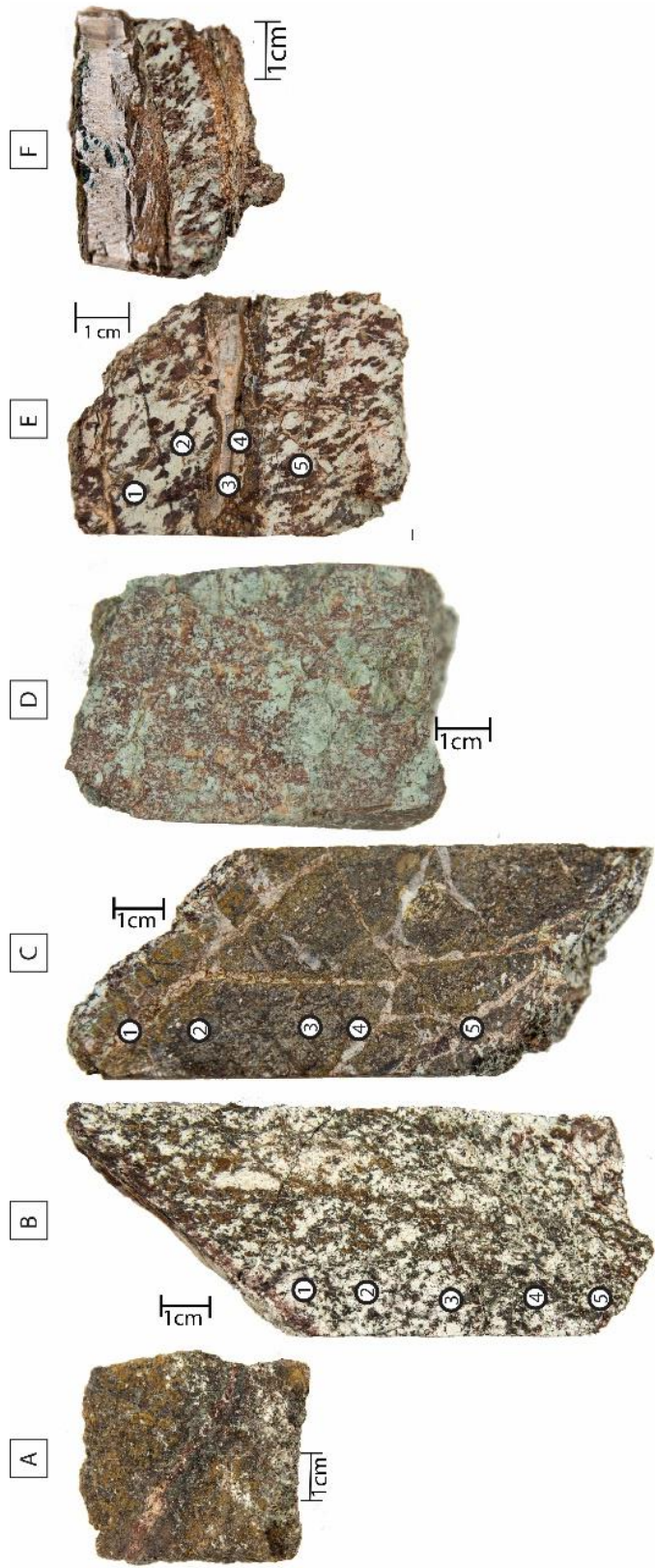


Figure 15: Nonconformity lower phyllosilicate zone samples from the BO-1 drillcore. Numbers indicate permeability test site locations. **A)** Sample 1269.00-1269.17 ft. Poorly consolidated clay gouge zone. Reacts with HCl. **B)** Sample 1275.00-1275.35 ft. Faulted sample dipping ~45°. White clays, red hematite, minor yellow goethite and green staining **C)** Sample 1283.30-1283.7 ft. Stockwork texture dolomite veins in Fe-oxide rich sample. Reacts with HCl throughout the sample, but particularly at veins. **D)** Sample 1286.8-1287.12 ft. Slip surface dipping at ~60°. Host rock is composed of serpentine (green), hematite (red), and dolomite (fizzes in HCl). **E)** Sample 1293.9-1294.3 ft. Red-brown hematite, green chlorite-clay, and yellow goethite. Vein is dolomite bordered by fibrous goethite-stained dolomite. **F)** Sample 1305.85-1305.95 ft. Host rock is serpentine-rich clay and hematite-rich red-brown layers. Vein is fibrous calcite cross-cut by a dark green phyllosilicate vein.

Notable structural features include the gouge zone at the upper part of this zone (Figure 3C, Figure 15A), stockwork texture veins (Figure 15C), slip surfaces (Figure 15 B & D), and cm-thick layered veins which have been brecciated and healed (Figure 10B – D, 15C,E&F). Slip surfaces are linear to irregular with occasional patches of waxy slickenfibers, at ~1 mm thickness and dipping at varying angles relative to the core axis. This zone is faulted at a frequency of ~2.3/m.

4.3.2 *Petrographic analysis*

Similar to the upper phyllosilicate zone, all 5 thin sections in this zone feature anhedral material with diffuse grain boundaries. (Table 1; Figure 5; Appendix A1). The matrix is typically composed of white to grey clays with dolomite and mesh-textured serpentine and chlorite (Figure 16). The outlines of some primary mafic minerals have been preserved in some areas, but have since been replaced by hematite, goethite, or serpentine (Figure 4C, 4D, Figure 16A). Mineral cleavage planes are visible and are indicated by darker staining of iron-oxides where preserved. Iron-bearing minerals in the lower phyllosilicate zone are more concentrated than the clay-dolomite zone above. They are often opaque and outlined with hematite or goethite. The only euhedral minerals in this zone are brecciated magnetite and apatite, though often they appear highly damaged or only their outlines remain in samples with slip surfaces (Figure 16).

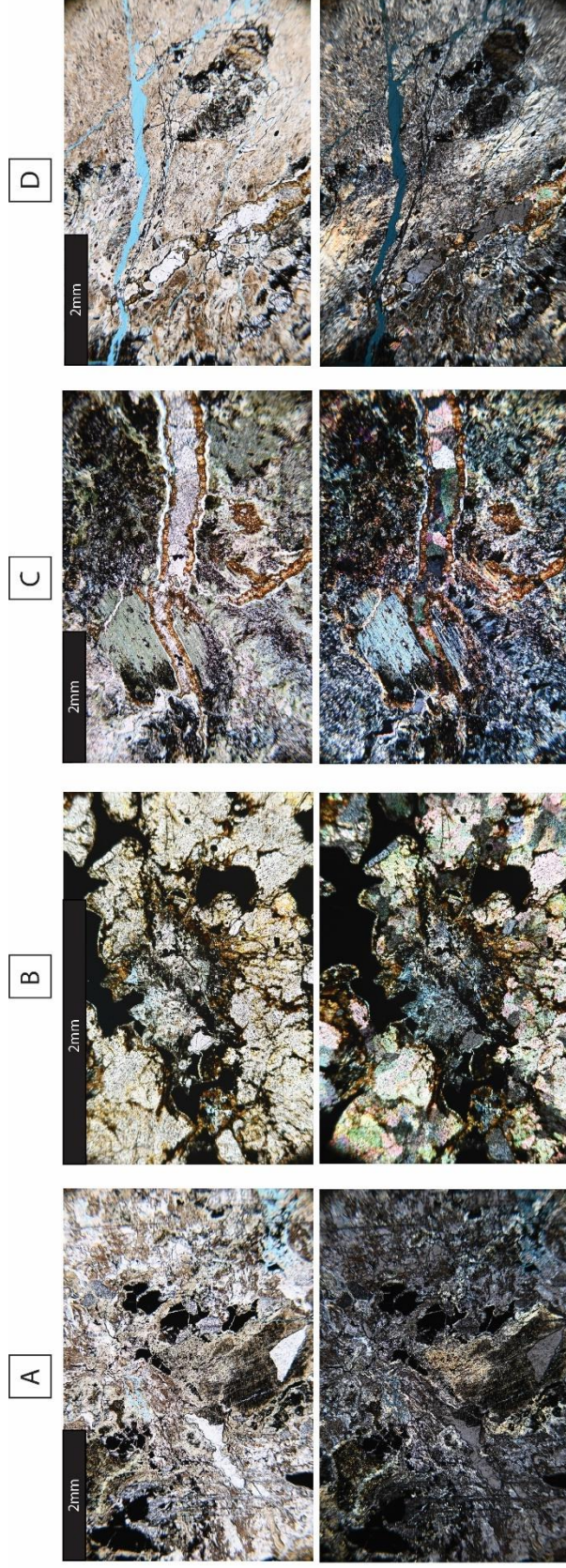


Figure 16: Nonconformity lower phyllosilicate zone photomicrographs from the BO-1 drillcore. Plane polarized light (PPL) images on the top row, cross polarized light (XPL) images on the bottom. Pore spaces are stained blue in PPL. **A**) Sample 1275.00-1275.35 ft. Serpentine (bottom left through upper middle) through clays, hematite, micas (surrounding hematite) Primary mineral cleavage textures preserved in hematite. Opaques are graphite or magnetite. **B**) Sample 1283.30-1283.70 ft. chlorite in the center surrounded by a ring of yellow goethite, followed by dolomite. Opaque minerals are magnetite and reflect dull silver grey. **C**) Dolomite vein bordered by goethite-stained dolomite cutting through a chlorite-rich host rock. **D**) Sample 1305.85-1305.95 ft. Serpentine-rich host rock cross-cut by a dolomite vein bordered with fibrous goethite-stained dolomite. Vein core is replaced by silica (grey in XPL). Minor apatite in the lower left part of the image.

Chlorite (green-grey in PPL, Blue-green in XPL); Clay (white in PPL, dark grey in XPL), Serpentine (pale brown in PPL, yellow-blue in XPL); Magnetite (opaque); Hematite (red); Goethite (orange-yellow); Dolomite (pastel high order colors in XPL); Apatite (colorless in PPL, grey in XPL, round, fractured, high relief)

Veins in the lower phyllosilicate zone vary from ~ 1 cm to sub-mm in thickness, and they share a similar composition of dolomite cores bordered with comb texture or fibrous goethite-stained dolomite (Figure 10), suggesting a change in mineralization conditions (see: Dong et al. 1995). A few veins are lined with amorphous silica (Figure 10C). Sample BO-1_1305.85-1305.95 features an unusual brecciated green phyllosilicate (celadonite?) vein cross-cutting a larger dolomite vein (Figure 10D). This exact mineralogy is uncertain because there was not enough material for XRD analysis and it is the only occurrence of this green material in the samples selected for this study. The vein core textures include can also be prismatic or fibrous, with the fibrous form appearing as either the entire vein or successive banding with occasional semi-spherical or spherulitic textures (crustiform to colloform: Dong et al., 1995; Taylor 2009; Moncada et al., 2012).

4.3.3 Hydrogeologic Properties

The pore geometry in three samples from this zone center around leached grains in clay-rich areas (Figure 5C), or along open-mode fractures (Figure 5D; porosity = $0.2 \pm 0.0 - 1.7 \pm 0.2\%$);). The three samples tested for permeability are generally similar to the UPZ (2 ± 1 mD, 2 ± 3 mD), with a notable increase (443 ± 644 mD) in one sample due to an open fracture parallel to a filled vein (Figure 6D).

4.3.4 Whole-rock Mineralogy and Geochemical Composition

Fourteen samples were analyzed for XRD in the lower phyllosilicate zone (Table 1). Hematite, goethite, and Fe-Mg carbonates (dolomite, siderite) form the major mineral constituents. Other metal oxides such as rutile, chromite, and spinel are locally detected in hematite-rich samples. The chlorite and serpentine viewed in thin section are not detected

in XRD except for two samples, likely because they do not occur in significant enough quantities. Clays detected in the previous zone decrease in favor of minor to major amounts of species-unspecific mica detected, which may be associated with the observed chlorite. Locally, apatite, graphite, and quartz are detected.

The Na₂O (<1%) and SiO₂ (14 - 37%) percentages are extremely low throughout this lower phyllosilicate zone (Figures 6-8, Appendix C). K₂O values are significantly higher in zone than anywhere else in the drillcore at the 90% confidence interval (2 - 6%), which may correspond to the micaceous material observed in thin section and XRD. FeO has a generally strong presence in this zone (22 - 40%) and is significantly higher than in the upper phyllosilicate zone. Al₂O₃ is significantly lower in this zone than the upper phyllosilicate zone. The LOI values are variable, but generally high compared to lower in the drillcore (7 - 19%; Figures 6 & 7) and is not statistically different from the upper phyllosilicate zone (Figure 8). The fault at 391.15 m (1283.30 ft) is associated with increases in MnO and CaO concentrations, increases in LOI, and corresponding decreases in concentrations of SiO₂ and Al₂O₃. Using fluid-immobile trace element ratios Zr/Ti and Nb/Y, these samples suggest a mafic (basalt) protolith composition (Figure 9A). Similar to the upper phyllosilicate zone above, the silica concentrations in these samples are too low to solely rely on the TAS plot for lithologic composition due to the secondary mineralization (Figure 9B).

4.4 Nonconformity Interface: Transition Zone

4.4.1 Mesoscopic Observations

A fault separates the overlying phyllosilicate zone from this transition zone that occurs between 401.92 – 406.00 m (1318.65 – 1332.00 ft; Figure 3E). This zone is gradational and defined by strong presence of clays/micas and dolomite in the upper part of the zone and primarily silicate minerals below (Figure 17). Red-black hematite alteration is more pervasive throughout this section of the drillcore. Drillcore samples grade from a softer yellow-brown altered fine-grained material at the fault (Figure 3E, 17A) to darker, harder black and red crystalline rock (Figure 17C). Lighter banded zones within the sample are more likely to react with HCl.

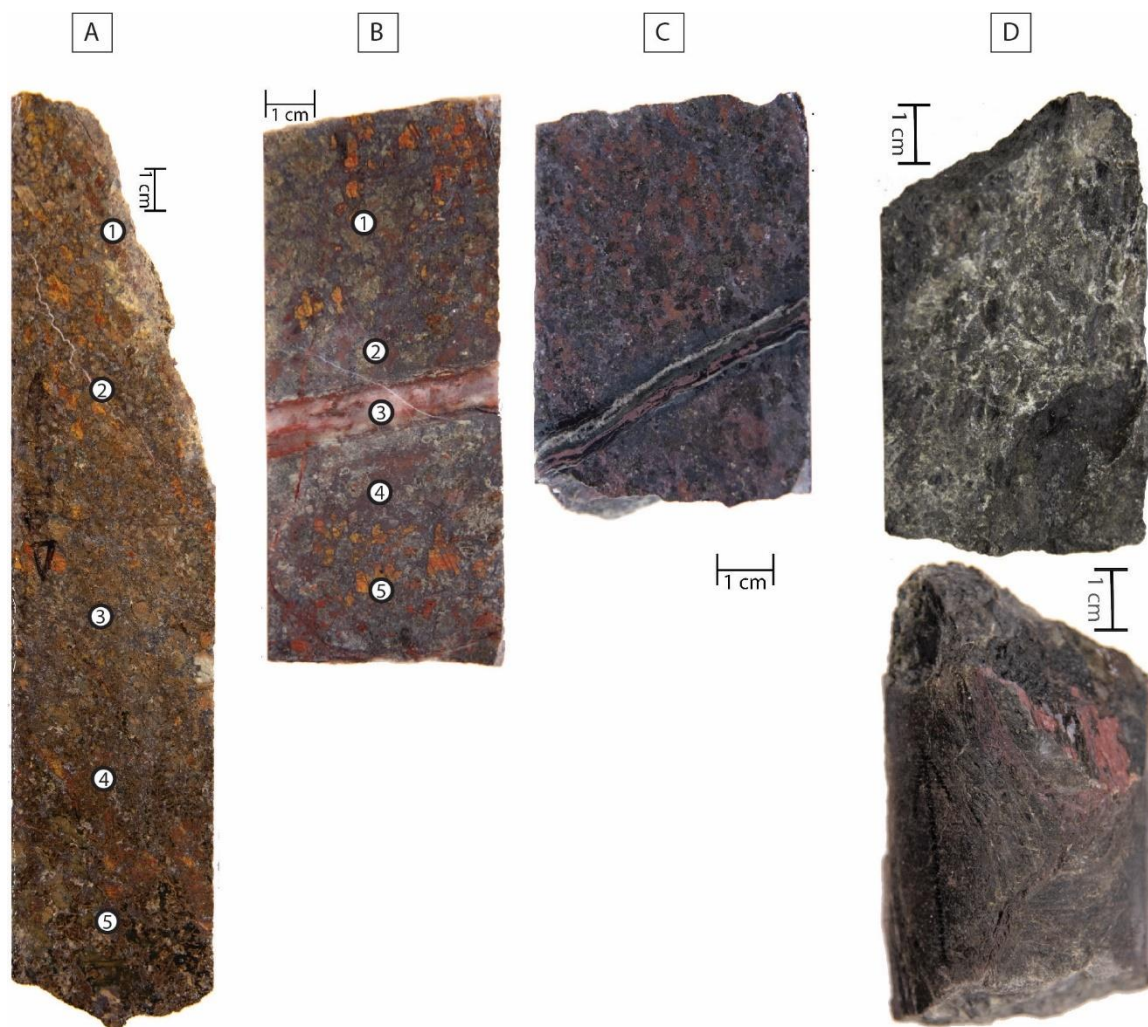


Figure 17: Nonconformity transition zone samples from the BO-1 Drillcore. Numbers indicate permeability test site locations. **A)** Sample 1318.65-1319.35 ft. Dolomite-rich host rock with powdery slip surface. **B)** Sample 1319.90-1320.25 ft. Major dolomite (reacts in HCl), Fe-oxides. Some accessory metallic minerals- occasional pyrite, but mostly graphite (ID'd in XRD). Vein is quartz with graphite (in XRD) and hematite (observed red stain). **C)** Sample 1327.70-1327.90 ft. Host rock composed of dolomite and hematite. More crystalline than previous samples. More abundant pyrite. Vein is carbonate (white, fizzes in HCl), quartz (dark grey), and hematite (red). **D)** Sample 1330.40-1330.60 ft. Slip surface separating this zone from the below metagabbro. Primary surface (top image) is undulatory with slickenlines and reacts with HCl. Secondary slip surface (bottom image) does not react.

This transition zone is marked by variable mineralogical compositions and includes several additional fault traces, vein networks, and fractures with a range of orientations (Figure 17). The fault separating the overlying phyllosilicate zone from this transition zone is non-cohesive gouge with slickenlines on scaly clay surfaces, dipping $\sim 70^\circ$ (Figure 3E, 17A). This gouge material also contains carbonate, indicated by a strong reaction to HCl. At ~ 405.5 m depth (Figure 17D) a waxy, undulatory, and multi-layered slip surface approximately parallel to the core axis occurs in a black, fine-grained, host rock. This slip surface reacts with HCL, unlike the host rock and red (hematite?) secondary slip surface dipping $\sim 65^\circ$. Fine scale carbonate veins pervade the upper samples in this zone. There is also a ~ 1 cm quartz vein cross-cut by fine-scale dolomite veins (Figure 9E; 17B) and a layered hematite, quartz, and carbonate vein (Figure 9F; 17C). This zone is faulted at a rate of ~ 1.5 /m.

4.4.2 Petrographic analysis

At the microscale, the 3 thin sections show a decreasing quantity of goethite and increasing quantity of silicate minerals as the drillcore transitions from clay-mica zone to the amphibolite below (Figure 18). The first thin section at the fault separating the lower phyllosilicate zone from the transition zone is composed of clays, carbonates, and iron-oxide minerals (Figure 4E, Figure 18A). Most grains are too diffuse, sheared, and anhedral to identify. Apatite grains are visible throughout the sample and are more intensely fractured and rounded nearest the fault surface.

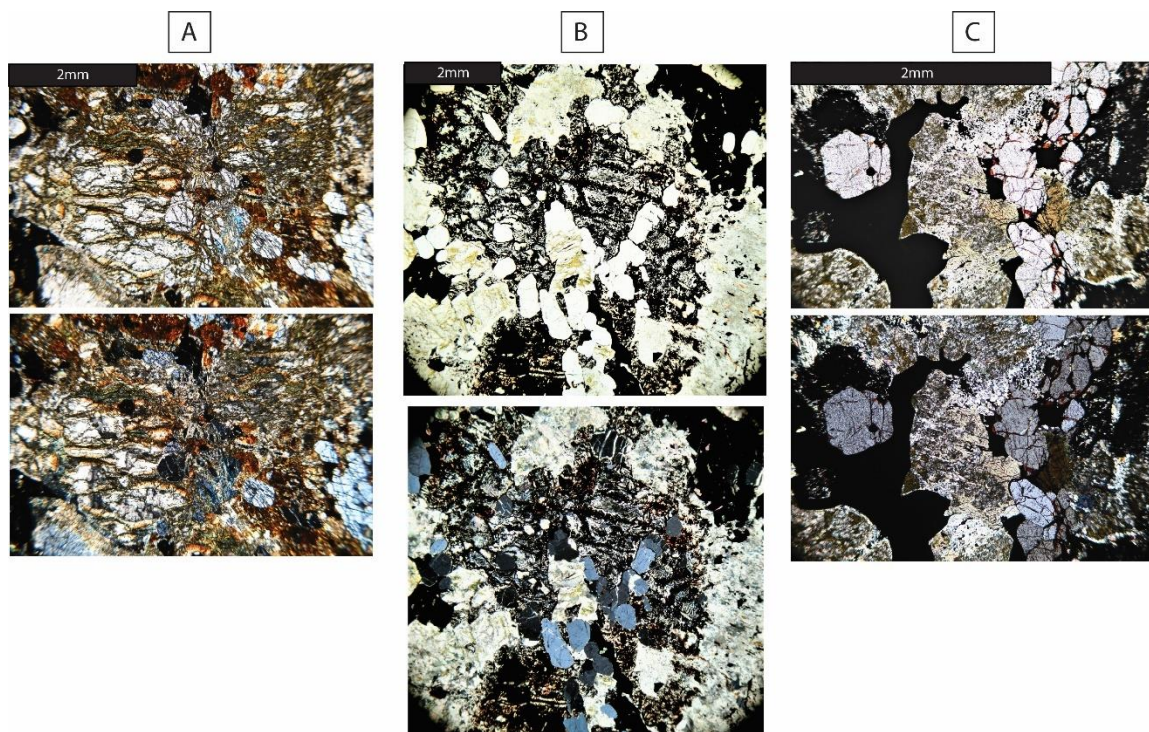


Figure 18: Nonconformity transition zone photomicrographs from the BO-1 Drillcore. Plane polarized light (PPL) images on the top row, cross polarized light (XPL) images on the bottom. Pore spaces are stained blue in PPL. **A)** Sample 1318.65-1319.35 ft. Major hematite + goethite, accessory magnetite, heavily fractured apatite. **B)** Sample 1319.90-1320.25 ft. Magnetite with clay + dolomite and apatite. **C)** Sample 1327.70-1327.90 ft. Opaque magnetite or pyrite, fractured apatite, clay + dolomite matrix with occasional remnant hornblende (yellow-green in PPL).

Clay (white in PPL, dark grey in XPL), Serpentine (pale brown in PPL, yellow-blue in XPL); Magnetite (opaque); Hematite (red); Goethite (orange-yellow); Dolomite (pastel high order colors in XPL); Apatite (colorless in PPL, grey in XPL, round, fractured, high relief)

As samples become darker and more crystalline in hand sample, the presence of magnetite increases across the thin sections. In the second thin section, grain boundaries are subhedral. Residual feldspar cleavage is visible, and the original minerals have been replaced by clay and dolomite. Iron minerals show intergrowth (symplectite) textures (Figure 18B). The vein in this sample is quartz with minor hematite and cross-cut by fine scale dolomite (Figure 10E). The final thin section has magnetite concentrated along cleavage planes of altered pyroxene or amphiboles, with primarily silicate minerals occasionally present (Figure 18C). The vein in this sample is complex, layered with hematite, carbonate, silica, and serpentine-chlorite (Figure 10F).

4.4.3 Hydrogeologic Properties

The 2 samples with porosity and permeability measurements are generally low (0.1 ± 0.0 & $0.6 \pm 0.1\%$; <1 mD; Figure 5) compared to the upper regions of the drillcore. The higher values are associated with alteration in close proximity to fault slip surfaces (Figure 5E). Other pore channels are observed at fine scale fracture systems that are oriented parallel to filled veins (Appendix B).

4.4.4 Whole-rock Mineralogy and Geochemical Composition

A total of 7 XRD sample measurements show major presence of dolomite and siderite towards the top of the transition zone, within closest proximity to the fault (Table 1). Orthoclase is also detected, though not seen in thin section. At increasing depths, the mineralogic composition is characterized by increased presence of quartz as dolomite presence decreases. The Fe-oxide minerals viewed in thin section are not detected in XRD, except for in the last sample. Locally, apatite and graphite are detected.

In the 3 XRF analyses, the LOI is initially high and decreases with increasing depth (15 - 5%). The amount of Na₂O remains at 0.00%, whereas SiO₂ shows a slight trend towards increasing concentrations (Figure 6). All other oxides do not exhibit a clear pattern throughout the transition zone. The transition zone has statistically significant differences at 90% confidence in Al₂O₃, CaO, K₂O and MnO relative to silica content compared to the upper and lower phyllosilicate zones (Figures 6-8; Appendix C). Using immobile trace elements, these samples plot as a mafic protolith. However, the rocks are composed of secondary mineral phases as seen in thin section and XRD resulting in a silica content too low to plot within the standard TAS diagram (Figure 9).

4.5 Below the Nonconformity Interface: Amphibolite

4.5.1 Mesoscopic Observations

An amphibolite unit extends from 406.00 - 422.21 m (1332.00 - 1385.20 ft) and is separated from the above section by an ~0.6 m thick, multi-layered fault system (Figure 3F; Figure 19). Fault traces are curvilinear approximately parallel to core axis and display abundant slickenlines (extension of fault at Figure 17D). This zone is faulted at a rate of ~1.5/m. The host rock composed of fine-crystalline, dark material with red hematite, silver-grey magnetite, and accessory pyrite (Figure 19).

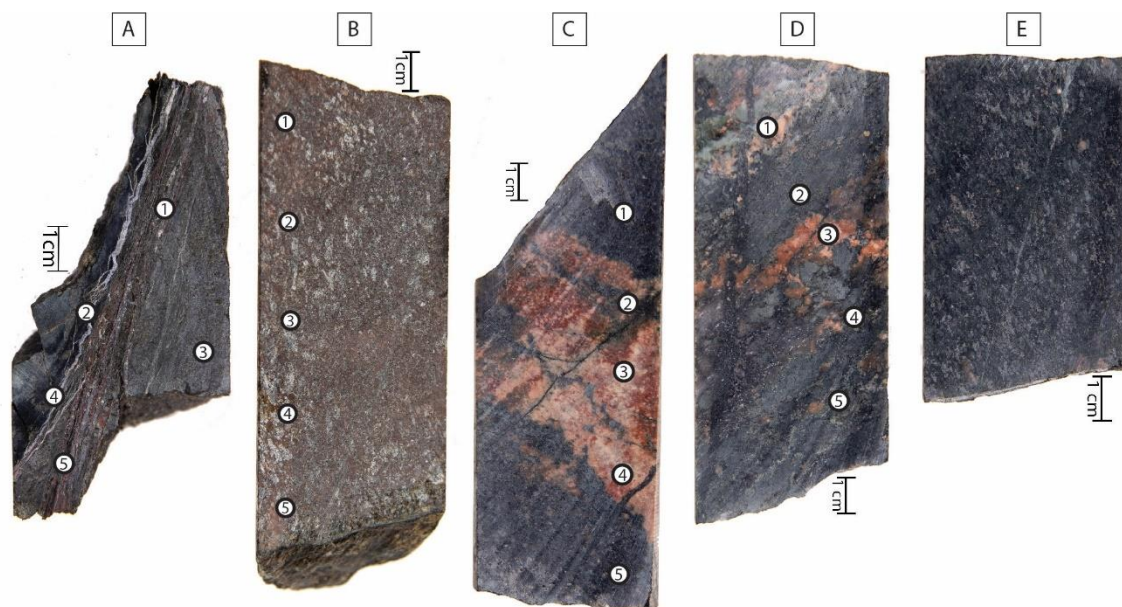


Figure 19: Amphibolite samples from the BO-1 Drillcore. Numbers indicate permeability test site locations. **A)** Sample 1332.30-1332.50 ft. Layered fault with fine-crystalline mafic host rock and anastomosing carbonate (reacts with HCl), hematite (red), and silica infills. **B)** Sample 1344.00-1344.40 ft. Hematite (red) and magnetite (reflective)-rich host rock with slip-surface on the lower part of the sample. Pyrite also present. **C)** Sample 1347.60-1348.00 ft. Slip surfaces on the upper side and rear of the sample. Host rock is fine-crystalline. Black veins react with HCl. **D)** 1366.20-1366.60 ft. Layered black amphibole, grey quartz in upper left, feldspars. Accessory pyrite. **E)** Sample 1381.70-1382.00 ft. Diabase with 1mm dolomite vein on the very bottom of the sample, cross-cut by a ~3mm dolomite vein dipping ~70°.

4.5.2 *Petrographic Analysis*

Across the 5 thin sections in the gabbro, plagioclase is highly sericitized with faint cleavage remaining (Figure 20). Areas with high quantities of carbonates and phyllosilicates are less common and/or are localized to veins or slip surfaces (Figure 4F, Figure 20C). Samples are primarily composed of albite and amphibole (usually hornblende). Phyllosilicates occasionally pervade hornblende crystals or appear as rims around mafic crystals (Figure 4G; Figure 20). The fault zone separating this section from the overlying alteration zone displays anastomosing vein networks with quartz and calcite infillings (Figure 10G).

4.5.3 *Hydrogeologic Properties*

Permeability measurements on 4 samples within this lithologic unit show extremely low permeability values (<1 mD; Figure 5; Appendix A). Porosity is also very low ($<0.1\pm 0.0$ - $0.3\pm 0.0\%$) with an increase (to $0.9\pm 0.1\%$) in sample 406.10 m (1332.30 ft) which features an open slip surface (Figure 5F; Appendix B). In general, pore network channels are limited to open fractures parallel to slip surfaces or vein infillings (Figure 5F). Leached grains and dilated features decrease relative to what was observed in overlying more highly altered zones.

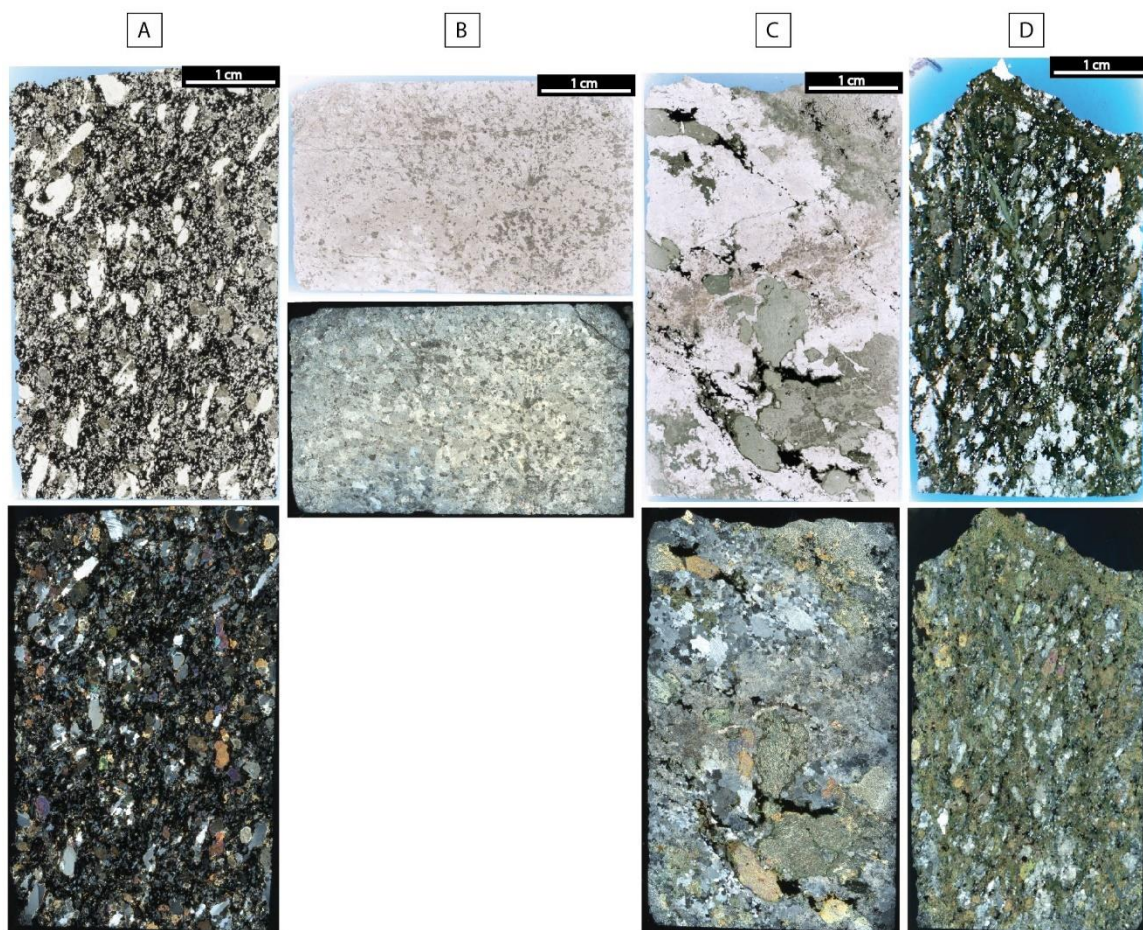


Figure 20: Amphibolite thin section scans from the BO-1 Drillcore. Plane polarized light (PPL) images on the top row, cross polarized light (XPL) images on the bottom. Pore spaces are stained blue in PPL. Field of view is standard 27 mm x 46 mm thin section. **A)** Sample 1344.00-1344.40 ft. Hematite-magnetite (opaque)-rich host rock with apatite (grey in XPL) and amphibole (colorful in XPL). **C)** Sample 1347.60-1348.00 ft. Sericitized albite from the pink portion of the hand sample. Minor chlorite present. **D)** 1366.20-1366.60 ft. Albite (white in PPL) with green hornblende. Fine-scale carbonate vein through the middle of the sample, surrounded by grey-brown sericite. **E)** Sample 1381.70-1382.00 ft. Hornblende (green), sericitized albite (white in PPL) with pyrite opaques. Refer to data repository for high-resolution image files.

4.5.4 Whole-rock Mineralogy and Geochemical Composition

Mineralogy results from 10 XRD samples show a host rock typically composed of albite, and various amphiboles such as tremolite, hornblende, and glaucophane (Table 1). Chlorite, muscovite, and Fe-Ti-oxides (hematite, ilmenite, spinel) are common minor constituents. Apatite and graphite are detected locally. Zeolites are detected in several samples at very low quantities. Vein infillings include carbonate and quartz.

In the 5 samples analyzed for whole-rock geochemistry (XRF), all relative major oxide concentrations are significantly different from the transition zone at the 90% confidence level (Figures 6-8). The most notable difference from the overlying transition zone is that Na₂O is present (range: 2 - 4%), likely corresponding to the albite observed in thin section and XRD (Figures 6-8). LOI values stay below 2% for the remainder of the drillcore (Figure 7, Appendix A7). The MnO concentrations remain <1% and K₂O concentrations also remain low (range: ≤1%). The relative Al₂O₃ concentrations are significantly higher in the amphibolite compared to the transition zone (Figure 8), and the concentrations are variable (range: 8 - 20%; Figures 6 & 7). Sample trace and major element compositions generally plot as mafic/gabbroic (Figure 10 A, B).

4.6 Below the Nonconformity Interface: Layered Intrusions

4.6.1 Mesoscopic Observations

This basal lithologic unit (422.27 - 480.64 m / 1385.40 - 1576.90 ft depth) is a series of layered intrusions likely correlating to the NEIIC (Appendix A1). It is separated from the overlying amphibolite by a layered fault dipping ~70-85° relative to core axis, dissecting

diabase-texture host rock (Figure 3H; Figure 21A). The majority of samples are dioritic with black hornblende, white to purple feldspar, and lesser quartz (Figure 3J; Figure 21). Some layers within this section are more mafic in composition. The intrusive complex is least faulted than all previous sections, however, several faults are observed at the lithologic boundary and towards the base of the drillcore (Figure 2). Locally, intrusions of aplite to pegmatitic texture dikes occur (Figure 21 B & E). These intrusions are faulted and separated from the host rock by a slip surface, typically green with slickenlines in hand sample (Figure 3I). This unit is faulted at a frequency of $\sim 0.6/\text{m}$.

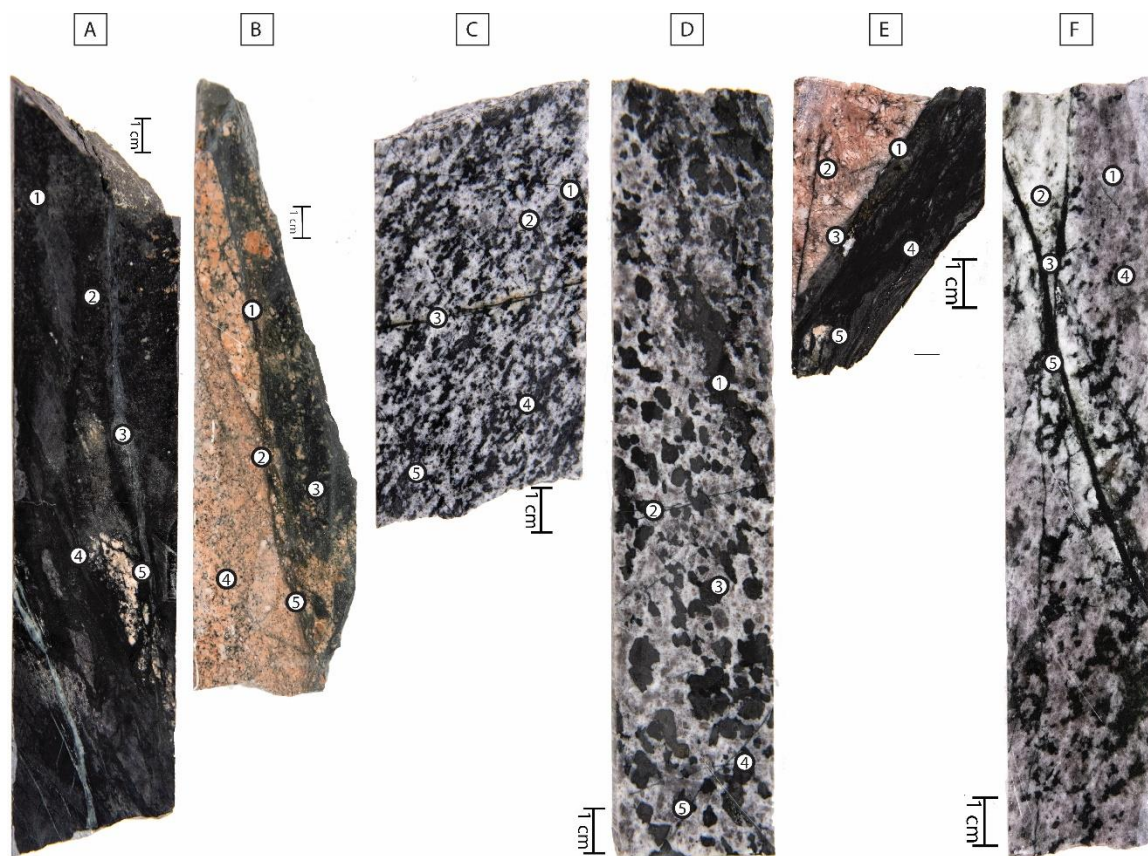


Figure 21: Layered intrusion samples from the BO-1 Drillcore. Numbers indicate permeability test site locations. **A)** Sample 1385.40-1386.00 ft. Layered fault separating the above gabbro from the layered intrusive complex. Matrix is fine-crystalline mafic material with larger, pink albite pods. **B)** Sample 1395.40-1396.00 ft. Layered pink albite and fine-grained green hornblende fault with cataclasite. **C)** Sample 1411.60-1412.00 ft. Grey albite with black tremolite. Fine-scale, black tremolite vein in the middle of the sample. **D)** Sample 1447.70-1448.25 ft. Grey albite with black hornblende, many small-scale tremolite veins. **E)** Sample 1459.40-1459.60. Aplite dike faulted against layered, mafic material. Slickenlines visible on lower surface. **F)** Sample 1472.3-1473.00. White to purple albite with some minor dark grey quartz and black hornblende.

4.6.2 *Petrographic Analysis*

Of the 16 thin sections in the layered intrusions, 9 samples are from diorite-amphibolite, 4 are faults, and 3 have granitic composition (Figure 4, Figure 22). The diorite-amphibolite samples are composed of feldspar and hornblende (Figure 4J; Figure 22). Phyllosilicates (biotite, chlorite) are present as either alteration rims around hornblende or it pervades the whole crystal. All feldspars display some degree of sericitization but appear relatively fresh compared to the rest of the drillcore. Some, though not all samples have quartz or chlorite. The granitic intrusions are composed of fine crystalline, often sericitized feldspar, quartz, minor hornblende and muscovite (Figure 22A).

Slip surfaces in general throughout this zone are composed of layered hornblende with phyllosilicates (biotite, chlorite), serpentine, with or without quartz, clays, or apatite (Figure 4H & 4I). Vein infills include prehnite and serpentine (Figures 4H & I, 10H). Structures other than faults are minimal, though a few samples show hairline mafic intrusions (Figure 22D)

4.6.3 *Hydrogeologic Properties*

Overall, the layered intrusions are largely composed of impermeable material (<1 mD) with low porosity (<0.1 - 2.1 ± 0.3%) (Figure 5; Appendices A & B). The majority of open pore spaces are associated with faults and/or associated fractures that dissect the drillcore (Figure 5). There are no fractured grains as seen in overlying alteration zones.

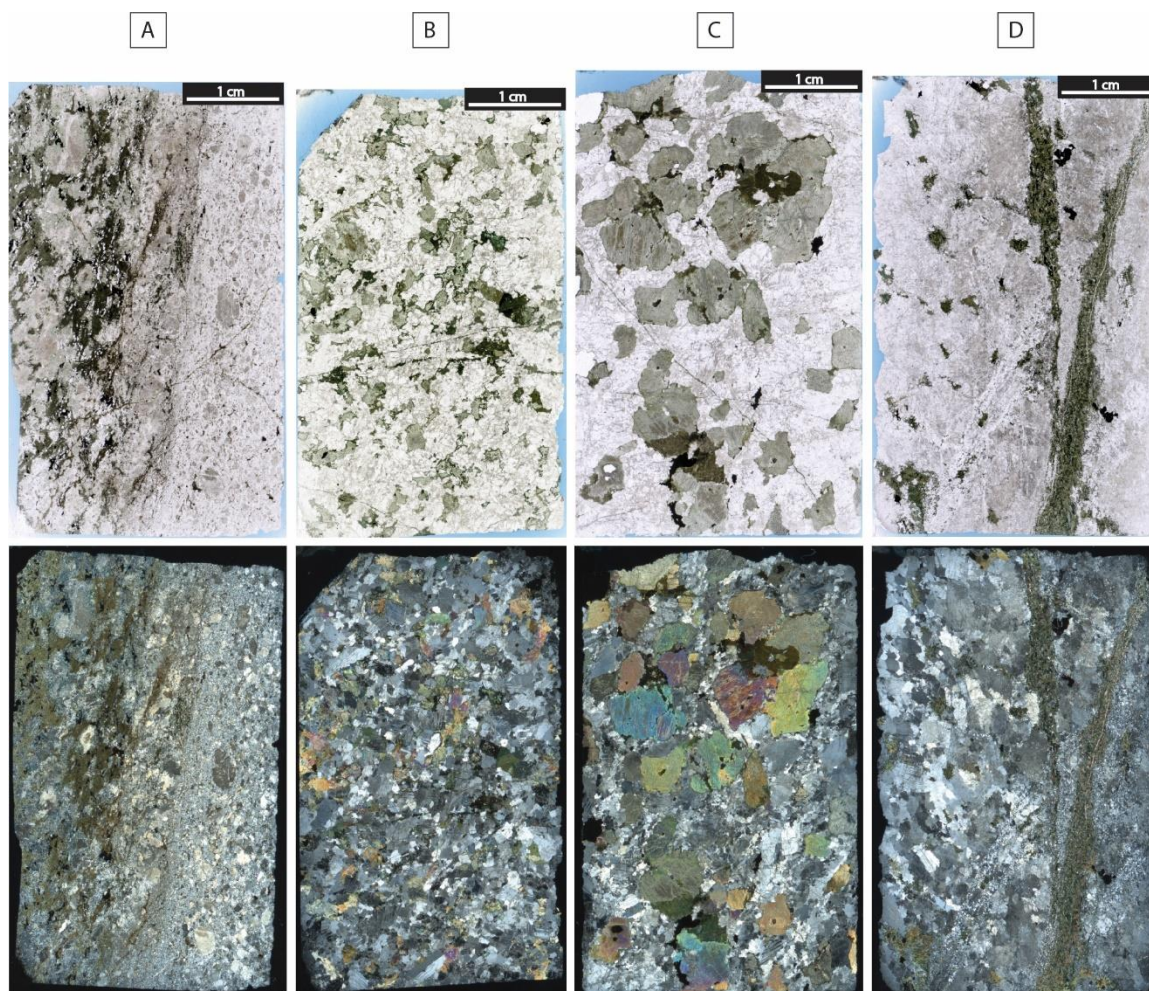


Figure 22: Layered intrusion thin section scans from the BO-1 Drillcore. Plane polarized light (PPL) images on the top row, cross polarized light (XPL) images on the bottom. Pore spaces are stained blue in PPL. Field of view is standard 27 mm x 46 mm thin section. **A)** Sample 1395.40-1396.00 ft. Sericitized albite (grey-brown in PPL) with layered tremolite and chlorite-serpentine in the slip surface. Fine-grained cataclasite separates the right and left half of the image. **B)** Sample 1411.60-1412.00 ft. Albite and anorthite (white in PPL) with green amphibole. **C)** Sample 1447.70-1448.25 ft. Albite and anorthite (white in PPL) with green amphibole and opaque ilmenite. **D)** Sample 1472.30-1473.00 ft. Sericitized albite (grey-white in PPL) with minor quartz and mafic intrusions. Refer to data repository for high-resolution image files.

4.6.3 *Whole-rock Mineralogy and Geochemical Composition*

The 25 samples analyzed for XRD confirm a predominantly albite composition with occasional anorthite or microcline, and frequently detected amphiboles (hornblende, tremolite, actinolite; Table 1). Other minor constituents include graphite, bornite, and chlorite-serpentine (associated with slip surfaces). The granite-aplite samples are predominantly quartz and albite with minor hornblende.

In the 12 XRF samples, there are no significant differences in relative oxide concentrations between the layered intrusions and the overlying amphibolite at the 90% confidence level (Figures 6-8). All relative oxide concentrations are significantly different from the nonconformity zones. The highest concentrations of SiO₂ values are measured in this section, except for the sandstone bedrock section above the nonconformity (range: 35 - 77%). The highest SiO₂ concentrations (~75%) correspond with the pegmatitic or aplite intrusions, which have significantly different relative oxide concentrations compared to the surrounding layered intrusions. (Figures 8 & 9). These samples in this unit generally plot as mafic-intermediate on the TAS and basalt discrimination plots (Figure 10A, B).

4.7 B-1 Drillcore

The photographic and sample record for the B-1 drillcore is not as continuous and the drillcore diameter is much smaller (BQ - 3.64 cm diameter), limiting the amount of sample material and feasibility of some analysis techniques (e.g. permeability and XRF). The chemical and petrographic record provides insight into the degree of lateral variability

of the nonconformity interface contact at the kilometer scale in subsurface settings with regional to local fault systems.

4.7.1 Above the Nonconformity Interface: Sedimentary Bedrock

The sedimentary bedrock portion (703.80 – 724.00 ft / 214.52 - 220.68 m) is a similar in composition to BO-1 drillcore, but the B-1 drillcore contains more finely bedded silty intervals than the BO-1 sandstone. Shared features include poorly sorted quartz sandstone (Figure 23). Yellow goethite staining is infrequent, but still present in the sampled intervals. Many sections of the drillcore exhibit pitted textures surrounding leached grains (Figure 23A). Open fractures occur along bedding planes and no faults are observed above the nonconformity. In the 3 thin section samples, the quartz grains are often poorly sorted, fine to granule size, and subrounded (Figure 24). Some quartz grains are metamorphic, or have experienced compaction, displaying undulose extinction. Opaque minerals occasionally line pore spaces. Minor clays are also present. In 3 XRD samples, minor pyrite, magnetite, and calcite are also detected (Table 2).

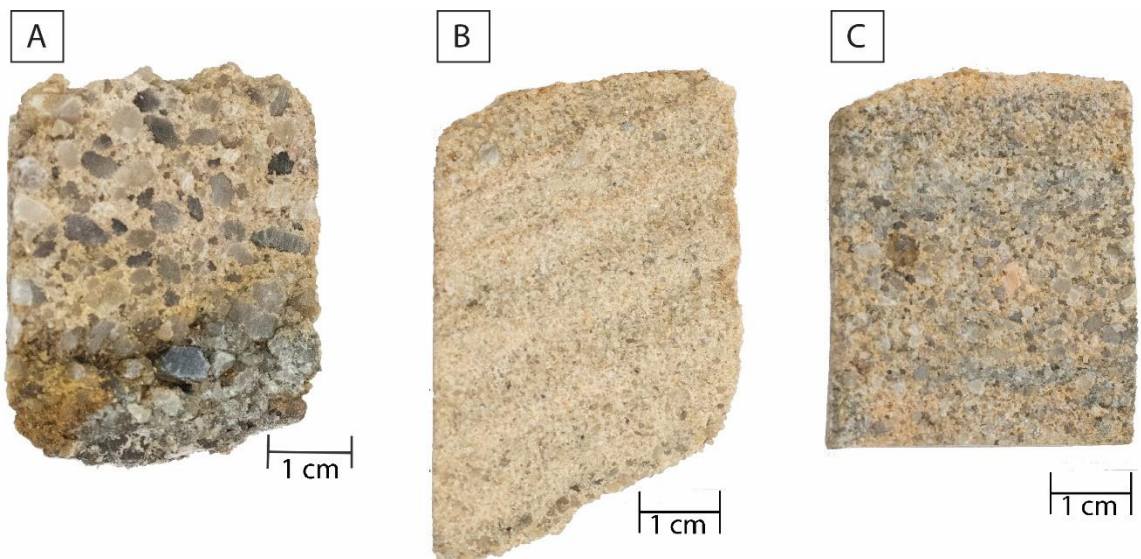


Figure 23: Quartz arenite samples from the B-1 drillcore. A) Sample 703.80-704.00 ft. Coarse grain quartz sandstone with quartz granule clasts. Grains are rounded to subangular. Base FeOH staining is 1.5 cm wide. **B)** Sample 714.00-714.20 ft. Fine to coarse grain quartz sand with few granules. Small fining upwards sequences ~5-8mm thick. **C)** Sample 723.70-723.90 ft. Coarse grain quartz and feldspar sequence (peach-pink grains). Some ~5mm FeOH stained pits.

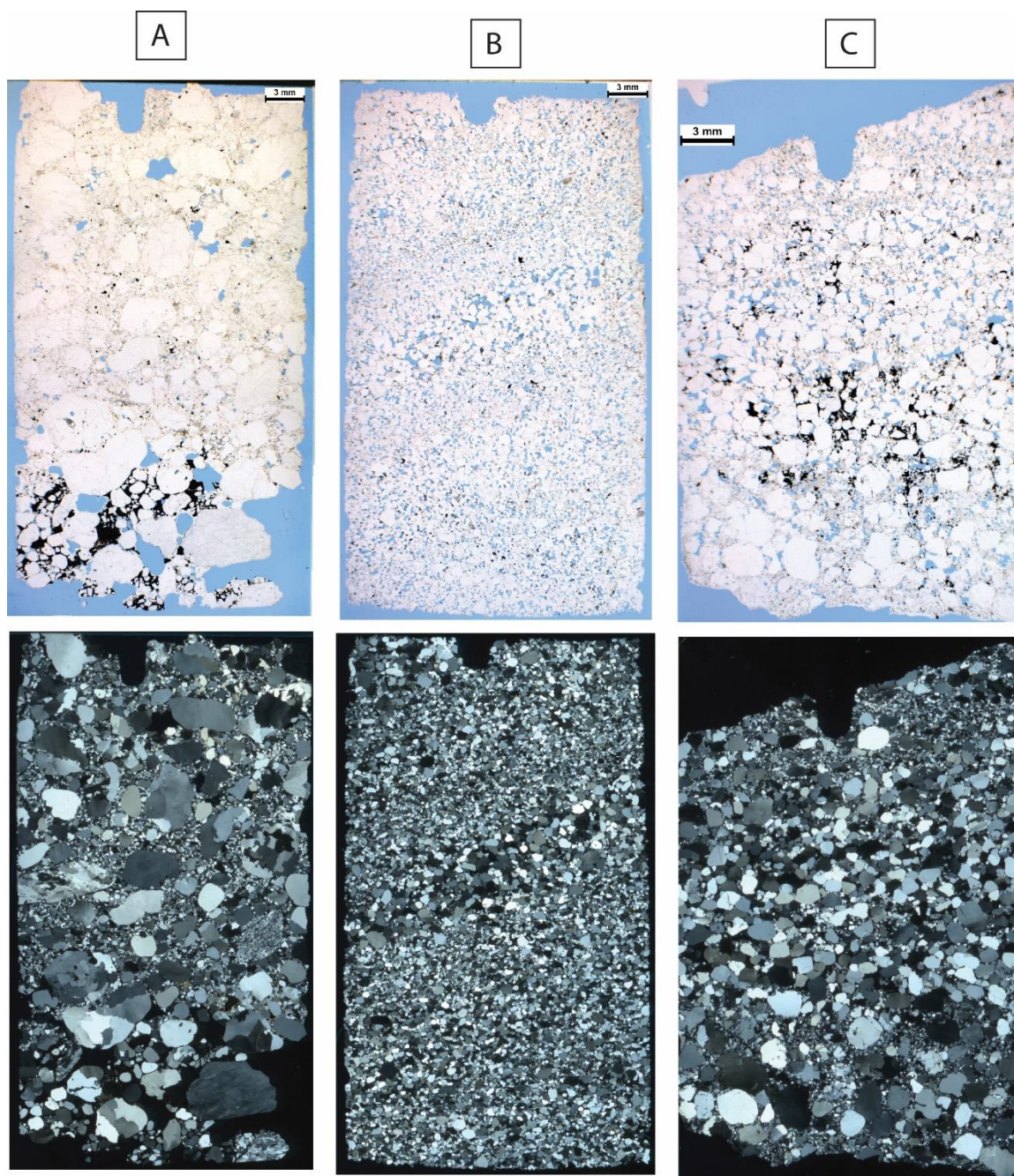


Figure 24: Quartz arenite thin section scans from the B-1 drillcore. Plane polarized light (PPL) images on the top row, cross polarized light (XPL) images on the bottom. Pore spaces are stained blue in PPL. Field of view is standard 27 mm x 46 mm thin section. **A)** Sample B-1_703.80-704.00. Note the lower part of the sample with Fe-oxide cement around quartz grains in PPL. In XPL, sutures within larger quartz grains are visible. **B)** Sample B-1_714.00-714.20. Fine to coarse grain quartz sand with few granules. Small fining upwards sequences ~5-8mm thick. Minor Fe-oxide, black grains in PPL. **C)** Sample B-1_723.70-723.90. Some pyrite mineralization around quartz grains, seen in black in PPL, reflects gold. Refer to data repository for high-resolution image files.

Table 2: Qualitative XRD analysis for the B-1 drillcore. Mineral concentration marked with shaded boxes. Dark blue: major, medium blue: minor, light blue: detected.

Depth (ft)	Quartz	Feldspar	Inosilicates	Phyllosilicates	Other Silicates	Carbonates	Sulfate/sulfide	Oxides
703.8- 704 A	Quartz					Calcite		goethite
703.8- 704 B	Quartz						Pyrite	
714.0- 714.2	Quartz					Dolomite, Witherite		Goethite, Spinel
723.7- 723.9	Quartz	Albite					Pyrite	Spinel
724.0- 724.2		Orthoclase		Palygorskite		Dolomite		Anatase
732.0- 732.3		Orthoclase		Dickite		Dolomite		Spinel, Anatase
732.6-732.8 A	Quartz	Albite	Enstatite					Goethite, Anatase
738.0- 738.3 A			Pyroxene			Siderite, Dolomite		Goethite
738.0- 738.3 B				Chlorite		Siderite		Ilmenite, Pyrolusite
744- 744.3 B	Quartz	Albite	Diopside		Epidote			Hematite, Ilmenite
750.0- 750.2	Quartz	Albite			Olivine			Ilmenite
784-784.25	Quartz	Ca-Albite				Magnesite		Hematite
792.0- 794.0		Albite		Chlorite, Biotite				Ilmenite
913- 913.2		Albite, Anorthite			Forsterite	Magnesite		Ilmenite, NiO
950- 950.2		Albite			Olivine			Perovskite
1026-1026.3 A	Quartz	Albite			Forsterite			Hematite, Perovskite
1026-1026.2 B		Ca-Albite			Forsterite			Ilmenite
1120-1120.4		Ca-Albite			Wollastonite	Calcite		
1121.4-1122.3 A		Albite		Chlorite		Calcite		Ilmenite
1121.4-1122.3 B				Kaolinite, Chlorite		Calcite		

4.7.2 Nonconformity Interface

The B-1 drillcore intersects the nonconformity at 724.00 ft (220.68 m), which correlates to ~ 47 m above where the BO-1 drillcore intersects the nonconformity. The nonconformity below the sedimentary samples is a pale green, clay-rich zone composed of unconsolidated fine and weathered material for ~2 m (~ 6.5 ft; Figure 25A). Core retrieval was poor over this interval (~ 17%). As a result, there are no thin sections for this interval. Rock chip XRD analysis on one sample shows the presence of dolomite, K-feldspar, palygorskite, ± anatase (Table 2).

4.7.3 Nonconformity Interface: Clay Altered Gabbro

Immediately underlying the unconsolidated argillic alteration, alternating layers of cohesive grey and brown clays are present (Figure 25B). This alteration is similar to the clay altered layer at the nonconformity boundary of BO-1 drillcore (See Figure 3B) The ultrafine brown layers react readily with HCl.

In one thin section (Figure 26A), the grain boundaries or mineralogy are not discernible with no clear foliation direction. The grey-white areas include clays and serpentine. The brown areas are composed of carbonates and goethite. There are a few brecciated, opaque minerals (magnetite?) and mesh textures visible at the micro-scale. In XRD, detectible minerals include K-feldspar, dolomite, dickite, with minor amounts of anatase and spinel (Table 2).

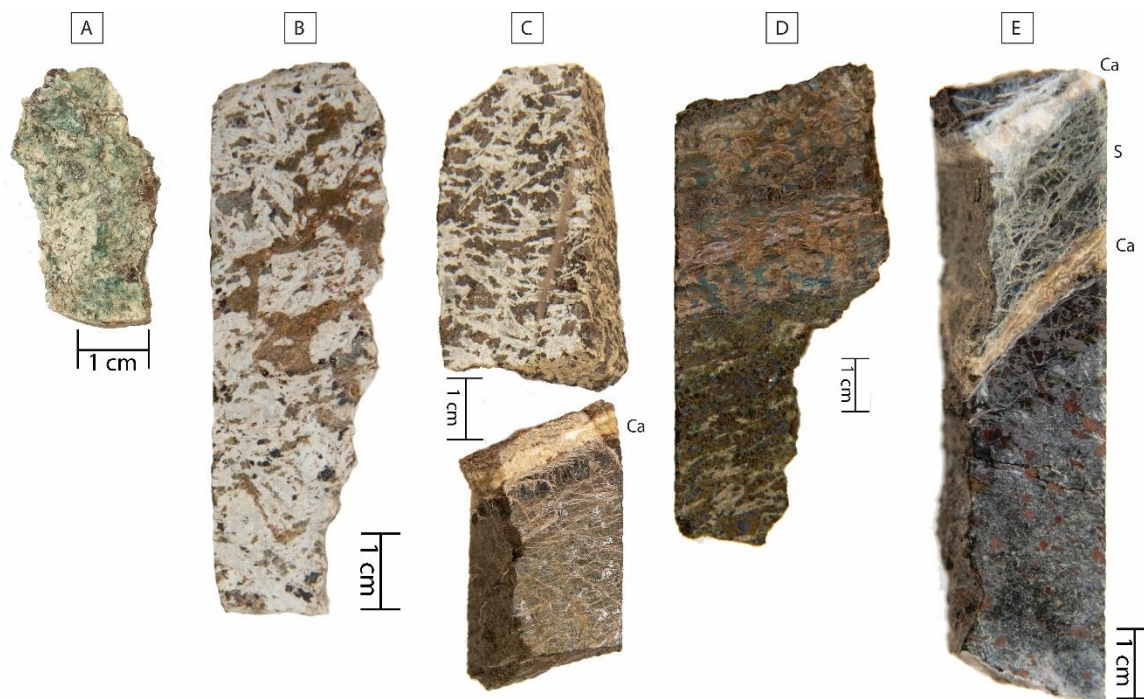


Figure 25: Clay-altered nonconformity boundary samples from the B-1 drillcore. **A)** Sample 724.00-724.20 ft. Poorly consolidated nonconformity boundary, core orientation unclear. **B)** Sample 732.00-732.30 ft. Platy white clay-altered feldspars and oxidized brown material. **C)** Sample 732.60-732.80 ft. Top half: Platy white feldspars with carbonate-rich, oxidized brown material. Lower half: Carbonate vein on top. Serpentine-rich host rock has anastomosing veinlets. **D)** Sample 738.00-738.30 ft. Dolomite + goethite vein on the upper part of the samples with chlorite + dolomite matrix. **E)** Sample 744.00-744.30 ft. layered calcite and serpentine veins in a serpentinized gabbro host rock. Minerals: Ca- calcite; S- serpentine.

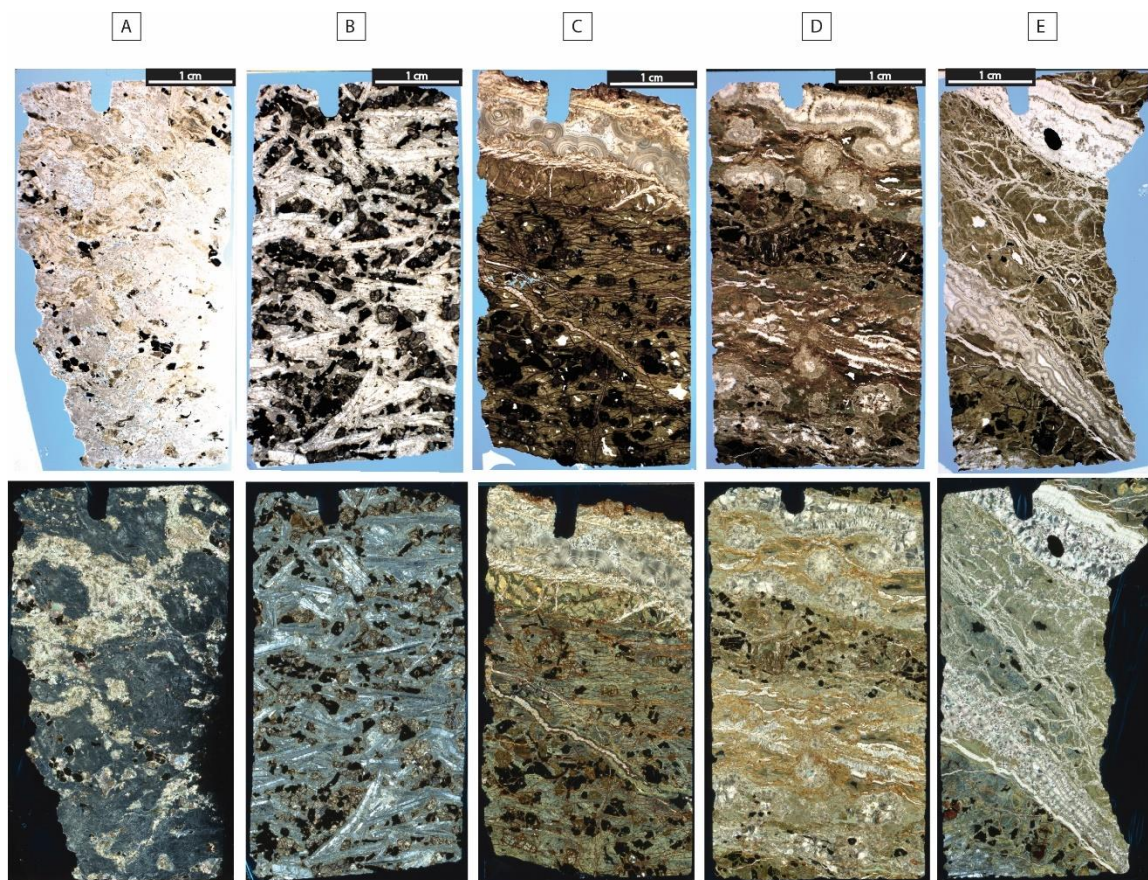


Figure 26: Clay-altered nonconformity boundary thin section scans from the B-1 drillcore. Plane polarized light (PPL) images on the top row, cross polarized light (XPL) images on the bottom. Pore spaces are stained blue in PPL. Field of view is standard 27 mm x 46 mm thin section. **A)** Sample 732.00-732.30 ft. Platy white clay-altered feldspars and oxidized brown material. **B)** Sample 732.60-732.80 ft. top half: Platy white feldspars with carbonate-rich, oxidized brown material. **C)** Sample 732.60-732.80 ft. lower half: Carbonate vein in serpentine-rich host rock with anastomosing veinlets. **D)** Sample 738.00-738.30 ft. **E)** Sample 744.00-744.30 ft. layered calcite and serpentine veins in a serpentinized gabbro host rock. Refer to data repository for high-resolution image files.

In sample B-1_732.6-732.8_A, sericitized feldspar occurs with some original material (clasts?) remaining in the grey clays (Appendix A1). Brown layers in hand sample (Figure 25C) and confirmed in thin section (Figure 26B), are dolomitized. Sample XRD analyses indicate the presence of quartz, albite, cuprite, hematite, with minor anatase, and enstatite (Table 2).

4.7.4 Nonconformity Interface: Serpentine Altered Gabbro

A ~1 cm calcite vein separates the overlying clay altered zone from this serpentinized zone which ranges from 223.33-226.80 m (732.70-744.10 ft) (Figure 10I, 25C, 26C). Several layered and anastomosing calcite veins occur throughout this section (Figure 10; Figure 26). At the meso-scale, the samples are characterized by an ultrafine brown and green groundmass with distinct black and red blebs (magnetite, hematite; Figure 25). Micro-scale observations in 3 thin sections show the host rock is almost entirely replaced by serpentine (Figure 26). Carbonate veins are bordered by goethite stained-fibrous carbonate (Figure 10J; Figure 26). Brecciated opaque minerals are still present throughout this serpentine altered zone. Two XRD samples from this alteration zone show the presence of siderite, dolomite, hematite, chlorite, ilmenite, and pyrolusite (Table 2).

4.7.5 Below the Nonconformity Interface: Unaltered Gabbro

A multi-layered system of carbonate veins (Figure 10K; 26E) separates the overlying serpentine-altered gabbro unit from this unaltered gabbro unit (226.80-341.99 m / 744.10-1122.00 ft: end of core). There is also a ~ 1 cm section of serpentinized host rock that grades to weakly or unaltered gabbro dominated by plagioclase and olivine for the remainder of the drillcore with occasional intervals of heavy iron oxide. Feldspars are

tabular, semi-oriented, and display weak sericitization (Figure . Olivines are near pristine. Whole-rock mineralogy, as measured through XRD analyses of 7 samples, indicate the presence of plagioclase feldspar, olivine, ilmenite, hematite, and phyllosilicates (Table 2).

The two slip surfaces identified in the B-1 drillcore occur at 1120.40 ft (341.50 m) and 1122.00 ft (341.99 m) (Figures 27 & 28). At 341.50 m (Figure 28D), there is a ~0.5 mm layer of banded serpentine at the fault surface with fibers perpendicular to the fault plane. Olivines nearest the fault surface are serpentinized, with cleavage patterns still visible. Feldspars are sericitized and prehnite is also present. Alteration diminishes rapidly with increasing distance away from the fault slip surface to the point where olivines on the upper edge of the slide are almost pristine. The XRD analysis for this sample shows major presence plagioclase feldspar, with minor amounts of calcite (Table 2).

The slip surface at 341.99 m (1122.00 ft) is near vertical relative to the core axis and contains slickenlines (Figure 27E, 28E). The ~ 4 mm wide fault core is grey cement-filled. The host rock shows a similar texture to previous samples with cream-grey tabular feldspars and black mafic minerals with a dark grey halo. Grain boundaries between feldspars and grey halos are irregular and difficult to identify at this scale. In thin section, the fault core is composed of prehnite and fine-grained chlorite (Figure 10L). The prehnite crystals are semi-parallel to each other, forming perpendicular to the fault plane. More fine-grained prehnite extends beyond the fault core and into the host rock. Olivine crystals have been replaced by serpentine and feldspars are heavily sericitized. The XRD analysis for this host rock sample indicates chlorite, with minor Na-feldspar, calcite and ilmenite (Table 2). The slip surface material was analyzed separately and includes abundant chlorite and kaolinite, with minor calcite.

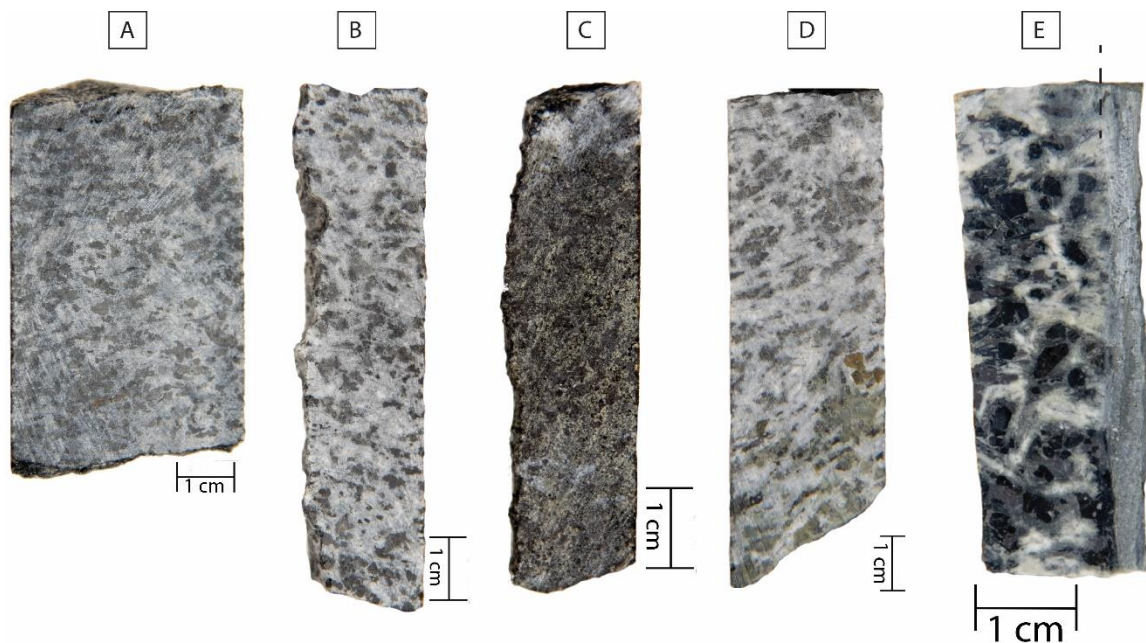


Figure 27: Gabbro samples from the B-1 drillcore. **A)** Sample 750.00-750.20 ft. Light grey albite and dark grey olivine. **B)** Sample 950.00-950.2 ft. Light grey albite and dark grey olivine. **C)** Sample 1026.00-1026.20 ft. light grey feldspar on top of sample, olivine cumulates (green) with magnetite (black). **D)** Sample 1120.00-1120.40 ft. Albite and olivine with slip surface on the bottom of the sample. **E)** Sample 1121.40-1122.00 ft. Faulted with slickenlines on the right side of the sample. Fault core is ~4mm wide. Host rock is white albite, black magnetite, and grey altered olivines.

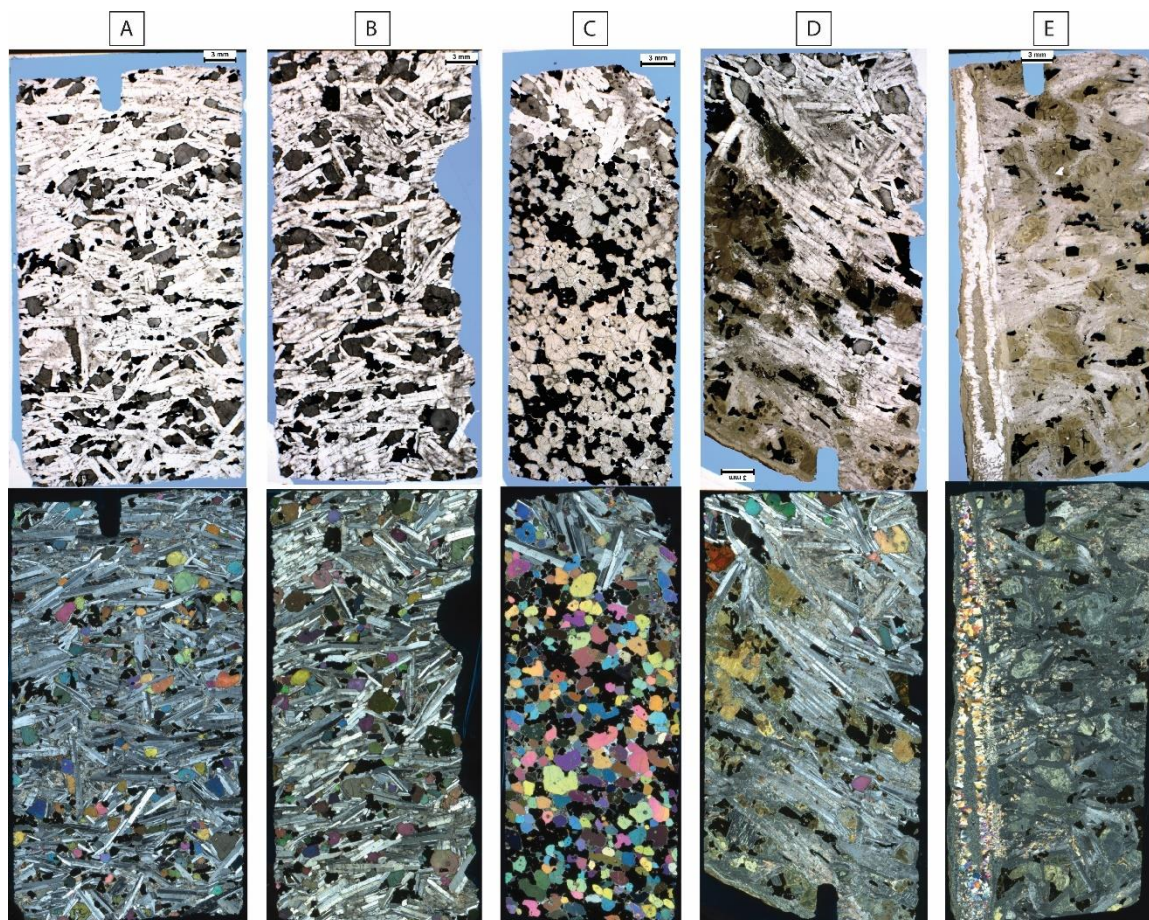


Figure 28: Gabbro thin section scans from the B-1 drillcore. Plane polarized light (PPL) images on the top row, cross polarized light (XPL) images on the bottom. Pore spaces are stained blue in PPL. Field of view is standard 27 mm x 46 mm thin section. **A)** Sample 750.00-750.20 ft. Albite and olivine. **B)** Sample 950.00-950.2 ft Albite and olivine. **C)** Sample 1026.00-1026.20 ft. Albite on top of sample, olivine cumulates with magnetite. **D)** Sample 1120.00-1120.40 ft. Albite and olivine with slip surface on the bottom of the sample. **E)** Sample 1121.40-1122.00 ft. Fault core is ~4mm wide on left side of image, composed of chlorite and prehnite (white in PPL, first to second order interference colors in XPL). Host rock is sericitized albite, black magnetite, and serpentinized olivines. Refer to data repository for high-resolution image files.

Albite (white in PPL); olivine (grey, high relief in PPL, third order interference colors in XPL); magnetite (opaque); serpentine (brown-green in PPL, yellow-green in XPL); chlorite (green in PPL, blue-grey fine grained in XPL).

5. DISCUSSION

This analysis of the nonconformity contact zone at ~ 1 – 1.5 km depth within the SE Minnesota drillcore analogs (Figure 1) offer a unique opportunity to examine the physical and chemical rock properties of crystalline basement rock underneath porous sedimentary reservoir injection sites within the midcontinent region. We delineate 3 distinct subsurface hydrogeologic units near the nonconformity interface based on meso- to micro-scale observations of composition, structures, mineral alteration assemblages (Tables 1, 2), and permeability measurements (Figures 5, 6). We use these results to develop a conceptual hydrogeologic framework for the subsurface. These nonconformity analog data support the hypothesis that the nature of the nonconformity interface will impact permeability architecture, mechanical rock properties, and fault reactivation in response to wastewater injection and provide critical geologic parameters for seismic risk models.

5.1 Geologic Features

In the BO-1 and B-1 drillcores (Figure 1), we observe a heterogenous mix of variably altered protoliths that include quartz arenite overlying mafic rock and a multi-layered mafic to intermediate intrusive complex, with occasional aplite dikes (Figures 2A). The nonconformity contact is irregular and displays topography, as seen in the ~47 m depth difference between where the two drillcores intersect the nonconformity. This is consistent with previous studies which observe topography along the nonconformity, either due to faulting or paleoweathering (Morey, 1977; Sims, 1990; Hamilton et al., 2021). The

drillcores display a variety of faulting and fracture intensity (Figure 2) and variable structure dip directions, which may be related to deformation along the nearby Belle Plain Fault Zone and Fayette Structural zone (Figure 1; Drenth et al., 2020).

Broad zones of moderate to extensive dissolution, mineralization, and alteration extend for 10's of meters vertical depth and 100's of meters laterally between the nonconformity interface contacts sampled in BO-1 and B-1 drillcores. A complex zone of alteration extends for ~ 22 m below the nonconformity boundary (Figure 2 C-D; Figure 29). This altered zone is the most intensely faulted portion of the drillcore compared to the less-altered protolith.

5.1.1 Fluid-Rock Interactions

We interpret the rocks examined to exhibit evidence of several episodes of fluid-rock interactions based on observations of layered vein composition and textures and secondary mineralization products. In the sedimentary bedrock we interpret the presence of pitted regions and hydrolytic alteration products as indicators for chemical weathering where acidic meteoric water reacts with feldspar to form clay (Delvigne, 1998; Boggs, 2006; Ulmer-Scholle et al., 2014). Iron oxides and hydroxides are present at varying intervals within the sedimentary region which co-occur with the pitted material and appear as coatings around grains (Figures 3A; 4A; 11; 12; 23; 24). The oxidizing zone continues into the basement units where the uppermost mafic protolith is altered to clays and iron-oxides (hematite, goethite) from primary feldspars and ferromagnesian mafic silicate minerals (Figures 25; 26 A, B, C; Boggs, 2006). Intense development of goethite through

the clay-zone overlaps with the majority of the lower phyllosilicate zone (Figures 3B-D; 4B-D; 15; 16). Mineral oxidation continues through the entire altered zone below the nonconformity (Figures 3E; 4E; 17; 18), below which iron oxide mineral assemblages (hematite, magnetite) are locally present in association with slip surfaces (Figures 19-22).

We interpret the lower phyllosilicate zone as the transition between primarily surface weathering-dominated or low temperature alteration vs. hydrothermally-dominated alteration in the crystalline basement rocks (Figure 15). These systems overlap at both the meso- and micro-scale and in XRD as observed by the co-occurrence of goethite and serpentine (Figure 16, Table 1). In the lower phyllosilicate zone, we note the presence of secondary alteration minerals: carbonate, serpentine, and mica minerals, which are diagnostic of hydrothermal environments (Figures 15-16; Table 1; Burnham, 1962; Bonnet and Corriveau, 2007; Shanks, 2012). This interpretation is supported by higher concentration of CaO, MgO, and LOI which is also diagnostic of this alteration (Figures 6-8; Burnham, 1962).

We observe evidence of carbonate deposition within centimeters of the nonconformity, overlapping in the drillcore where oxide minerals are present, and diminishing in the transitional zone (Figure 2; 13-18). Carbonates are present both in the matrix of the host rock and as layered veins (Figure 10). Since carbonates can be sourced from either weathering or hydrothermal-related processes, we rely on the textural evidence to infer variations in mineralization events and conditions (e.g., Dong et al., 1995; Moncada et al., 2012).

5.1.2 Vein Textures

Micro-textural observations also provide evidence for multiple episodes of mineralization at different mineralization conditions within fault and fracture infillings (Figure 10). We did not perform fluid-inclusion tests to understand boiling conditions within our samples, thus we infer fluid conditions based on the textural evidence gathered by Dong et al. (1995) and Moncada et al. (2012) who did perform fluid inclusion experiments and documented associated vein textures. Within veins we note the presence of silica and calcite mineralization textures associated with boiling fluid conditions, such as jigsaw, colloform, and crustiform crystallization, as well as non-boiling textures such as rhombic calcite, massive, cockade, and comb crystallization (Figure 10; Dong et al., 1995; Moncada et al., 2012). The presence of both boiling and non-boiling textures and brecciated and re-sealed veins across >20m depth from the nonconformity supports episodic fluid cycling and fluid distribution related to multiple stages of sealing or dilation related to deformation over a broad zone within the crystalline basement at different formation conditions (Figure 10; Sibson et al., 1998; Boullier et al., 2004; Williams, 2019). Mineralized faults and fractures are present to at least a depth of ~ 445 m (Figures 2, 3I, 4I, 21E).

5.1.3 Intensity of Alteration

Based on mineralogical and textural observations from the meso- to micro-scale within the two drillcore analogs, we created a relative intensity scale of alteration for the crystalline basement underlying the nonconformity contact: 1) weak 2) moderate; 3) strong; and 4) extensive; (Figure 29, Table 3). We designate the upper phyllosilicate of the crystalline basement closest to the nonconformity as “extensive alteration”. The immediate contact

exhibits extensive alteration where the textures and mineralogy are difficult to discern between hydrothermal alteration, structural diagenesis, and/or near-surface chemical weathering. In this section, original mineral boundaries are no longer visible and have been brecciated to fragments and/or sheared into diffuse shapes, consistent with textures associated with surface weathering type alteration (Figure 4B, 14, 16, Delvigne, 1998). The lack of distinct grain boundaries is likely caused by hydration of oxide minerals to goethite, which results in rock volume changes and disruption to the rock fabric (Boggs, 2006). In the transitional zone to the locally-altered protolith, we define “strong alteration” where primary mineralogy has largely been replaced, but original grain boundaries and/or cleavage are visible. We designate “moderately altered” samples where primary mineralogy is identifiable. For example, sericitized feldspars or pyroxenes altering to mica are typical features in strongly altered sections of the drillcore (Figures 20B-D, 22A). Mafic minerals have intense alteration rims or micas running parallel to cleavage. “Weakly altered” material is present exclusively in the gabbro and layered intrusions. We define this level of alteration as dominantly original mineralogy with altered material occurring as minor sericitization or alteration rims around mafic minerals (Figure 20A, 22).

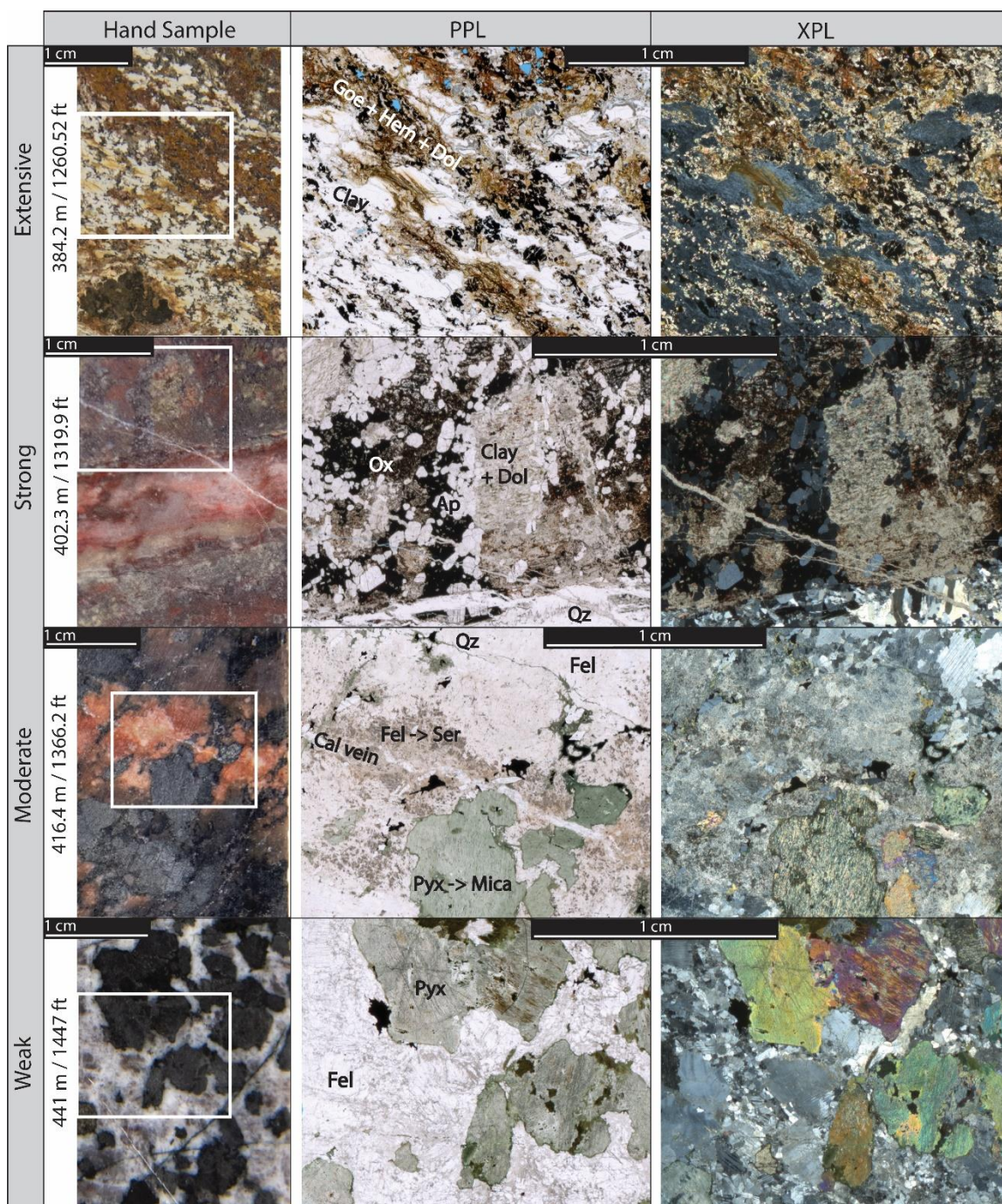


Figure 29: Alteration intensity from meso- to micro-scale. Images provide examples of textural evidence; the exact mineral assemblage may vary per sample or with depth. Thin-section image location outlined in white on the hand sample photo. Thin sections are shown in both plane polarized light (PPL) and cross polarized light (XPL). Mineral abbreviations: Goe-goethite, Hem-hematite, Dol-dolomite, Cal-calcite, Qz- quartz, Ox-oxides, Ap-apatite, Fel-feldspar (albite), Ser-sericite. See Table 3 for more descriptions.

Table 3. Alteration intensity from meso- to micro-scale. Descriptions adapted from Delvigne (1998). Percent replacements are estimated.

Extensive	Replacement of all original mineralogy; typically by clays and/or oxides. Original texture not identifiable, no sharp grain boundaries. Alteration textures consists of sheared, planar fabric with abundant clay (smectite and kaolinite). The samples in this study also likely have overlapping weathering and chemical alteration assemblages. Fragments of cleavage patterns may or may not be visible. Extremely durable minerals like apatite may be present in this section and can display a degree of brecciation and/or dissolution.
Strong	Original mineral outlines may be identifiable but primary mineralogy has been largely replaced (>70%). Some more robust minerals (ex: quartz, apatite) may be preserved. Original rock fabric is discernable, and cleavage of original minerals may be visible from replacement. Feldspars appear gritty with faint cleavage in XPL
Moderate	Original textures and mineral outlines still identifiable but with larger halos/more extensive mineral replacement or sericitization (original cleavage faint or not visible in XPL). ~ 30-70% mineral replacement
Weak	Majority of original mineralogy and textures preserved. Possible alteration features include presence of alteration halos (ex: micas around pyroxene) or patchy presence of alteration within original mineral, sericitization of feldspars though cleavage in XPL remain visible. ~ 0-30% replacement of original material.

5.2 Hydrogeologic Units

We present a conceptual model of the subsurface hydrogeologic setting that integrates the relationship between lithology, structure, alteration, geochemistry, and permeability (Figure 30). We delineate three distinct hydrogeologic units: 1) the sedimentary bedrock 2) the altered nonconformity, and 3) the crystalline basement. The complex nonconformity hydrogeologic unit is further subdivided by distinct alteration phases (Figures 2, 30).

5.2.1 Sedimentary Bedrock

The Mount Simon Sandstone exhibits heterogenous porosity and pore geometry (Figures 11, 12, 23, 24) likely due to original depositional conditions, compaction, diagenesis, and deep fluid-rock dissolution and precipitation (Bowen et al., 2011; Mozley et al., 2016). Such heterogenous rock properties of the reservoir can lead to complicated fluid migration pathways and fluid-rock interactions (Mozley et al., 2016). Despite such heterogeneities, the sedimentary section has the highest porosity and permeability within the examined drillcore sample (Figures 5, 6). In this study, we observe goethite staining just above the nonconformity boundary (Figure 11C) that continues into the alteration zone, which we interpret this as cross-contact fluid communication between the sedimentary bedrock and underlying crystalline basement (Figures 13, 14).

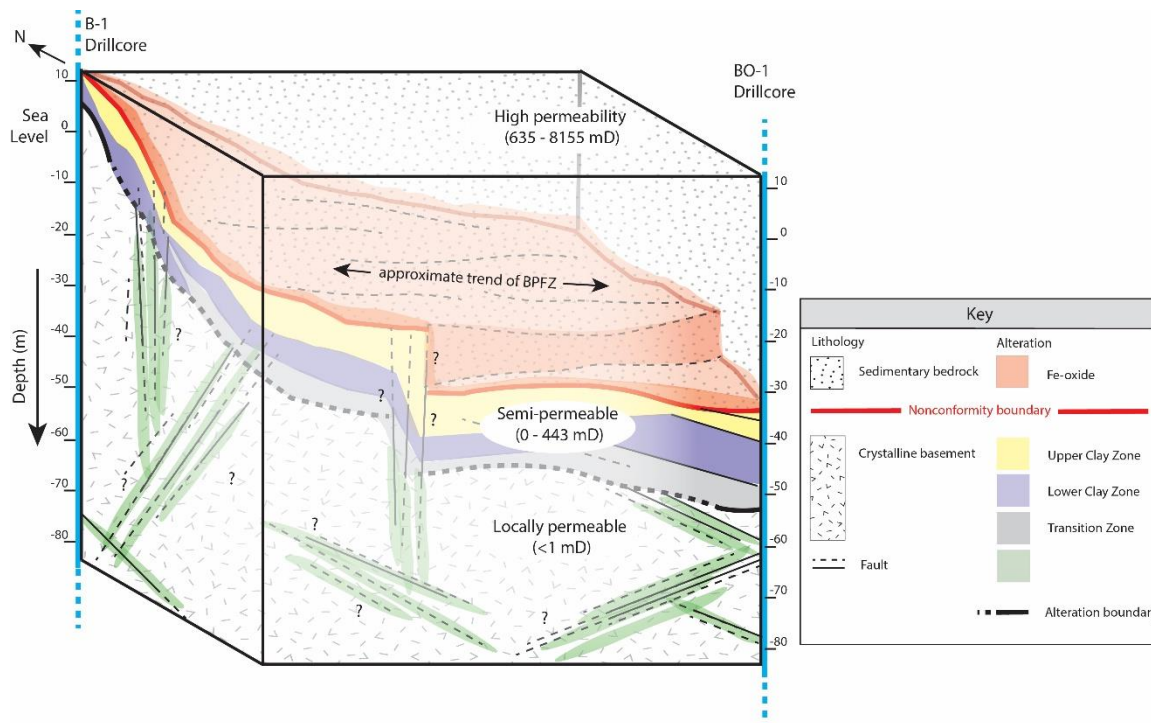


Figure 30: Schematic of the midcontinent nonconformity interface based on observations from the B-1 and BO-1 drillcores (compressed horizontal scale). Drillcore depths have been standardized to meters relative to sea level. The total core length of BO-1 drillcore is 487.6 m and B-1 drillcore is 342.6 m. The nonconformity displays ~46.7 m of topography between the two drillcores. Exact number of fault traces from core logging are reduced for figure clarity. Faults between the two drillcores are schematic, align with the trend of the Belle Plain Fault Zone (BPFZ), and are shown terminating at the nonconformity or crossing into Paleozoic sediment, as has been observed in previous nonconformity characterizations (Morey, 1977; Zhang et al., 2016; Petrie et al., 2020). The alteration associated with the nonconformity can be layered with varying mineralogical assemblages with strong presence of clays, dolomite, and Fe-oxides. Alteration in the crystalline basement is concentrated around faults and fractures.

5.2.2 Altered Nonconformity

The drillcores examined in this study show that an extensive altered nonconformity interface that extends ~ 6 - 22 m below the sedimentary - basement contact and is hydrologically and chemically distinct from the upper sedimentary units and underlying crystalline basement (Figures 6-8). We characterize the nonconformity interface unit as having strong to extensive alteration (Figure 29, Table 3) with intensity increasing towards the nonconformity boundary (Figures 13, 14). Throughout the entire altered nonconformity interface, alteration assemblages can vary by composition and thickness within a single protolith (Figure 2). We observed 3 additional alteration subunits between the nonconformity interface and relatively unaltered protolith in the two drillcores: 1) an upper phyllosilicate zone (Figure 13, 14); 2) a lower phyllosilicate zone (Figures 15-16); and 3) a transitional zone to the locally altered basement unit (Figure 17-18).

Compared to the locally altered basement unit below, the altered nonconformity is significantly different in its geochemistry relative to silica content at the 90% confidence level in all major oxides and LOI (Figures 6-8). In general, the whole-rock geochemical data for rocks below the nonconformity has an extreme range in LOI, CaO, Al₂O₃, & MgO values over very short distances (Figure 6). This geochemical variability supports differential fluid-rock interactions facilitated by complicated structural and permeability architectures (Evans and Chester, 1995). The altered nonconformity has high percentages of CaO and loss on ignition (LOI) values, and low concentrations of SiO₂, Na₂O, and K₂O (Figures 6-8). We interpret the low SiO₂, Na₂O, and K₂O data to correspond to the hydrolytic breakdown of feldspars to clay (Goddard and Evans, 1995) and low initial silica content from the mafic protolith. The high presence of combustible minerals like

carbonates, phyllosilicates, and goethite all contribute to LOI. While these different altered strata share some geochemistry and may exhibit overlap, the three altered zones have significantly different relative concentrations of Al_2O_3 and K_2O at the 90% confidence interval. We interpret these differences to the increased presence of mica minerals in the lower phyllosilicate zone. The upper phyllosilicate zone is significantly different from the transition zone in all major relative oxide concentrations, which we interpret as a result from the transition from low temperature chemical alteration to alteration dominated by hydrothermal processes.

At the cm-scale, crystalline basement hydraulic properties are typically assumed to be low porosity and relatively impermeable, isotropic materials which behave as reservoir seals if not fractured at large scales (Ingebritsen and Manning 1999; Stober and Bucher, 2007). However, these assumptions do not account for extensive alteration. The altered crystalline basement examined in this study is semi-porous (Figure 5), semi-permeable (Figure 6) and extensively faulted and locally fractured (Figure 2). This altered zone has lower mean permeability than the Mount Simon Sandstone, much higher mean permeability than in the unaltered crystalline basement, and permeability and porosity are extremely variable from the meso- to micro-scale (Figures 5, 6). The increases in porosity and permeability are associated with open fractures and faults, which occur in a greater concentration within the altered horizon. We also see pore spaces in extremely altered mineral grains, however these pore channels appear less connected, so they may not contribute to increases in permeability (Figure 5B).

The spatial variability of this hydrogeologic zone, and the alteration assemblages within, appears to be controlled by the intensity of faulting. Based on textural observations,

alteration is more extensive near faults and fractures which may explain why the BO-1 drillcore, which is more faulted and mechanically damaged, has a more extensive altered nonconformity than the B-1 drillcore. Alteration types are bounded by slip surfaces or gouge zones, implying the alteration is associated with structurally-controlled fluid migration (Figure 2). It is difficult to determine when certain alteration or chemical weathering events have occurred due to the spatial limitation of the drillcore. There is some evidence for non-boiling mineralization conditions occurring after boiling conditions seen in Figure 10E where a jigsaw-texture quartz vein is cross-cut by a fine-crystalline dolomite vein. Secondary micaceous material altering to clay and hematite also suggests a hydrothermal event followed by chemical weathering (Figure 16C).

5.2.3 Crystalline Basement Protolith

In the drillcores we examined, the crystalline basement is composed of mafic to intermediate rocks (Figure 3; 4; 9; Table 1). The B-1 drillcore intersects an albite-olivine gabbro (Figures 27-28) and the BO-1 drillcore intersects an amphibolite overlying an intrusive complex with local aplite dikes (Figure 9, 19-22). In addition to mafic protolith mineralogy, this hydrogeologic unit is characterized by localized, minimal alteration proximal to structures such as veins and faults (Figures 21B & E; 28D & E). This hydrogeologic unit generally has low porosity and permeability (0.0-2.1%; <0.01-0.37 mD; Figure 5). Increases are related to open faults. We provide evidence for faults throughout the Proterozoic section of the drillcores to at least ~1.5 km depth (Figure 2). This is critical because faults and fractures are known to be major fluid pathways in the shallow crust (Hickman et al., 1995; Caine et al., 1996; Boullier et al., 2004), and many studies note the presence of hydraulically conductive faults in the basement which may or

may not cross into the overlying sedimentary strata (Stober and Bucher, 2007; Cuccio, 2017; Hesseltine, 2019; Petrie et al., 2020).

5.3 Injection Implications

5.3.1 Geomechanics

In the two drillcore analogs examined for this study, we note the presence of several features which can affect mechanical strength of the crystalline basement, which are the rocks in midcontinent injection sites most likely to experience induced seismic events (Keranen et al., 2013; McNamara et al., 2015; Kolawole et al., 2019). The intensity of alteration may lead to changes in rock volume and rheologic strength (Evans and Chester, 1995; Arancibia et al., 2014; Callahan et al., 2019), thus the crystalline basement rocks altered by multiple fluid-rock events could be more susceptible to fault reactivation particularly in areas with overlapping carbonate and phyllosilicate mineralization. The high LOI values in the altered region regions of the drillcore are associated with the presence of hydrous alteration minerals, carbonates, or other mechanically weak materials compared to unaltered crystalline protolith (Rigopoulos et al, 2015). The amount of phyllosilicates observed throughout the drillcores are significant because of their decreased frictional stability compared to unaltered rock, particularly when exposed to certain injection fluids (Bakker et al., 2019). Previous studies have shown that alteration may increase seismic instability, as seen in deformation experiments (Kolawole et al., 2019). Alteration can also or impact reservoir permeability in geothermal systems depending on the fluid chemistry (Sanchez-Roa, 2021).

The complex and discontinuous vein textures observed here create small-scale heterogeneities to consider when determining basement rock mechanics, especially since the crystalline basement samples with the highest permeability values are associated with open faults and fractures (Figure 8). Since open structures are major channels for fluid migration (Hickman et al., 1995; Caine et al., 1996; Boullier et al., 2004), they are the primary channel for mineral dissolution and precipitation. The other consideration for long-term permeability evolution of open structures, and thus mechanical changes due to fluid-rock interactions, is the composition of injected fluids, e.g. granite permeability increases when subjected to alkaline undersaturated solutions; Sanchez-Roa et al., 2021).

In addition to the geometry and spatial distribution of faults and fractures, their infill composition must also be considered when evaluating the strength and mechanical properties of the injection region. The drillcores in this study have been subjected to fluids of varying chemical compositions and/or conditions, as seen in the precipitation of Fe-oxide/hydroxide minerals, followed by veins of calcite, quartz, or prehnite lower in the core (Figure 9). These complex alteration assemblages imply oxidizing environments (Delvigne, 1998), CO₂-charged fluids (Gislason and Oelkers, 2014), and/or fluids of varying silica saturations (Burnham, 1962; Sanchez-Roa et al., 2021). Additionally, injection fluids can change the frictional stability and likelihood of fault slip depending on the original mineralogy of the fault gouge or damage zone, especially when carbonate cements are involved because they are weak and commonly precipitated in hydrothermal and weathering processes (Hangx et al., 2015; Bakker et al., 2016; Bakker et al., 2019). These layered fault and fracture infillings imply repeated cycles of weakening, dilation, infilling, and/or healing. Regions with fluid-driven seismic cycles are more prone to

reactivation driven by fluid over-pressurization (Sibson et al., 1988), as would be the case with fluid-injection induced seismicity.

Evidence for repeated weakening is a concern when considering seal integrity for large-scale CO₂ storage as a climate change mitigation strategy (Zoback and Gorelick, 2012). However, this research also has implications for CO₂ storage in basaltic composition rocks because the chemistry readily mineralizes CO₂-charged waters (Gislason and Oelkers, 2014), as seen in the heavily dolomitized nonconformity. Additionally, maintaining reservoir permeability is a critical issue for geothermal operations where the permeability evolution of a reservoir depends strongly on the fluid chemistry, pressure, and micro-scale reactions with the host rock (Sanchez-Roa, 2021).

5.3.2 Comparison to Previous Work

Our observations for lateral and cross-contact fluid migration support the observations of previous studies where nonconformity contacts display low relative permeability (Kerner, 2015), which can promote lateral dispersion of fluids from an injection site (Cuccio, 2017; Ortiz et al., 2018; Petrie et al., 2020). Previous studies have noted that nonconformities at depth can be weathered, altered, mineralized, or discrete contacts that may have faults crossing or terminating at the nonconformity boundary (Cuccio, 2017; Petrie et al., 2020). Given the multiple alteration events we see between and within the BO-1 and B-1 drillcores, and the similar observations from other studies (Hamilton et al., 2021), we interpret this nonconformity contact as a combination between the phyllosilicate (Type I) and mineralized (Type II) end member contacts proposed by Petrie *et al.*, (2020).

Based on our observations, structural and mineralogical heterogeneities at the nonconformity are thought to control the degree to which fluids, fluid pressure, and associated poroelastic stresses are transmitted over long distances across and along the nonconformity boundary. The structural and fluid-related alteration patterns observed in these two analog sites indicates that the nonconformity interface can exert a strong influence or control on the permeability architecture and/or the potential for cross-contact fluid flow and fluid fluctuations within the crust (Sanchez-Roa et al., 2021). Where modelling crystalline basement properties are concerned, *in-situ* permeability values for crystalline basement have been reported from 0-100 mD (Brace, 1980) and strongly depend on the lithology and local deformation history (Stober and Bucher, 2007). In this study, permeability values below the nonconformity exceeded that permeability range (Figures 5 & 30).

Currently no drillcore samples which cross the nonconformity are available in the areas of the midcontinent directly affected by injection-induced seismicity (Kolawole et al., 2019; Hamilton et al., 2021). The closest analog sites observed are surface outcrop exposures (Kolawole et al., 2019) and the closest drillcores revealed fractured and hydrothermally altered granitic to andesitic rocks (Hamilton et al., 2021). Similar to the observations in our drillcores, a study of 8 drillcores from northeastern Oklahoma revealed multiple generations of mineralized fractures extending for ~140 m past the nonconformity contact. Furthermore, both studies share a combination of weathering and hydrothermal alteration products with strong presence of carbonates and phyllosilicates at the nonconformity contact. In addition to the alteration assemblages and geochemistry, our

hydrogeologic data provide additional constraints for future and more accurate modelling of the crystalline basement at depth.

6. CONCLUSIONS

The local and broader subsurface geologic conditions are critical to document in areas with the potential for induced seismicity such as the midcontinent region. Failure to account for the heterogeneities in the basement rock may result in moduli calculations that overestimate the strength of basement faults (Kibikas et al., 2019). The existence of inter-related structures and extensive alteration within the crystalline basement emphasizes the need to consider the interplay between host rock, fluid-flow, fault and permeability architecture at depth when modeling the potential fluid-rock interactions and mechanical stability of an injection horizon or reservoir seal (Faulkner et al., 2010).

This case study from two drillcores in SE Minnesota documents the structural, chemical, and hydrologic variability of the nonconformity between Cambrian Mount Simon Sandstone and Precambrian basement. Based on micro- to macro-scale observations, we delineate three distinct hydrogeologic units associated with the nonconformity interface: a sedimentary reservoir, a variably altered nonconformity interface, and an unaltered basement. A laterally discontinuous and variably altered phyllosilicate and carbonate-rich nonconformity interface with evidence for extensive alteration occurs from ~6-22 m immediately below the nonconformity contact. The contacts between the three hydrogeologic units can be gradational on the meter to sub-meter scale. Overall, lithologies, structure, and alteration are variable over short distances

and include a heterogeneous mix of mineral assemblages, geochemistry, and pore channel morphology.

Our geologic observations indicate weathering and hydrothermal fluids have contributed to the alteration assemblages and intensity observed within the crystalline basement. Results support the modelling interpretations of Ortiz *et al.* (2018) and Petrie *et al.* (2020) which show that laterally discontinuous altered zones create conditions for an ineffective seal below an injection reservoir and the potential for fluid migration both laterally and vertically away from the site of injection. Dynamic and evolving permeability can control the movement of fluids and fluid pressures that have the potential to reach hydraulically conductive and critically stressed faults and result in fault zone reactivation (Ortiz *et al.*, 2018). A semi-permeable interface may be an additional fluid-flow pathway for injected wastewater to reach critically stressed faults that do not directly intersect the nonconformity.

CHAPTER III

1. EXHUMED OUTCROP SUMMARY

We examined two exhumed and faulted nonconformity contacts near Gunnison, Colorado. In this region, the nonconformity lies between Jurassic to Cretaceous siliciclastic units and Precambrian gneiss, amphibolite, quartzite, and schist metamorphosed at ~1.7 Ga with granite and diorite intrusions (Afifi, 1981; Steven and Hail, 1989; Kellogg, 2004; Stork et al., 2006). Given the direction of focus and magnitude of data analysis associated with the Minnesota drillcores, the samples collected as part of the field work activities have not been fully characterized nor interpreted. The imagery, X-ray diffraction (XRD) files, and X-ray fluorescence (XRF) spectra can be found in Appendices D, E, H, and I. For potential future work and laboratory analyses, I include a summary of observations made during fieldwork in July of 2019 and subsequent sample processing information.

1.2 Blue Mesa Dam

The Blue Mesa Dam field sites feature a depositional contact between the Jurassic Wanakah Formation (Junction Creek sandstone member) and Precambrian migmatitic gneiss (Figure 1). We collected 12 hand samples across a vertical transect and produced 12 thin sections, 14 XRD analyses and 13 portable XRF (pXRF) analyses from this site (see Data Repository).

The first outcrop BMD-A (UTM 13 S 0296207, 4258819 \pm 2m: Figure 1A) features a laterally discontinuous apparent shear zone between the altered amphibolite basement and sandstone. The zone directly below the sandstone in the sheared-appearing area is generally

poorly consolidated. Textures range from grainy to friable, foliated rocks. There is undulose limonite staining (yellow) and green staining, possibly composed of epidote.

The second outcrop BMD-B (UTM 13 S 0296247, 4258819; Figure 1B) does not show the same sense of shear as observed in BMD-A. A pebble conglomerate base directly overlying the nonconformity. There is approximately 20 cm of weathering/alteration below the contact where the material is foliated parallel to the contact and is poorly consolidated. A few meters east of Outcrop B, the nonconformity has an extremely sharp contact between gneiss (no alteration) and carbonaceous cemented sandstone, with granule clasts and muddy layers.

The third outcrop (BMD-C: Figure 1C) is located west of previous two outcrops and up-section from the nonconformity. The sandstone is orange to buff, medium grained, with rounded to subrounded quartz and FeO coatings around grain contacts. Bedding is horizontal and occasionally undulatory. Lighter areas along fractures indicate bleaching due to fluid migration and fluid-rock interactions. Data collected at this outcrop is pXRF only, for comparison to sandstone samples closer to the nonconformity contact.

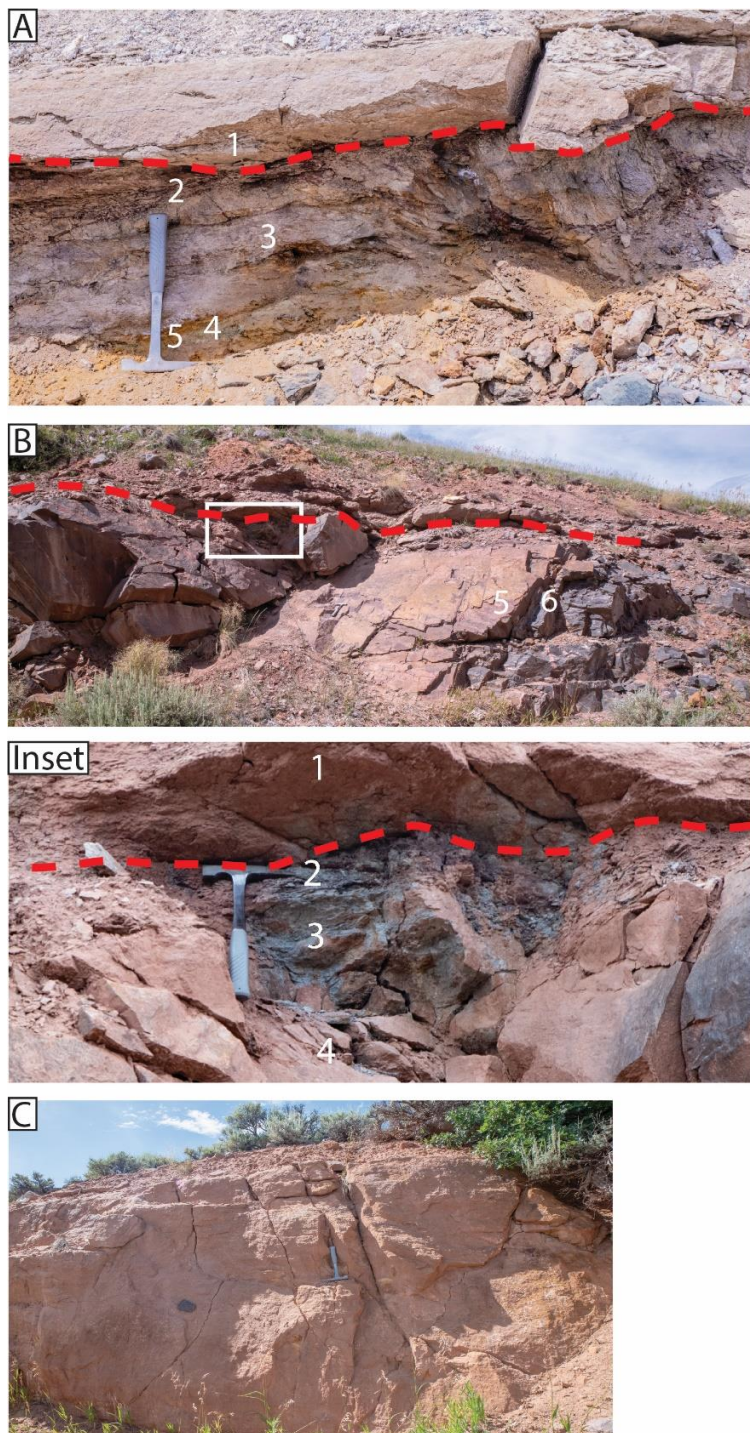


Figure 1: Blue Mesa Dam outcrops. Sampling locations are numbered. Nonconformity contact marked with dashed red line. BMD-A: UTM 13 S 0296207, 4258819 \pm 2m. BMD-B: UTM 13 S 0296247, 4258819. BMD-C is west of the other two outcrops, located in the sedimentary unit up section from the exposed nonconformity contact. Rock hammer for scale.

1.2 Hartman Rocks Recreation Area

The Hartman Rocks field site features an exposed reverse faulted contact between Jurassic Morrison Formation (Brushy Basin sandstone member) and Precambrian amphibolite in a graben (Figure 2). Deformation bands are visible in the sandstone, and the faulted area features a clay gouge zone spanning several meters. At the meso scale, we identified green epidote, which suggests possible propylitic alteration, and Fe and Mn oxides, which appear as red-orange or black stains. We collected 27 hand samples and produced 20 thin sections, 22 field pXRF analyses, 27 XRD analyses and 18 XRF + ICPMS analyses (see Data Repository).

An undulatory fault at site HR-A (UTM 13S 0330363, 4263528) is expressed in outcrop (~170/63 SW) (Figure 3). We sampled along a 12 m horizontal transect crossing from the fault core into the fractured basement rock. The fault core is unconsolidated gouge with pods and fins of crystalline quartz on the sandstone side, which curl up near-parallel to the fault indicating possible fault drag. The basement amphibolite is intensely fractured with yellow limonite coatings on fracture faces.

The second outcrop HR-B (UTM 13S 0330423, 4263497) features an exposure of the same fault with alternating breccia and Fe-rich clay layers (Figure 4). Pieces of basement rock appear to be mixed with the brecciated zone. The basement side of the fault is intensely fractured and limonitic alteration. Basement amphibolite protolith samples were collected in the Hartman Rocks site at a distance from the fault for compositional comparison.



Figure 2: Hartman Rocks field site in Gunnison, CO. (UTM 13S 0330363, 4263528). Faulted contact between Jurassic Morrison Formation (Brushy Basin sandstone member) and Precambrian amphibolite. Approximate fault contact marked with dashed red line. Humans for scale on right side of image.

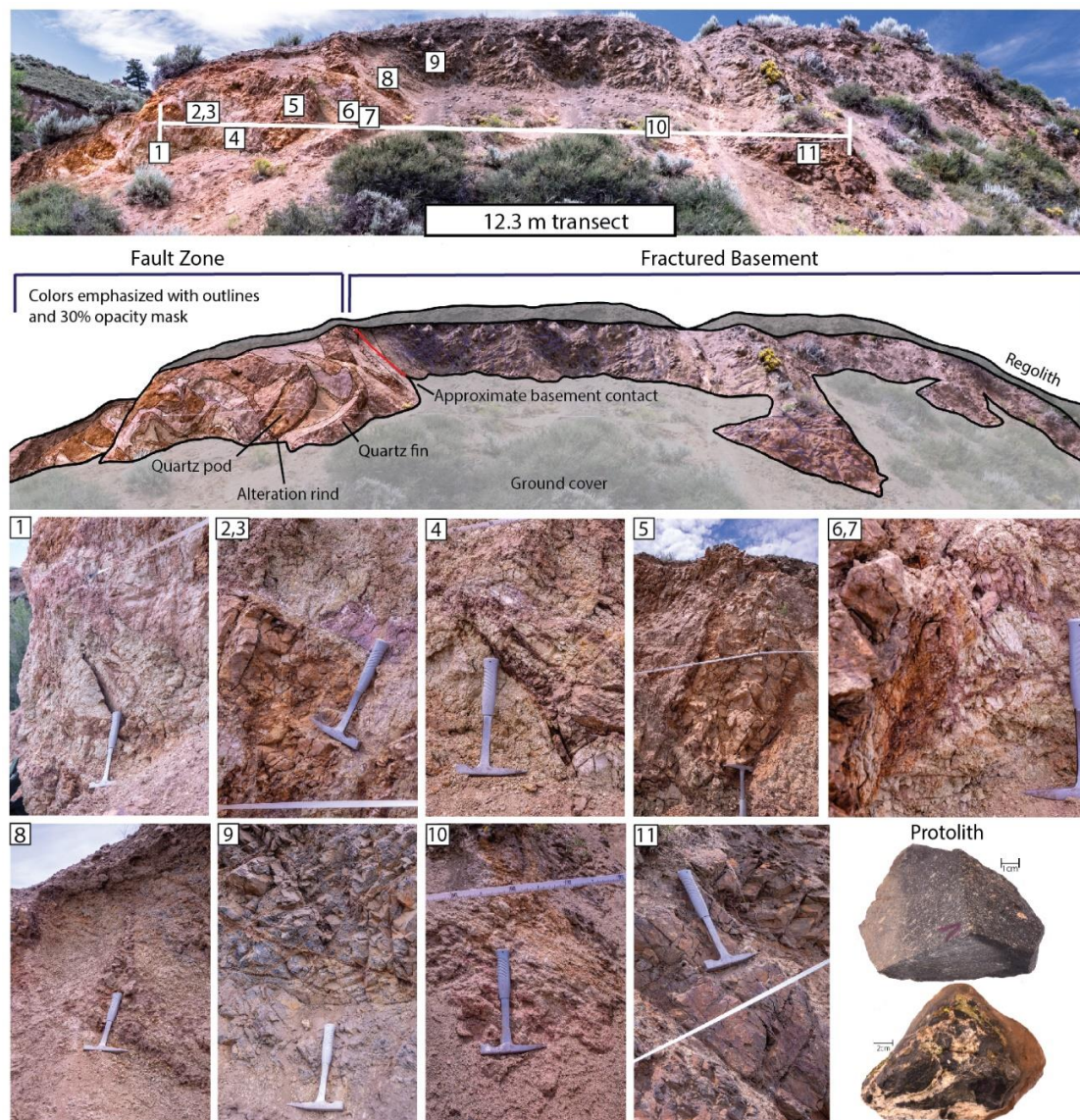


Figure 3: Hartman Rocks outcrop A. (UTM 13S 0330363, 4263528) Gunnison fault damage zone, no unaltered protolith at the outcrop. To the left is a fault gouge zone with clays, intense Fe-oxide alteration, and highly fractured quartz. Amphibolite basement rock is on the right side of the image and is intensely fractured with alteration concentrated around the fractures. Gouge zone mineralogy includes goethite, zeolite, albite, dolomite, siderite, and dickite. Altered basement mineralogy includes albite, amphibole, quartz, vermiculite, and zeolite. Sampling sites and closeup imagery are numbered. Rock hammer for scale. Protolith samples were sources several hundred meters from the fault zone (mineralogy: amphibole, albite, anorthite).



Figure 4: Hartman Rocks Outcrop B. (UTM 13S 0330423, 4263497) Gunnison fault damage zone, no unaltered protolith at the outcrop. To the left is a fault gouge zone with layered clays, intense Fe-oxide alteration, and brecciated clasts of altered basement rock. Amphibolite basement rock is on the right side of the image and is intensely fractured with limonite oxidation concentrated around the fractures. Sample sites are numbered. Approximate basement contact marked with dashed red line. Rock hammer for scale. Note: Sample HR-B-01-19 is located out of view of this image on the left side.

The primary purpose of the geochemical data collected from the Hartman Rocks field site was to compare the efficacy of a portable XRF machine (Bruker Tracer III-V) between field samples *in-situ* and samples collected and processed in a lab as whole-rock powders. Given the heterogenous nature of fault rocks and nonconformity contacts, we were uncertain if the pXRF would capture whole-rock elemental data at the fine scales required to compare to lab analysis, however initial test results show relatively similar XRF spectra compared between the two methods (Paulding, 2020). On-going work aims to quantify this comparison.

These results indicate that pXRF is a useful and efficient method for collecting data, not just in terms of time and expense to analyze material in a lab, but also for obtaining data in areas where destructive sample collection is not permitted (ex: national parks, core labs) or feasible (backcountry exposures).

CHAPTER IV

CONCLUSIONS

Induced seismicity has a wide range of societal, environmental, and economic impacts. Earthquakes related to wastewater injection in the mid-continent region have caused millions of dollars of damage, inciting numerous lawsuits and an increase in earthquake insurance claims (Gallucci, 2015; Wertz, 2015; Pulaski Law Firm, 2019).

Research has demonstrated that seismic faults in the midcontinent predominately rupture in crystalline basement rock, however, very few drillcores remain or are accessible within this region (Zhang et al., 2013; Keranen et al., 2014; Kolawole et al., 2019; Petrie et al., 2020; Hamilton et al., 2021). Detailed characterization of the geologic and hydraulic conditions that occur at depth along the nonconformity injection interface in this study, provide critical constraints for hydrologic and geomechanical risk models and may assist with mitigating impacts related to regions experiencing induced seismicity.

In summary, we observe a ~6-22m altered nonconformity horizon across two drillcore analogs from Minnesota. Alteration mineral assemblages include phyllosilicates and carbonates, which have reduced frictional stability compared to unaltered host rock (Bakker et al., 2016; Bakker et al., 2019; Kolawole et al., 2019). This unit is also semi-permeable, allowing for fluid communication across the nonconformity contact. Broader goals of this focused on rock properties along the nonconformity interface using outcrop analogs in Colorado. We examined sandstone overlying metagabbro and sandstone overlying amphibolite-gneiss nonconformity interface contacts which expands on the lithotypes examined in previous work (Table 1; Cuccio, 2017; Hesseltine, 2019; Petrie et al., 2020) and we provide whole-rock mineralogical and geochemical data and quantitative

permeability measurements spanning the interface contact in both outcrop and core analogs. Our observations reveal the complex nature and heterogeneity of rock properties, fault zone structure, and permeability architecture that may exist within the nonconformity interface region from the micro- to meso-scale. These data, coupled with our outcrop and drillcore characterizations, provide evidenced-based compositional and textural constraints that may exist at the subsurface along injection interface contacts in similar geologic settings.

This study is limited with respect to understanding the entirety of the Paleozoic-Precambrian nonconformity given our spatial limitations on accessible rock material. However, this research has broader implications for how coupled geological-hydromechanical processes affect pressure migration in faulted heterogenous rock sequences (Bense et al., 2013). Specifically, this study further contributes to a knowledge gap related to the nature of pre-existing fault and fracture systems, and associated permeability architecture complexity that may lead to fault reactivation within the interface contact region (Kolawole et al., 2019). These data can also be used to inform the potential impact that long-term storage of chemically reactive fluids may have on rock properties (Callahan et al., 2020) and associated fault zone weakening. Once fluids penetrate the basement, flow is likely controlled by the nature of fracture and fault systems and reactivation of pre-existing structures becomes possible. The complicated fluid-rock interaction history further supports that the contact should not be treated as a simplified impermeable barrier to fluid flow and should instead be evaluated on a site-by-site basis prior to injection of large fluid volumes. (Petrie et al., 2020).

Additional applications of this study include development of more well-constrained hydrologic models of nonconformity contacts associated with geothermal resources and carbon capture and storage (Deichmann and Giardini, 2009; Cappa and Rutqvist 2011; Dewers et al., 2014; Rutqvist et al., 2016). Further studies are needed to quantify the hydromechanical properties resulting from the intensity and variability of alteration. Furthermore, it is important to consider how these altered contacts may respond to complex fluids, such as brines over time. These data have the potential to aid in the design of future rock strength testing and fluid-rock interaction experiments. A second outcome of this work provides critical information to inform the proposed USU-USGS Northeast Iowa Scientific Drilling Project that targets the magnetic and gravitational anomalies associated with the Northeast Iowa Intrusive Complex (Drenth et al., 2015; Drenth et al., 2020).

REFERENCES

- Afifi, A., 1981, Stratigraphy, petrology, and structure of Precambrian metavolcanic rocks in the Iris district, Gunnison and Saguache Counties, Colorado, in *Western slope Colorado: western Colorado and eastern Utah*: New Mexico Geological Society, Thirty-second Field Conference, October 8-10, 1981, Socorro, NM, The Society, p. 287–292.
- Abousif, Alsedik Mohamed Ali, 2015, Mineral and geochemical attributes of the midcontinent rift sequence; An application for deep carbon dioxide sequestration: Doctoral Dissertations. 2372.
https://scholarsmine.mst.edu/doctoral_dissertations/2372
- Anderson, R., 2012, U.S. Geological Survey Airborne Study of Northeast Iowa: Iowa Geological & Water Survey, p. 1-4.
- Arancibia, G., Fujita, K., Hoshino, K., Mitchell, T.M., Cembrano, J., Gomila, R., Morata, D., Faulkner, D.R. and Rempe, M., 2014, Hydrothermal alteration in an exhumed crustal fault zone: Testing geochemical mobility in the Caleta Coloso Fault, Atacama Fault System, Northern Chile: *Tectonophysics*, v. 623, p.147-168.
- Bakker, E., Hangx, S.J., Niemeijer, A.R. and Spiers, C.J., 2016, Frictional behaviour and transport properties of simulated fault gouges derived from a natural CO₂ reservoir: *International Journal of Greenhouse Gas Control*, v. 54, p.70-83.
- Bakker, E., Kaszuba, J., den Hartog, S. and Hangx, S., 2019. Chemo-mechanical behavior of clay-rich fault gouges affected by CO₂-brine-rock interactions: *Greenhouse Gases: Science and Technology*, v. 9(1), p.19-36.
- Bense, V., Gleeson, T., Loveless, S.E., Bour, O., and Scibek, J., 2013, Fault zone hydrogeology: *Earth-Science Reviews*, v. 127, p. 171–192, doi: 10.1016/j.earscirev.2013.09.008.
- Bonnet, A.-L., and Corriveau, L., 2007, Alteration vectors to metamorphosed hydrothermal systems in gneissic terranes, in Goodfellow, W.D., ed., *Mineral deposits of Canada—A synthesis of major deposit-types, district metallogeny, the evolution of geological provinces, and exploration methods*: Geological Association of Canada, Mineral Deposits Division, Special Publication No. 5, p. 1035–1049.
- Boullier, A.M., Fujimoto, K., Ohtani, T., Roman-Ross, G., Lewin, E., Ito, H., Pezard, P. and Ildefonse, B., 2004, Textural evidence for recent co-seismic circulation of fluids in the Nojima fault zone, Awaji island, Japan: *Tectonophysics*, v. 378(3-4), p.165-181.

- Bowen, B.B., Ochoa, R.I., Wilkens, N.D., Brophy, J., Lovell, T.R., Fischietto, N., Medina, C.R. and Rupp, J.A., 2011, Depositional and diagenetic variability within the Cambrian Mount Simon Sandstone: Implications for carbon dioxide sequestration: *Environmental Geosciences*, v. 18(2), p.69-89.
- Brace, W.B., 1980, Permeability of crystalline and argillaceous rocks: *International Journal of Rock Mechanics and Mining Sciences & Geomechanics Abstracts*, v. 17, Issue 5, 1980, Pages 241-251, ISSN 0148-9062, [https://doi.org/10.1016/0148-9062\(80\)90807-4](https://doi.org/10.1016/0148-9062(80)90807-4).
- Burnham, C.W., 1962, Facies and types of hydrothermal alteration: *Economic Geology*, v. 57(5), p.768-784.
- Caine, J.S., Evans, J.P. and Forster, C.B., 1996, Fault zone architecture and permeability structure: *Geology*, v. 24(11), p.1025-1028.
- Callahan, O.A., Eichhubl, P., Kyle, J.R., Zahm, C., and Hennings, P.H., 2019, Factors influencing rock strength and fluid flow at the basement-sediment interface from field- and core-based observations, Llano Uplift, Texas: *Geological Society of America Abstracts in Program*, <https://gsa.confex.com/gsa/2019AM/meetingapp.cgi/Paper/341188> (accessed October 2019).
- Callahan, O.A., Eichhubl, P., Olson, J.E., and Davatzes, N.C., 2020, Experimental investigation of chemically aided fracture growth in silicified fault rocks: *Geothermics*, v. 83.
- Cappa, F., and Rutqvist, J., 2011, Modeling of coupled deformation and permeability evolution during fault reactivation induced by deep underground injection of CO₂: *International Journal of Greenhouse Gas Control*, v. 5, p. 336–346, doi:10.1016/j.ijggc.2010.08.005.
- Chen, X., Nakata, N., Pennington, C. *et al.* The Pawnee earthquake as a result of the interplay among injection, faults and foreshocks. *Sci Rep* **7**, 4945 (2017). <https://doi.org/10.1038/s41598-017-04992-z>
- Cuccio, L., 2017, Geological Characterization of Precambrian Nonconformities: Implications for Injection- Induced Seismicity in the Midcontinent United States: Utah State University, <https://digitalcommons.usu.edu/etd/6889>.
- Deichmann, N., and Giardini, D., 2009, Earthquakes Induced by the Stimulation of an Enhanced Geothermal System below Basel (Switzerland): *Seismological Research Letters*, v. 80, p. 784–798, doi:10.1785/gssrl.80.5.784.
- DeLucia, M.S., Guenther, W.R., Marshak, S., Thomson, S.N., and Ault, A.K., 2017, Thermochronology links denudation of the Great Unconformity surface to the

supercontinent cycle and snowball Earth: *Geology*, v. 46, p. 167–170, doi: 10.1130/g39525.1.

- Delvigne, J., 1998. Atlas of micromorphology of mineral alteration and weathering. Mineralogical Association of Canada: ISBN: 0-921294-43-3.
- Dewers, T., Newell, P., Broome, S., Heath, J., and Bauer, S., 2014, Geomechanical behavior of Cambrian Mount Simon Sandstone reservoir lithofacies, Iowa Shelf, USA: *International Journal of Greenhouse Gas Control*, v. 21, p. 33–48, doi: 10.1016/j.ijggc.2013.11.010.
- Dong, G., Morrison, G. and Jaireth, S., 1995, Quartz textures in epithermal veins, Queensland; classification, origin and implication: *Economic Geology*, v. 90(6), p.1841-1856.
- Doglioni, C., 2017, A classification of induced seismicity: *Geoscience frontiers*, v. 9, no. 6, p. 1903-1909. DOI: 10.1016/j.gsf.2017.11.015.
- Drenth, Benjamin J., Raymond R. Anderson, Klaus J. Schulz, Joshua M. Feinberg, Val W. Chandler, William F. Cannon. What lies beneath: geophysical mapping of a concealed Precambrian intrusive complex along the Iowa–Minnesota border: *Canadian Journal of Earth Sciences*, 2015, v. 52, p. 279-293, <https://doi.org/10.1139/cjes-2014-0178>.
- Drenth, B.J., Souders, A.K., Schulz, K.J., Feinberg, J.M., Anderson, R.R., Chandler, V.W., Cannon, W.F. and Clark, R.J., 2020, Evidence for a concealed Midcontinent Rift-related northeast Iowa intrusive complex: *Precambrian Research*, v. 347, p.105845.
- Ellsworth, W.L., 2013, Injection-Induced Earthquakes: *Science*, v. 341, p. 1225942–1225942, doi: 10.1126/science.1225942.
- EPA, Class II Oil and Gas Related Injection Wells, 2017, <https://www.epa.gov/uic/class-ii-oil-and-gas-related-injection-wells> (accessed August 2019).
- Evans, D.M. 1966, The Denver Area Earthquakes and the Rocky Mountain Arsenal Disposal Well: *Engineering Seismology*, p. 25–32, doi: 10.1130/eng-case-8.25.
- Evans, J.P. and Chester, F.M., 1995, Fluid-rock interaction in faults of the San Andreas system: Inferences from San Gabriel fault rock geochemistry and microstructures. *Journal of Geophysical Research: Solid Earth*, 100(B7), pp.13007-13020.
- Evans, K.F., Genter, A., and Sausse, J., 2005, Permeability creation and damage due to massive fluid injections into granite at 3.5 km at Soultz: 1. Borehole observations: *Journal of Geophysical Research: Solid Earth*, v. 110, doi: 10.1029/2004jb003168

- Faulkner, D., Jackson, C., Lunn, R., Schlische, R., Shipton, Z., Wibberley, C., and Withjack, M., 2010, A review of recent developments concerning the structure, mechanics and fluid flow properties of fault zones: *Journal of Structural Geology*, v. 32, p. 1557–1575, doi: 10.1016/j.jsg.2010.06.009.
- Floyd, P.A. and Winchester, J.A., 1978, Identification and discrimination of altered and metamorphosed volcanic rocks using immobile elements: *Chemical Geology*, v. 21(3-4), p.291-306.
- Foulger, G.R., Wilson, M.P., Gluyas, J.G., Julian, B.R., and Davies, R.J., 2018, Global review of human-induced earthquakes: *Earth-Science Reviews*, v. 178, p. 438–514, doi: 10.1016/j.earscirev.2017.07.008.
- Franseen, Evan K., Byrnes, Alan P., Cansler, Jason R., Steinhaff, D Mark, Carr, Timothy R., 2004, The geology of Kansas- Arbuckle Group Current Research in Earth Sciences, Bulletin 250, part 2.
- Fritz, Richard D., Patrick Medlock, Michael J. Kuykendall, and James L. Wilson, 2012, The geology of the Arbuckle Group in the midcontinent: Sequence stratigraphy, reservoir development, and the potential for hydrocarbon exploration, in J. R. Derby, R. D. Fritz, S. A. Longacre, W. A. Morgan, and C. A. Sternbach, eds., *The great American carbonate bank: The geology and economic resources of the Cambrian—Ordovician Sauk megasequence of Laurentia*: AAPG Memoir 98, p. 203 – 273.
- Frohlich, C., 2012, Two-year survey comparing earthquake activity and injection-well locations in the Barnett Shale: Texas. *Proceedings of the National Academy of Sciences*, v. 109(35), p.13934-13938.
- Gallucci, M., 2015, Oklahoma Earthquake Swarm 2015: In Sharp Turnaround, Oklahoma Officials Confirm The Link Between Fracking Wastewater And Earthquakes: *International Business Times*, <https://www.ibtimes.com/oklahoma-earthquake-swarm-2015-sharp-turnaround-oklahoma-officials-confirm-link-1892086> (accessed August 2019).
- Gilbert, R.C., 1962, Final Report Minnesota Project (Area 4) Fillmore County, Minnesota: The New Jersey Zinc Company, Platteville Wisconsin. 103-9-0 File #1, Item 1.
- Goddard, J.V. and Evans, J.P., 1995, Chemical changes and fluid-rock interaction in faults of crystalline thrust sheets, northwestern Wyoming, USA: *Journal of Structural Geology*, v. 17(4), p.533-547.
- Grove, C., and Jerram, D.A., 2011, jPOR: An ImageJ macro to quantify total optical porosity from blue-stained thin sections: *Computers & Geosciences*, v. 37, p. 1850–1859, doi: 10.1016/j.cageo.2011.03.002.

- Ham, W.E., Denison, R.E., and Merritt, C.A., 1965, Basement Rocks and Structural Evolution of Southern Oklahoma--A Summary: AAPG Bulletin, v. 49, doi: 10.1306/a6633682-16c0-11d7-8645000102c1865d.
- Hangx, S., Bakker, E., Bertier, P., Nover, G. and Busch, A., 2015, Chemical–mechanical coupling observed for depleted oil reservoirs subjected to long-term CO₂-exposure—A case study of the Werkendam natural CO₂ analogue field: Earth and Planetary Science Letters, v. 428, pp.230-242.
- Haq, B.U., and Schutter, S.R., 2008, A Chronology of Paleozoic Sea-Level Changes: Science, v. 322, p. 64–68, doi: 10.1126/science.1161648.
- Healy, J.H., Rubey, W.W., Griggs, D.T., and Raleigh, C.B., 1968, The Denver Earthquakes: Science, v. 161, p. 1301–1310, doi: 10.1126/science.161.3848.1301.
- Hesseltine, Garth, 2018, Micro- to Macro-Scale Structural and Lithological Architecture of Basal Nonconformities: Implications for Fluid Flow and Injection Induced Seismicity: All Graduate Theses and Dissertations. 7497. <https://digitalcommons.usu.edu/etd/7497>
- Hickman, S., Sibson, R. and Bruhn, R., 1995, Introduction to special section: Mechanical involvement of fluids in faulting: Journal of Geophysical Research: Solid Earth, v. 100(B7), p.12831-12840.
- Hincks, T., Aspinall, W., Cooke, R., Gernon, T., 2018, Oklahoma’s induced seismicity strongly linked to wastewater injection depth: Science, v. 7911, p.1-9, doi: 10.1126/science.aap7911
- Hinze, W.J., Braile, L.W., and Chandler, V.W., 1990, A geophysical profile of the southern margin of the midcontinent rift system in western Lake Superior: Tectonics, v. 9, p. 303–310, doi: 10.1029/tc009i002p00303
- Jones, C., 2016, Insurers pay record \$1.5 million in claims for Prague earthquake, but overall approvals are few: Tulsa World, https://www.tulsaworld.com/earthquakes/insurers-pay-record-million-in-claims-for-prague-earthquake-but/article_1f7b1d0d-c8f3-504d-8a03-bda4953c5b07.html (accessed August 2019).
- Karlstrom, K.E., and Timmons, J.M., 2012, Many unconformities make one ‘Great Unconformity’: Grand Canyon Geology; Two Billion Years of Earth’s History, eds Timmons JM, Karlstrom KE (Geol Soc Am, Boulder City, CO): GSA Special Paper 489, pp 73–79.
- Keller, C.B., Husson, J.M., Mitchell, R.N., Bottke, W.F., Gernon, T.M., Boehnke, P., Bell, E.A., Swanson-Hysell, N., and Peters, S.E., 2019, Neoproterozoic glacial origin of the Great Unconformity: doi: 10.31223/osf.io/4k6pd.

- Kellogg, K.S., 2004, The geologic story of Gunnison Gorge National Conservation Area, Colorado: U.S. Geological Survey.
- Keranen, K.M., Savage, H.M., Abera, G.A., and Cochran, E.S., 2013, Potentially induced earthquakes in Oklahoma, USA: Links between wastewater injection and the 2011 Mw 5.7 earthquake sequence: *Geology*, v. 41, p. 699-702, doi: 10.1130/g34045.1
- Keranen, K. M., Weingarten, M., Abers, G. A., Bekins, B. A. and Ge, S., 2014, Sharp increase in central Oklahoma seismicity since 2008 induced by massive wastewater injection: *Science*, 25, 448–451.
- Kerner, K.R., 2015, Permeability architecture of faulted nonconformities: implications for induced seismicity: New Mexico Institute of Mining and Technology, Department of Earth and Environmental Sciences.
- Kibikas, W.M., Carpenter, B.M., and Ghassemi, A., 2019, The Petrophysical and Mechanical Properties of Oklahoma's Crystalline Basement: American Rock Mechanics Association.
- Kolawole, F., Johnston, C.S., Morgan, C.B., Chang, J.C., Marfurt, K.J., Lockner, D.A., Reches, Z., and Carpenter, B.M., 2019, The susceptibility of Oklahoma's basement to seismic reactivation: *Nature Geoscience*, v. 12, p. 839–844, doi: 10.1038/s41561-019-0440-5.
- Lachenbruch, A.H., 1980, Frictional heating, fluid pressure, and the resistance to fault motion. *Journal of Geophysical Research: Solid Earth*, 85(B11), p.6097-6112.
- Lafrance, B., and John, B., 2001, Sheeting and dyking emplacement of the Gunnison annular complex, SW Colorado: *Journal of Structural Geology*, v. 23, p. 1141–1150, doi: 10.1016/s0191-8141(00)00181-4.
- Laubach, S.E., Eichhubl, P., Hilgers, C., and Lander, R.H., 2010, Structural diagenesis: *Journal of Structural Geology*, v. 32, p. 1866–1872, doi:10.1016/j.jsg.2010.10.001
- Leetaru, H. E., S. Frailey, D. Morse, R. J. Finley, J. Rupp, J.A. Drahozval, and J. H. McBride, 2008, Carbon sequestration in the Mt. Simon Sandstone saline reservoir, in M. Grobe, J. C. Pashin, and R. L. Dodge, eds., Carbon dioxide sequestration in geological media: State of the science: AAPG Studies v. 59, p. 1–17.
- Manger, G. Edward, 1963, Porosity and Bulk Density of Sedimentary Rocks; Geological Survey Bulletin 1144-E.
- Marsh, S. and Holland, A., 2016. Comprehensive fault database and interpretive fault map of Oklahoma: Oklahoma Geol. Surv. Open-File Rep. OF2-2016, Oklahoma Geological Survey, Norman, OK.

- Maurer, J., Dunham, E.M. and Segall, P., 2020, Role of fluid injection on earthquake size in dynamic rupture simulations on rough faults: *Geophysical Research Letters*, v. 47(13), p.e2020GL088377.
- McGarr, A., Simpson, D., Seeber, L., 2002. Case histories of induced and triggered seismicity. In: Lee, W.H., Jennings, P., Kisslinger, C., Kanamori, H. (Eds.), *International Geophysics Series. International Handbook of Earthquake and Engineering Seismology* p. 647–664.
- Middlemost, E.A., 1994. Naming materials in the magma/igneous rock system: *Earth-science reviews*, v. 37(3-4), p.215-224.
- MN Department of Natural Resources, 2020, Drill Core Library & Mineral Exploration Collections. URL: <https://arcgis.dnr.state.mn.us/portal/apps/webappviewer/index.html?id=ccb20299e68a4d8881ed8c192f00edda>. Accessed July 2020.
- Moncada, D. and Bodnar, R.J., 2012, Gangue mineral textures and fluid inclusion characteristics of the Santa Margarita Vein in the Guanajuato Mining District, Mexico: *Central European Journal of Geosciences*, v. 4(2), p.300-309.
- Mossler, J.H., 1995, *Geologic Atlas of Fillmore County, Minnesota*: University of Minnesota.
- Mozley, P.S., Heath, J.E., Dewers, T.A. and Bauer, S.J., 2016, Origin and heterogeneity of pore sizes in the Mount Simon Sandstone and Eau Claire Formation: Implications for multiphase fluid flow. *Geosphere*, 12(4), pp.1341-1361. Murray, K.E., 2015, *Class II Saltwater Disposal for 2009–2014 at the Annual-, State-, and County-Scales by Geologic Zones of Completion, Oklahoma*: Oklahoma Geological Survey Open-File Report (OF5-2015).
- Ortiz, J.P., Person, M.A., Mozley, P.S., Evans, J.P., and Bilek, S.L., 2018, The Role of Fault-Zone Architectural Elements on Pore Pressure Propagation and Induced Seismicity: *Groundwater*, v. 57, p. 465–478, doi: 10.1111/gwat.12818.
- Paulding, A., 2020, Using a portable X-ray fluorescence unit to examine rock properties of the nonconformity interface. Poster presented at: Utah Conference on Undergraduate Research, February 2020, Logan, UT.
- Pearce, J.A., 1996, A user's guide to basalt discrimination diagrams. Trace element geochemistry of volcanic rocks: applications for massive sulfide exploration: *Geological Association of Canada, Short Course Notes*, v. 12(79), p.113.

- Peterie, S.L., Miller, R.D., Intfen, J.W., and Gonzales, J.B., 2018, Earthquakes in Kansas Induced by Extremely Far-Field Pressure Diffusion: *Geophysical Research Letters*, v. 45, p. 1395–1401, doi: 10.1002/2017gl076334.
- Peters, S.E., and Gaines, R.R., 2012, Formation of the ‘Great Unconformity’ as a trigger for the Cambrian explosion: *Nature*, v. 484, p. 363–366, doi: 10.1038/nature10969.
- Petrie, E.S., Bradbury, K.K., Cuccio, L., Smith, K., Evans, J.P., Ortiz, J.P., Kerner, K., Person, M. and Mozley, P., 2020, Geologic characterization of nonconformities using outcrop and core analogs: hydrologic implications for injection-induced seismicity: *Solid Earth*, v. 11(5), p.1803-1821.
- Powell, J.W., Thompson, A.H., Coues, E., and Goode, G.B., 1875, *Exploration of the Colorado River of the West and its tributaries: explored in 1869, 1870, 1871, and 1872, under the direction of the Secretary of the Smithsonian Institution: Washington, G.P.O.*
- Pulaski Law Firm, 2019, <https://ifspb.com/oklahoma-fracking-earthquake-property-home-damage-lawsuit-lawyer-help/> (accessed Jan. 2019)
- Rigopoulos, I., Tsikouras, B., Pomonis, P. and Hatzipanagiotou, K., 2015, Assessment of the engineering behavior of ultramafic and mafic rocks using chemical indices: *Engineering Geology*, v. 196, p.222-237.
- Rubinstein, J.L., and Mahani, A.B., 2015, Myths and Facts on Wastewater Injection, Hydraulic Fracturing, Enhanced Oil Recovery, and Induced Seismicity: *Seismological Research Letters*, v. 86, p. 1060–1067, doi:10.1785/0220150067.
- Rutqvist, J., Rinaldi, A.P., Cappa, F., Jeanne, P., Mazzoldi, A., Urpi, L., Guglielmi, Y., and Vilarrasa, V., 2016, Fault activation and induced seismicity in geological carbon storage – Lessons learned from recent modeling studies: *Journal of Rock Mechanics and Geotechnical Engineering*, v. 8, p. 789–804, doi: 10.1016/j.jrmge.2016.09.001.
- Sanchez-Roa, C., Saldi, G.D., Mitchell, T.M., Iacoviello, F., Bailey, J., Shearing, P.R., Oelkers, E.H., Meredith, P.G., Jones, A.P. and Striolo, A., 2021. The role of fluid chemistry on permeability evolution in granite: Applications to natural and anthropogenic systems: *Earth and Planetary Science Letters*, v. 553, p.116641.
- Scales, M.M., DeShon, H.R., Magnani, M.B., Walter, J.I., Quinones, L., Pratt, T.L. and Hornbach, M.J., 2017, A decade of induced slip on the causative fault of the 2015 Mw 4.0 Venus earthquake, northeast Johnson County, Texas. *Journal of Geophysical Research: Solid Earth*, v. 122(10), p.7879-7894.
- Sibson, R.H., Robert, F. and Poulsen, K.H., 1988, High-angle reverse faults, fluid-pressure cycling, and mesothermal gold-quartz deposits: *Geology*, v. 16(6), p.551-555.

- Sims, P. K., 1990, Precambrian Basement Map of the Northern Midcontinent, U.S.A., U. S. Geological Survey Open-File Report Open-File Report 85-604.
- Smith, V., and Jaques, P., 2016, Illinois Basin – Decatur Project pre-injection microseismic analysis: *International Journal of Greenhouse Gas Control*, v. 54, p. 362–377, doi: 10.1016/j.ijggc.2015.12.004.
- Steven, T.A., and Hail, W.J., Jr., 1989, Geologic map of the Montrose 30' X 60' quadrangle, southwestern Colorado, National Geologic Map Database: U.S. Geological Survey. Miscellaneous Investigations Series Map I-1939
- Stober, I. and Bucher, K., 2007. Hydraulic properties of the crystalline basement: *Hydrogeology Journal*, v. 15(2), pp.213-224.
- Stork, Allen, Coogan, James C., Csar, Alex, and Wentz, Raelene, 2006, Geologic Map of the Gunnison Quadrangle, Gunnison County, Colorado: Colorado Geological Survey, Open-File Report OF-06-04.
- Taylor, R., 2009, *Ore textures: recognition and interpretation*. Springer Science & Business Media. ISBN: 9783642017827.
- Townend, J. and Zoback, M.D., 2000, How faulting keeps the crust strong: *Geology*, v. 28, no. 5, p. 399-402.
- USGS, 2018, Induced Earthquakes: [https://earthquake.usgs.gov/research/induced/overview .php](https://earthquake.usgs.gov/research/induced/overview.php) (accessed Dec. 2018)
- USGS, 2019, Latest Earthquakes: <https://earthquake.usgs.gov/earthquakes/map/> (accessed July 2019).
- Van Poolen, H.K. and Hoover, D.B., 1970, Waste disposal and earthquakes at the rocky mountain arsenal, Derby, Colorado: *Journal of Petroleum Technology*, v. 22(08), p.983-993.
- Walsh, F.R., and Zoback, M.D., 2015, Oklahoma’s recent earthquakes and saltwater disposal: *Science Advances*, v. 1, doi: 10.1126/sciadv.1500195.
- Weingarten, M., Ge, S., Godt, J.W., Bekins, B.A., Rubinstein, J.L., 2015, High-rate injection is associated with the increase in U.S. mid-continent seismicity: *Science Research Reports*, v. 348, no. 6241.
- Wertz, J., 2015, Oklahoma Earthquake Rate is High, But Holding Steady: State Impact Oklahoma, <https://stateimpact.npr.org/oklahoma/2015/01/14/oklahoma-earthquake-rate-is-high-but-holding-steady/> (accessed Jan. 2019)


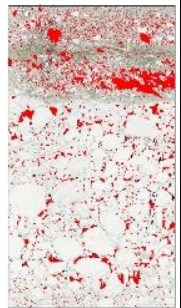
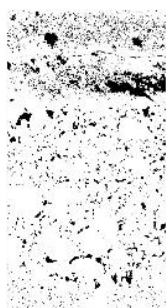

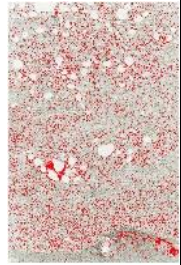
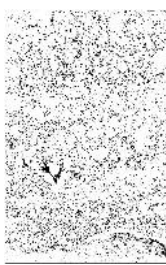


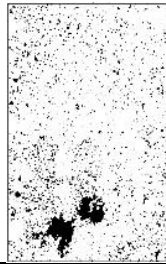

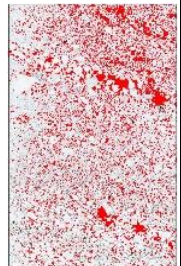
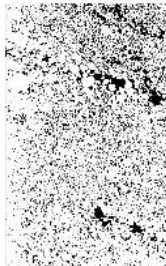
- Wickstrom, L.H, Venteris, E.R., Harper, J.A., McDonald, J., Slucher, E.R., Carter, K.M., Greb, S.F., Wells, J., Harrison III, W.B., Nuttall, B.C., Riley, R.A., Drahovzal, J.A., Rupp, J.A., Avary, K.L., Lanham, S., Barnes, D.A., Gupta, N., Baranoski, M.A., Radhakrishnan, P., Solis, M.P., Baum, G.R., Powers, D., Hohn, M.E., Parris, M.P., McCoy, K., Grammar, G.M., Pool, S., Luckhardt, C., and Kish, P., 2010, Characterization of geologic sequestration opportunities in the MRCSP region: Phase I task report. ODNR Geological Survey Open-File Report 2005-1.
- Williams, R.T., 2019, Coseismic boiling cannot seal faults: Implications for the seismic cycle: *Geology*, v. 47(5), p.461-464.
- Yanguas, J.E., and Dravis, J.J., 1985, Blue Fluorescent Dye Technique for Recognition of Microporosity in Sedimentary Rocks: RESEARCH METHOD PAPER: SEPM Journal of Sedimentary Research, v. Vol. 55, doi: 10.1306/212f875b-2b24-11d7-8648000102c1865d.
- Yehya, A., Yang, Z., and Rice, J.R., 2018, Effect of Fault Architecture and Permeability Evolution on Response to Fluid Injection: *Journal of Geophysical Research: Solid Earth*, v. 123, p. 9982–9997, doi: 10.1029/2018jb016550.
- Zhang, Y., Person, M., Rupp, J., Ellett, K., Celia, M.A., Gable, C.W., Bowen, B., Evans, J., Bandilla, K., Mozley, P., Dewers, T., and Elliot, T., 2013, Hydrogeologic Controls on Induced Seismicity in Crystalline Basement Rocks Due to Fluid Injection into Basal Reservoirs: *Groundwater*, v. 51, p. 525–538, doi: 10.1111/gwat.12071.
- Zhang, Y., Edel, S.S., Pepin, J., Person, M., Broadhead, R., Ortiz, J.P., Bilek, S.L., Mozley, P. and Evans, J.P., 2016, Exploring the potential linkages between oil-field brine reinjection, crystalline basement permeability, and triggered seismicity for the Dagger Draw Oil field, southeastern New Mexico, USA, using hydrologic modeling: *Geofluids*, v. 16(5), p.971-987.
- Zoback, M.D., and Harjes, H.P., 1997, Injection-induced earthquakes and crustal stress at 9 km depth at the KTB deep drilling site, Germany: *Journal of Geophysical Research: Solid Earth*, v. 102, p. 18477–18491, doi: 10.1029/96jb02814.
- Zoback, M.D. and Gorelick, S.M., 2012, Earthquake triggering and large-scale geologic storage of carbon dioxide: *Proceedings of the National Academy of Sciences*, v. 109(26), p.10164-10168.

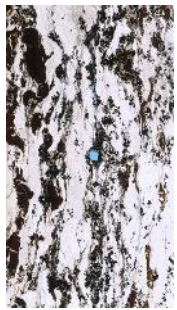














APPENDICES

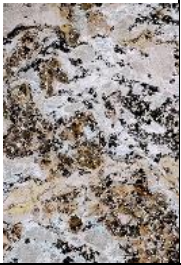
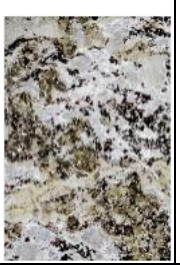


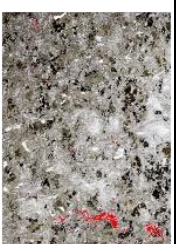








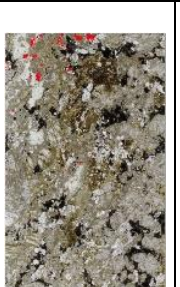




APPENDIX A: Permeability values for select samples of the BO-1 drillcore. Gas permeability measurements conducted through Schlumberger. The system has lower permeability limit of 0.01 mD, samples below this threshold were assigned a value of 0.00 mD when averaged. Prior to measuring the permeability on these samples, the lab performed a system check using a known Berea Sandstone and repeated the process in between the sample measurement. The average Berea permeability varied between 120 - 280 md over the length of the Berea sample. The permeability measurements were taken as close to the designated points as possible.



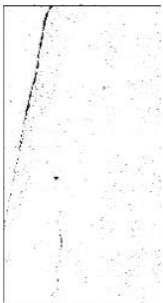















SAMPLE ID	POINT 1		POINT 2		POINT 3		POINT 4		POINT 5		AVG SAMPLE PERM						
	ATTEMPT 1	ATTEMPT 2	ATTEMPT 1	ATTEMPT 2	ATTEMPT 1	ATTEMPT 2	ATTEMPT 1	ATTEMPT 2	ATTEMPT 1	ATTEMPT 2	AVG	AVG	stddev n=5				
BO-1-1183.67-1184.00	1337.75	1248.76	1293.26	3.23	4.31	3.77	29.07	1220.69	1234.09	1227.39	617.64	620.82	619.23	634.54	622.51		
BO-1-1224.15-1224.42	833.52	772.63	803.07	305.68	299.58	302.63	2396.86	2363.17	2380.02	1209.45	1209.98	409.22	405.16	407.19	1020.58	840.08	
BO-1-1259.90-1260.18	857.92	735.25	796.58	110.96	125.36	118.16	37698.10	41951.90	39825.00	16.20	17.20	16.70	17.87	17.28	8154.74	17707.21	
BO-1-1260.30-1260.52	1.94	2.52	2.23	5.23	4.85	5.04	4.13	4.44	4.44	3.73	3.93	3.83	4.61	4.43	4.52	4.01	1.09
BO-1-1260.52-1261.00	0.11	0.14	0.13	7.11	6.94	7.03	0.06	0.05	0.05	0.08	0.07	0.08	0.17	0.17	0.17	1.49	3.10
BO-1-1261.52-1261.83	0.02	0.03	0.03	0.38	0.38	0.38	7.71	8.04	7.87	0.13	0.13	0.13	0.02	0.02	0.02	1.68	3.46
BO-1-1262.11-1262.47	0.33	0.35	0.34	0.05	0.00	0.03	0.08	0.09	0.09	0.09	0.47	0.04	0.04	0.04	0.04	0.19	0.20
BO-1-1262.87-1263.13	0.03	0.01	0.02	0.04	0.03	0.04	0.04	0.03	0.04	<0.01	<0.01	<0.01	<0.01	<0.01	<0.01	0.02	0.02
BO-1-1263.65-1263.05	1.91	1.95	1.93	0.13	0.14	0.14	0.69	0.68	0.69	0.55	0.51	0.53	0.02	0.01	0.01	0.66	0.76
BO-1-1275.00-1275.35	1.26	0.76	1.01	2.05	2.05	2.05	2.45	2.83	2.64	1.45	2.79	2.12	2.89	1.92	2.41	2.04	0.63
BO-1-1283.30-1283.70	6.75	4.97	5.86	0.02	<0.01	0.01	<0.01	<0.01	<0.01	0.49	0.48	0.48	2.72	2.69	2.70	1.81	2.52
BO-1-1293.90-1294.30	10.79	11.03	10.91	27.93	28.48	28.21	668.12	615.23	641.67	1547.56	1436.60	1492.08	40.98	41.52	41.25	442.82	644.24
BO-1-1318.65-1319.35	0.41	0.45	0.43	0.33	0.30	0.31	0.05	0.02	0.03	<0.01	<0.01	<0.01	0.43	0.43	0.43	0.24	0.21
BO-1-1319.90-1320.25	<0.01	<0.01	<0.01	<0.01	<0.01	<0.01	<0.01	<0.01	<0.01	0.01	0.01	0.01	<0.01	<0.01	<0.01	<0.01	<0.01
BO-1-1332.30-1332.50	0.04	0.05	0.04	0.07	0.06	0.06	0.01	0.01	0.01	0.02	0.02	0.02	0.08	0.11	0.09	0.05	0.03
BO-1-1344.00-1344.40	0.01	0.03	0.02	0.01	<0.01	<0.01	<0.01	<0.01	<0.01	<0.01	0.01	0.01	<0.01	<0.01	<0.01	0.01	0.01
BO-1-1347.60-1348.00	<0.01	<0.01	<0.01	0.02	0.02	0.02	<0.01	0.01	0.01	<0.01	<0.01	<0.01	<0.01	<0.01	<0.01	0.01	0.01
BO-1-1366.20-1366.60	<0.01	<0.01	<0.01	<0.01	<0.01	<0.01	<0.01	<0.01	<0.01	<0.01	<0.01	<0.01	<0.01	0.02	0.01	<0.01	0.00
BO-1-1385.40-1386.00	<0.01	<0.01	<0.01	1.78	1.79	1.79	<0.01	<0.01	<0.01	<0.01	0.01	0.01	0.03	0.05	0.04	0.37	0.79
BO-1-1395.40-1396.00	0.01	<0.01	0.01	<0.01	0.02	0.01	<0.01	<0.01	<0.01	0.01	0.02	0.01	<0.01	<0.01	<0.01	0.01	0.01
BO-1-1411.60-1412.00	<0.01	<0.01	<0.01	<0.01	<0.01	<0.01	<0.01	<0.01	<0.01	<0.01	<0.01	<0.01	<0.01	<0.01	<0.01	<0.01	<0.01
BO-1-1447.70-1448.25	<0.01	<0.01	<0.01	<0.01	<0.01	<0.01	<0.01	0.03	0.01	0.09	0.16	0.12	<0.01	<0.01	<0.01	0.03	0.06
BO-1-1459.40-1459.60	<0.01	<0.01	<0.01	<0.01	<0.01	<0.01	<0.01	<0.01	<0.01	<0.01	<0.01	<0.01	<0.01	<0.01	<0.01	<0.01	<0.01
BO-1-1472.30-1473.00	<0.01	<0.01	<0.01	<0.01	<0.01	<0.01	0.01	0.02	0.01	<0.01	<0.01	<0.01	<0.01	<0.01	<0.01	<0.01	0.01
BO-1-1552.30-1552.65	<0.01	<0.01	<0.01	<0.01	0.02	0.01	0.01	<0.01	<0.01	<0.01	<0.01	<0.01	0.03	0.01	0.02	0.01	0.01




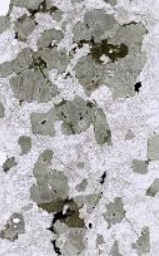
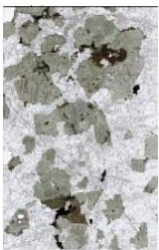

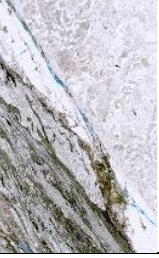

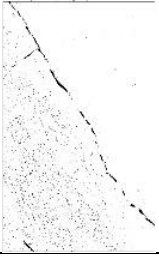






APPENDIX B: Porosity values for select samples of the BO-1 drillcore. The thin section imagery is cropped to exclude surrounding epoxy and are processed according to the methods of Grove and Jerram (2011). The imageJ jPOR plugin highlights the dyed blue pore space with red pixels and then reduces the image to a binary image where the black pore space pixels are reported as a percentage of the image area. Errors are reported as 1.2% of the detected area, which is the mean inter-operator variability (Grove and Jerram, 2011).

Sample (ft)	%Area	Error (1.2%)	Cropped Image	Image + Pore	Pore Space Only
1183.67 A	10.5	1.3			
1183.67b	11.7	1.4			
1224.15	9.1	1.1			
1259.90	19.2	2.3			

1260.30 a	0.6	0.1			
1260.52	0.6	0.1			
1261.52	0.6	0.1			
1262.11	0.1	0.0			
1262.87	0.5	0.1			

1263.65	0.7	0.1			
1275.00	0.9	0.1			
1283.30	0.2	0.0			
1293.90	1.7	0.2			
1318.65	0.6	0.1			
1319.90	0.1	0.0			

1332.30	0.9	0.1			
1344.00	0.1	0.0			
1347.60	0.0	0.0			
1366.20	0.3	0.0			
1385.40	0.6	0.1			
1395.40	0.7	0.1			

1411.60	0.0	0.0			
1447.70	0.3	0.0			
1459.40	2.1	0.3			
1472.30	0.7	0.1			
1552.30	0.9	0.1			

APPENDIX C: XRF data for select samples of the BO-1 drillcore. Samples were processed at the Washington State University GeoAnalytical lab using their laboratory equipment and protocols. Sample 1263.65 had a duplicate bead sample made with the same rock powder. Total Fe is expressed as FeO.

Unnormalized Major Elements (Weight %):												
Sample (ft)	SiO2	TiO2	Al2O3	FeO*	MnO	MgO	CaO	Na2O	K2O	P2O5	Sum	LOI %
BO-1_1224.15-1224.42	83.74	0.110	1.02	1.32	0.040	1.27	5.61	0.00	0.32	2.474	95.90	3.62
BO-1_1260.30-1260.52	25.69	14.224	21.49	25.88	0.582	0.26	0.19	0.00	0.46	0.528	89.31	10.10
BO-1_1261.00-1261.25	13.18	10.485	11.21	10.78	0.793	7.16	18.92	0.00	0.04	4.191	76.76	22.85
BO-1_1261.52-1261.83	16.72	9.387	14.01	10.88	0.710	5.59	17.23	0.00	0.06	4.897	79.49	19.98
BO-1_1262.11-1262.47	18.65	8.833	15.57	9.91	0.697	5.54	15.50	0.00	0.07	3.900	78.66	20.84
BO-1_1262.87-1263.13	9.94	7.096	7.93	17.60	0.578	7.58	20.63	0.00	0.15	4.342	75.86	24.03
BO-1_1263.65-1263.95	23.91	7.002	19.40	15.93	0.387	2.23	11.83	0.00	0.26	5.323	86.27	13.50
BO-1_1269.00-1269.17	16.43	6.386	6.43	40.07	0.223	3.69	8.87	0.00	2.37	2.819	87.29	12.26
BO-1_1275.00-1275.35	37.37	5.289	13.93	21.58	0.088	2.22	4.07	0.00	5.80	2.600	92.95	6.99
BO-1_1283.30-1283.70	14.10	7.691	5.57	29.67	0.398	6.10	12.73	0.00	2.08	1.985	80.32	19.31
BO-1_1307.25-1307.50 A	32.25	2.987	11.49	24.99	0.094	3.61	3.58	0.00	4.47	0.831	84.31	15.27
BO-1_1318.65-1319.35	25.84	6.280	10.21	21.91	0.295	4.39	9.39	0.00	3.32	2.986	84.62	15.17
BO-1_1319.90-1320.25	29.86	7.719	0.80	24.89	0.738	3.60	16.72	0.00	0.02	4.872	89.22	10.57
BO-1_1330.40-1330.60	31.39	4.192	3.22	19.53	0.489	6.76	20.29	0.04	0.05	8.547	94.51	4.96
BO-1_1332.30-1332.50	49.92	1.304	15.22	10.80	0.255	5.42	10.54	3.20	0.92	0.523	98.11	1.36
BO-1_1344.00-1344.40	31.70	6.502	8.01	32.99	0.282	3.71	10.56	1.51	0.09	3.800	99.16	0.34
BO-1_1347.60-1348.00	49.38	0.734	19.90	13.24	0.215	3.95	4.90	4.02	1.35	0.036	97.72	1.87
BO-1_1366.20-1366.60	43.29	0.969	14.17	21.44	0.378	7.48	6.97	2.32	0.44	0.486	97.94	1.90
BO-1_1381.70-1382.00	39.09	4.494	12.04	21.82	0.383	5.01	10.22	2.46	0.59	2.826	98.93	0.52
BO-1_1389.10-1389.60	46.82	2.304	14.17	13.60	0.244	6.40	8.59	4.13	0.43	1.376	98.07	1.56
BO-1_1395.40-1396.00	56.90	1.389	17.39	8.09	0.128	2.24	3.16	7.69	0.36	0.727	98.08	1.42
BO-1_1411.60-1412.00	52.46	0.187	21.68	7.34	0.153	2.65	8.63	4.33	0.88	0.047	98.36	1.08
BO-1_1447.70-1448.25	50.33	1.809	17.88	9.50	0.206	3.30	10.81	4.03	0.48	0.766	99.11	0.46
BO-1_1451.50-1451.90	43.56	6.463	11.05	18.84	0.384	4.38	9.33	3.06	0.59	1.215	98.87	0.55
BO-1_1458.00-1458.80	76.59	0.030	13.92	0.20	0.004	0.02	0.50	7.07	1.05	0.014	99.39	0.09
BO-1_1472.30-1473.00	54.24	0.709	22.99	4.90	0.067	1.05	7.61	6.06	0.61	0.249	98.50	0.88
BO-1_1495.60-1496.40	43.32	3.658	13.38	17.36	0.304	4.36	9.82	3.59	0.55	2.331	98.67	1.02
BO-1_1524.60-1524.90	34.16	5.393	7.44	31.14	0.543	8.76	8.39	1.10	0.13	2.330	99.40	0.00
BO-1_1550.72-1551.15 A	75.77	0.078	10.42	2.91	0.097	0.76	4.20	3.67	0.45	0.045	98.40	1.05
BO-1_1552.30-1552.65	35.25	5.487	12.69	22.42	0.336	5.04	10.29	2.06	1.56	3.542	98.69	0.69
BO-1_1573.00-1573.5	75.70	0.108	13.28	1.26	0.014	0.25	1.21	6.21	0.41	0.034	98.48	0.79
BO-1_1263.65-1263.95	23.91	7.002	19.40	15.93	0.387	2.23	11.83	0.00	0.26	5.323	86.27	13.50
BO-1_1263.65-1263.95*	24.14	6.992	19.37	15.62	0.386	2.23	11.79	0.00	0.26	5.324	86.11	13.50